Pontifícia Universidade Católica
do Rio de Janeiro

Raphael Pereira Pinto

Non-destructive, microstructural and mechanical performance evaluation of metal polymer hybrid structures

Dissertação de Mestrado

Dissertation presented to the Programa de Pós-graduação em Engenharia de Materiais e de Processos Químicos e Metalúrgicos of PUC-Rio in partial fulfillment of the requirements for the degree of Mestre em Engenharia de Materiais e de Processos Químicos e Metalúrgicos.

Advisor: Prof. Sidnei Paciornik

Rio de Janeiro

August 2017

Raphael Pereira Pinto

Non-destructive, microstructural and mechanical performance evaluation of metal-polymer hybrid structures

Dissertation presented to the Programa de Pós-graduação em Engenharia de Materiais e de Processos Químicos e Metalúrgicos of PUC-Rio in partial fulfillment of the requirements for the degree of Mestre em Engenharia de Materiais e de Processos Químicos e Metalúrgicos. Approved by the undersigned Examination Committee.

Prof. Sidnei Paciornik
Advisor
Departamento de Engenharia Química e de Materiais – PUC Rio

Profa. Ivani de Souza Bott
Departamento de Engenharia Química e de Materiais – PUC Rio

Prof. Valter Rocha dos Santos
Departamento de Engenharia Química e de Materiais – PUC Rio

Prof. Marcio da Silveira Carvalho
Vice Dean of Graduate Studies Centro Técnico Científico – PUC-Rio

Rio de janeiro, August 31st, 2017

Raphael Pereira Pinto

The author graduated in Petroleum Engineering from Universidade de Vila Velha - UVV in 2012. Specializing in the areas of: Materials science and High-Resolution Tridimensional Characterization.

Bibliographic data

Pinto, Raphael Pereira

Non-destructive, microstructural and mechanical performance evaluation of metal-polymer hybrid structures/ Raphael Pereira Pinto; advisor: Sidnei Paciornik - Rio de Janeiro: PUC-Rio, Departamento de Engenharia Química e de Materiais, 2017.

v., 119 f: il. color. ; 30 cm

Dissertação (mestrado) – Pontifícia Universidade Católica do Rio de Janeiro, Departamento de Engenharia Química e de Materiais.

Inclui bibliografia

1. Engenharia Química – Teses. 2. Engenharia de Materiais – Teses. 3. União pontual por fricção. 4. Rebitagem por fricção. 5. União por energia ultrassônica. 6. Estruturas Híbridas. 7. Microtomografia Computadorizada. I. Paciornik, Sidnei. II. Pontifícia Universidade Católica do Rio de Janeiro. Departamento de Engenharia Química e de Materiais. III. Título.

CDD: 620:11

I kindly dedicate this MSc thesis to the woman who made me believe in faith:

Zenobia Gaigher Pino, my beloved grandmother!

Acknowledgments

Several people supported the successful completion of this MSc. To them, I would like to express the deepest appreciation for all the help and encouragement:

- Prof. Dr. Sidnei Paciornik for the supportive orientation, inspiration, encouragement, precious guidance in this work and opportunity to conclude this MSc study in such a renowned institution (PUC-Rio).
- Dr. Valter Rocha Santos for the internship opportunity in Germany and support of this work.
- Dr. Jorge F. dos Santos and Prof. Dr. Sergio T. Amancio Filho for the opportunity to perform part of my experiments with the Solid State Joining Processes Group in Germany and access the know-how of their group. Special thanks to Dagmar Koschek for the friendship and exceptional support in all issues during my stay in Germany.
- The Digital Image Analysis Group, for the greatest example of competence, dedication, teamwork and mutual support. Special thanks to Dr. Marcos H. P. Mauricio for unconditional support in microCT imaging.
- Natália Manente André, Natascha Zocoller Borba and Eduardo Feistauer for the technical assistance, useful critiques and support. Specially, all my colleagues of Helmholtz-Zentrum Geesthacht for their support and fellowship during my stay in Germany.
- CNPq for sponsoring me with MSc scholarship.
- Finally, and most important, God for the guidance and all blessings in my journey.

Abstract

Pinto, Raphael Pereira; Paciornik, Sidnei (Advisor). **Non-destructive, microstructural and mechanical performance evaluation of metal-polymer hybrid structures**. Rio de Janeiro, 2017. 119p. Dissertação de Mestrado - Departamento de Engenharia Química e de Materiais, Pontifícia Universidade Católica do Rio de Janeiro.

The transportation industry has been facing stringent environmental regulations to decrease fuel consumption and CO_2 emissions. A promising solution to fulfill these demands is decreasing the structural weight of vehicles and airplanes by combining lightweight alloys and fiber-reinforced polymers in hybrid structures. Conventional joining technologies are usually inadequate to produce high performance joints. To overcome these limitations, advanced joining technologies are under development such as: Friction Spot Joining (FSpJ), Friction Riveting (FricRiveting) and Ultrasonic Joining (U-Joining). This master dissertation was devised to evaluate FSp, FricRiveting and U-Joining joints produced with different heat input levels (low and high) in terms of process temperature development, microstructural features, quasi-static mechanical performance and the respective failure mechanisms. In this context, microscopy techniques (i.e. optical, confocal laser and scanning electron), X-Ray micro-computed tomography (microCT), lap shear and T-Pull testing were chosen for this purpose. FSp joints produced under HHI joining condition achieved an ultimate lap shear force (ULSF) 43 % higher than LHI joints, whereas HEI joints produced by FricRiveting process achieved ultimate tensile force (UTF) 46 % higher than LEI joints. The lap shear strength of ultrasonically joined joints produced under HEI joining condition was up to 85% higher than LEI joints. FSp joints failured in the center of the overlap area while friction-riveted joints failured through the rivet (HEI) and full rivet pull-out (LEI). Ultrasonically joined joints failured “through the polymer” (HEI), whereas LEI joints failured through a combination of shearing of the metallic pins and a mixed cohesive (CF) and adhesive (AF) failure.

Keywords

Friction spot joining (FSpJ); friction Riveting (FricRiveting); ultrasonic joining (U-Joining); hybrid structures; micro-computed tomography.

Resumo

Pinto, Raphael Pereira; Paciornik, Sidnei. **Avaliação não-destrutiva, microestrutural e desempenho mecânica de juntas hibridas produzidas com metal e polímero**. Rio de Janeiro, 2017. 119p. Dissertação de Mestrado - Departamento de Engenharia Química e de Materiais, Pontifícia Universidade Católica do Rio de Janeiro.

A indústria de transporte tem enfrentado rigorosas políticas econômicas e ambientais para a redução do consumo de combustível e consequentemente redução na emissão de CO_2. Uma solução promissora para suprir tais exigências encontra-se na redução do peso da estrutura de carros e aviões através do uso de estruturas híbridas. Técnicas de união convencionais geralmente são inadequadas para produzir juntas híbridas de metal e polímero. Sendo assim, tecnologias de junção inovadoras estão sendo desenvolvidas para surprir tais limitações, como por exemplo: União pontual por fricção (FSpJ), rebitagem por fricção (FricRiveting) e união por energia ultra-sônica (U-Joining). Esta dissertação de mestrado foi desenvolvida para avaliar juntas híbridas produzidas com baixo (BAE) e alto aporte energético (AAE). O monitoramento da temperatura, a análise microestrutural, a resistência mecânica e os respectivos modos de falhas das juntas foram avaliados para as três técnicas de fricção. Neste contexto, técnicas de microscopia, microtomografia de raio-x e ensaios de resistência mecânica foram escolhidas para tal finalidade. Juntas de AAE produzidas por união pontual de fricção apresentaram 43 % maior resitência mecânica comparado com juntas de BAE e ambas falharam no centro da área de junção. Juntas de AAE produzidas por rebitagem apresentaram 46 % maior resitência mecânica e falha do rebite metálico fora da placa polimérica, comparado com juntas de BAE que teve o rebite metálico arrancado da placa polimérica. A resitência ao cisalhamento das juntas de AAE (fratura da placa polimérica) produzidas por energia ultra-sônica foi 85 % maior que as juntas de BAE (fratura dos pinos combinado com falhas coesivas e adesivas).

Palavras-chaves

União pontual por fricção; rebitagem por fricção; união por energia ultrassônica; estruturas híbridas; microtomografia computadorizada.

Table of Contents

List of figures

List of Tables

1
Introduction

The transportation industry has been facing stringent environmental regulations to decrease fuel consumption and CO_2 emissions. A promising solution to fulfill these demands is decreasing the structural weight of vehicles and airplanes by combining lightweight alloys and fiber-reinforced polymers in hybrid structures [1]. In the aircraft industry, for instance, the Boeing 787 has 50 wt% of composite materials, 20 wt% of aluminum and 15% of titanium in its airframe and primary structures [2, 3]. The Airbus A350 XWB is composed of 53 wt% composites and 14% of aluminum in the main structures which led to a reduction of 25% in fuel consumption [4, 3]. The KC-390, the military transport aircraft produced by Embraer, uses lightweight ballistic protection solutions provided by composite materials [5]. In the automotive industry, for example, BMW and Audi one of the largest vehicles manufacturer have also adopted the use of lightweight alloys and fiber-reinforced polymers in hybrid structures [6,7].

Conventional welding-based technologies are usually inadequate to produce high-performance metal-polymer hybrid joints due to the physical and chemical material dissimilarities [8]. Currently, the most used technologies to join metal-polymer hybrid structures are mechanical fastening and adhesive bonding [1,9]. However, these technologies have shown some limitations which urge the development of new technologies for such purpose. The main limitations in mechanical fastening are weight penalty, stress concentrations and damage of reinforcing fibers induced by drilling, whereas adhesive bonding requires extensive surface preparation and curing time of the thermoset adhesive [10, 11]. Thus, due to these limitations, some alternative welding-based techniques have been developed with different advantages and drawbacks (i.e. resistance, induction, ultrasonic and laser welding) [12].

Resistance welding uses an electrical element or implant such as a metal mesh or carbon tip, between the joining parts [13]. These welding-based techniques are

cheap and can be used to weld most thermoplastic-based materials. Nevertheless, additional heating elements and long welding cycles (1-11 minutes) are some disadvantages reported in the literature [14].

In induction welding, the heat is generated at the polymer-composite interface by an alternating current electromagnetic field produced by a coil and the joint is consolidated under pressure, resulting in a weld [15]. Strong joints are produced by this technique. However, some drawbacks have been listed such as high cost of the insert materials, long welding cycles (1-4 min), non-uniform heat distribution at the bond line, difficulty of welding large parts and expensive equipment [15, 16].

Ultrasonic welding uses high frequency vibration of a tool to generate frictional heat on the welding pieces. It has been reported that ultrasonic welding presents high energy efficiency, with a clean and fast process (1-4 s). However, the welding equipment is expensive and can be applied only to thin metal sheets [15,17].

Laser welding uses a laser beam transmitted through a transparent material and absorbed at the top surface of a non-transparent material. By heat conduction, the interface is heated and the polymer is melted [18]. However, the laser welding equipment is expensive and high volume of defects are generated at the joint interface due to the polymer degradation [19].

Due to the limitations related to the mechanical fastening, adhesive bonding and welding-based techniques as well as the increasing importance of joining metal-composite hybrid structures, advanced joining technologies are under development to overcome these limitations.

In the present work, metal-polymer/composite hybrid joints were produced using three new friction-based joining techniques developed at Helmholtz-Zentrum Geesthacht (HZG), Germany: Friction Spot Joining (FSpJ [20]), Friction Riveting (FricRiveting [21]) and Ultrasonic Joining (U-Joining [22]).

Two joining conditions with different heat input levels (low and high) were selected to produce hybrid joints for each joining technology. Microscopy techniques (*i.e.* optical, confocal laser and scanning electron), X-Ray micro-computed tomography (microCT), local (microhardness) and global (T-Pull and lap shear testing) mechanical performance were selected to understand the joint

formation, process-related changes of internal features and their correlation with joint mechanical performance. The failure mechanisms were also evaluated and correlated with the microstructural features and mechanical performance of the friction-based joints.

This MSc dissertation is structured as follows. After this introduction the objectives of the work are presented in Section 2. Section 3 briefly reviews the state-of-the-art literature on Friction Spot Joining (FSpJ), Friction Riveting (FricRiveting), Ultrasonic Joining (U-Joining) and X-Ray micro-computed tomography (μCT). Further, the technical details of the materials used as joining parts and the experimental methods used to produce and characterize the joints are described in Section 4. The main results obtained and the respective discussions are presented in Section 5. This Section is divided into three parts, the evaluation of FSpJ, FricRiveting and U-Joining. Finally, the conclusions and the recommendations for future work are given in Section 6 and Section 7, respectively.

2
Objectives

This work aims at evaluating the influence of different energy input levels on the hybrid joint internal features produced by three different friction-based joining techniques: Friction Spot Joining (FSpJ), Friction Riveting (FricRiveting) and Ultrasonic Joining (U-Joining). The following specific objectives were defined for this work:

- Understand the joint formation along with process-related microstructural changes, temperature evolution as well as global and local mechanical properties.
- Analyze the process-related changes by high-resolution tridimensional microCT characterization of the hybrid joints' internal features (i.e. process-related joint geometrical changes, thermomechanical-induced flaws and interface quality).
- Correlate the microstructural features with the joints' mechanical performance (quasi-static mechanical testing) and the respective failure mechanisms.

3
Literature Review

This section presents a brief literature review of the friction-based joining techniques for metal-polymer hybrid structures used in the present work. Additionally, X-Ray micro-computed tomography is described as a non-destructive technique to characterize the joint microstructural features in three dimensions.

3.1.
Joining process

3.1.1.
Friction Spot Joining

Friction Spot Joining (FSpJ) is an innovative friction-based joining technology (European Patent 2329905B1, 2012 [20]) for producing overlap joints in metal-polymer/composite hybrid structures [23]. The technique uses a tool (Figure 1) comprised by three pieces: a pin, a sleeve and a clamping ring, which have independent rotational and axial actions. The process has two variants: sleeve plunge and pin plunge. The steps of the process for both variants are similar. However, the sleeve plunge variant has been more widely used because of the larger joining area and higher joint strength achieved. For this reason, the sleeve plunge variant was used in this work [24].

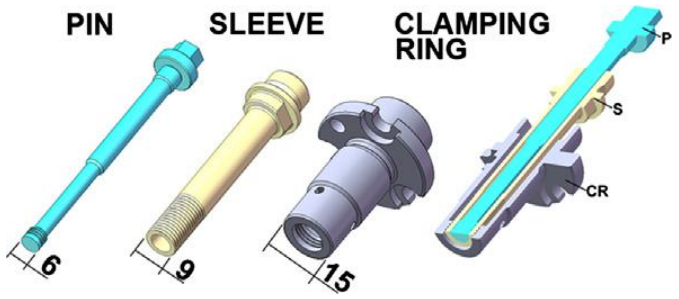

Figure 1 - FSpJ tools used in this study (dimensions in mm) (Adapted from [24]).

Figure 2 schematically illustrates the FSpJ process for the sleeve plunge variant. Prior to the joining process, the parts are clamped in an overlap configuration (aluminum on top of composite) between a backing plate and the clamping ring to avoid the separation of the parts during the joining process. In the first step (Figure 2-1) the rotating sleeve is plunged into the metallic part to a predefined position. The plunging of the sleeve is restricted to the metal part to avoid or reduce polymer degradation and damages to the fiber network in the case of composites. Simultaneously, the pin is retracted forming a deposit. The volume of metal plasticized due to the friction between sleeve and metal flows into this deposit. In the second step (Figure 2-2) the pin pushes back the plasticized metal and the keyhole formed by the sleeve plunging is refilled. Finally, the tool used during the process is removed (Figure 2-3) and the spot joint consolidates under pressure [24].

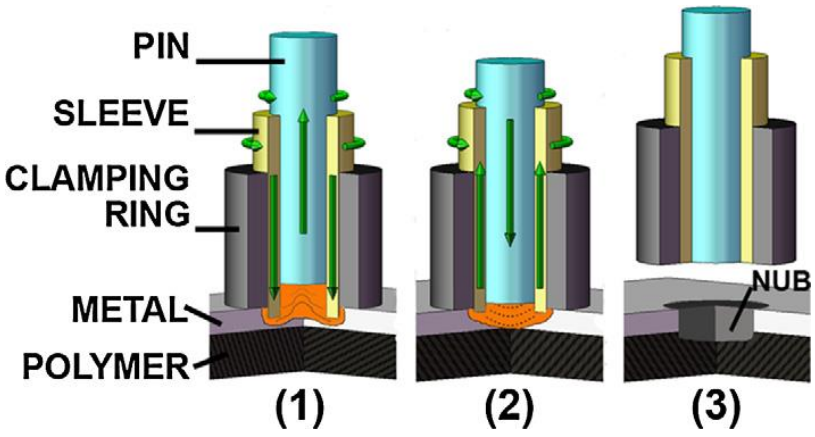

Figure 2 - Schematic illustration of the FSpJ process steps (sleeve plunge variant) for a metal-composite hybrid joint. (1) Sleeve plunging and metal plasticizing; (2) spot refilling and (3) joint consolidation (Reproduced from [24]).

The FSpJ process has four main process parameters: rotational speed (RS), plunge depth (PD), joining time (JT) and joining force (JF). RS and JT are responsible for the heat generation and temperature evolution during the process while PD controls the shape of the inserted volume of metal into the polymer/composite part. JF defines the pressure applied during the process to avoid the separation of the joining parts and also controls the flow of molten polymer at the metal-composite interface [25].

Mechanical interlocking and adhesion forces are the main bonding mechanisms responsible for the joints strength in FSpJ. The plasticized metal is deformed by the tool plunging movement and slightly inserted into the composite part, improving the joint strength under shear loading. This geometrical feature is called “metallic nub” and it is responsible for the macro-mechanical interlocking between the parts [24]. The entrapment of polymer matrix and fibers into the irregularities of the metal surface also creates a micro-mechanical interlocking between the two parts, improving the joint strength under loading. In addition, adhesion forces are established at the metal-composite interface by a thin layer of reconsolidated polymer matrix, which was softened as a result of the generated frictional heat [26].

Different materials have been successfully joined by friction spot joining:

Amancio-Filho *et al.* [24] investigated the feasibility of the FSpJ technology for AZ31-O/GF-PPS and CF-PPS joints. The authors observed change on the local mechanical performance of composite and metal parts as a result of the grain refinement by dynamic recrystallization of the AZ31-O induced by the FSpJ process, while the PPS structure was altered by annealing. Joints without surface pre-treatment of the parts showed an increased average ultimate lap shear strengths of 20 to 29 MPa.

Goushegir *et al.* [26] studied the microstructural features and mechanical strength of Al 2024-T3/CF-PPS joints. The author identified three zones in the fractured surface of the FSp joints: macro- and micro-mechanical interlocking and adhesion forces. The effectiveness of the aluminum surface pre-treatment was evaluated. The lap shear strength increased up to 31 MPa (bare) and 43 MPa (alclad) due to the increase in the wettability of the aluminum surface and the micro-mechanical interlocking.

Esteves *et al.* [27] evaluated the influence of the FSpJ parameters on the mechanical performance and microstructure of double lap Al 6181-T4/CF-PPS joints. The authors used the Taguchi design of experiments (DoE) and ANOVA to analyses the influence of the FSpJ process parameters on the mechanical performance of the joints. Joints produced by using low frictional heat (1200 rpm; 0.75 mm, 2s; 6.8 kN of joining force) showed an ultimate lap shear force of (2107 ± 470 N) while joints produced with high frictional heat (1600 rpm, 1.15 mm, 6s;

8.3kN of joining force) achieved (3523 ± 527 N). Taguchi analysis indicated rotational speed as the parameters which has the largest influence on the lap shear strength, followed by joining time, plunge depth and joining pressure.

In another work, Esteves *et al.* [28] observed the strong influence of the aluminum surface pre-treatments on the mechanical performance of FSpJ of Al 6181-T4/CF-PPS joints. Natural aluminum oxide layer was removed manually of the aluminum surface by grinding (SiC paper, P1200), increasing the roughness of the aluminum. In addition, to increase the wettability of the aluminum surface with the molten polymer during the joining process, acid pickling was also investigated. Aluminum was etched with nitric acid for 30 minutes leading to a lap shear strength of 29 MPa while the strength decreased to 11 MPa when the grinding procedure was applied.

André *et al.* [29] investigated the feasibility of FSp joints of Al2024-T3/CF-PPS with a PPS film interlayer. Mechanical grinding, sandblasting and plasma activation were performed on the composite part. Sandblasting led to a better micro-mechanical interlocking between the molten PPS film and the composite surface as well as the highest joint strength. The addition of an interlayer resulted in increases of up to 55% in the ultimate lap shear force compared to the FSp joints without film. The joints produced with the interlayer showed an average lap shear strength of (2703 ± 114 N) for the high and (3069 ± 166 N) for the low heat input joining conditions.

The current studies, among several others have been demonstrated that friction spot joining can be successfully used to join materials chosen for structural applications in transportation companies.

3.1.2. Friction riveting

Friction Riveting [21] (FricRiveting, in short) is an alternative friction-based joining technology [21] developed for metal-polymer/composite hybrid structures which relies on the principles of mechanical fastening and friction welding [30]. The joining parts are composed by a rotating metallic rivet and a stationary polymeric base plate which can be joined in different configurations. The simplest configuration is the metallic-insert joint where the rivet is inserted and mechanically

anchored into a single polymeric or composite plate. More configurations such as overlap and sandwich-type combine multiple base plates made of polymer, composite or metal inserted by the rivet [31].

The simplest description of the process is for metallic-insert joints, as shown in Figure 3. Prior to the joining process, the stationary polymeric part is clamped over the table of the frictional welding machine, while the metallic rivet is fixed into the friction head, *i.e.* in the chuck (Figure 3-A). Subsequently, the rivet is rotated, pressed against the stationary polymeric base plate and inserted (Figure 3-B). High rotation and pressure generates frictional heat which rises locally the temperature at the rivet tip. Such temperature overcomes the transition temperatures of the polymer (*i.e.* glass transition temperature for amorphous thermoplastics and melting temperature for semi-crystalline thermoplastics) leading to the formation of a thin softened/molten polymeric layer around the rivet tip.

Due to the rivet insertion into the polymeric base plate, a volume of softened/molten polymer is expelled outward of the joining area, as a flash. At the end of the frictional phase, the rotation is decreased to zero while axial force is increased (Figure 3-C), initiating the so called forging phase. The cold polymer underneath the rivet tip creates a resistance to the rivet penetration contributing to plastically deform the metal and, hence, increasing the original rivet diameter [30]. Recent work [33] has shown the possibility of achieving the mechanical anchoring of the rivet without the forging phase by generating enough heat at the frictional phase to enable the rivet plasticizing and plastic deformation. Finally, the joint is consolidated under pressure (Figure 3 - D).

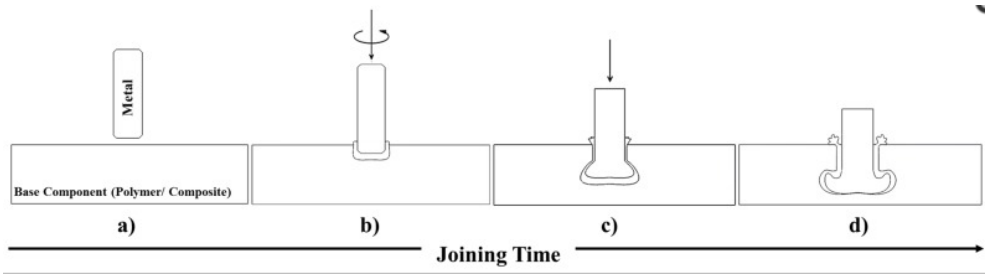

Figure 3 - Schematic illustration of the FricRiveting process steps. a) Positioning of the joining parts. b) Insertion of the rotating rivet into the polymeric base plate. c) Plasticizing and forging of the rivet tip. d) Joint consolidation (Adapted from [32]).

FricRiveting can be controlled by time, force, displacement or the combination of these variants [33]. The most consolidated process variant is the time-control process limited by time, which has as monitoring process parameters the rotational speed (RS), friction force (FF), forging force (FOF), friction time (FT) and forging time (FOT). The rotation speed is the angular velocity of the rotating rivet which has an important influence on the temperature development and heat generation. The friction force and forging force are related to the normal pressure distribution in the frictional area, while friction time and forging time influence the frictional heating and consequently the level of rivet plastic deformation and volumetric defects caused by thermo-mechanical processing [34]. For other process variants, other parameters must be considered such as the displacement at friction (DF) which is the rivet insertion depth at the friction phase.

Mainly two joining mechanisms can be identified for friction-riveted joints: mechanical anchoring related to the deformed tip of the rivet into the thermoplastic component and adhesive forces established in the metal/polymer interface [34]. The feasibility of Friction Riveting has been successfully demonstrated for metallic-inset hybrid joints of material combinations selected for structural applications in transportation companies, including titanium alloys joined with carbon-fiber reinforced polymers [35].

Amancio-Filho [34] investigated the feasibility of the PEI/AA2024-T351 friction-riveted joints. The author correlated the average process temperatures achieved (300ºC to 500ºC) with the mechanical performance of the joints. The combination of high temperature and applied force led to an outstanding mechanical performance of the joints, reaching about 89% of the tensile strength of the rivet base material.

Rodrigues *et al.* [36] demonstrated the feasibility of polycarbonate/AA2024-T351 friction-riveted joints produced in a metallic-insert configuration by analyzing the mechanical performance and microstructural properties. The authors observed satisfactory mechanical performance due to the effective anchoring of the rivet into the polymeric plate. Joints produced with PC/AA2024-T351 demonstrated ultimate tensile force between (6659 ± 62 N) and (8540 ± 182 N).

Blaga *et al.* [37] studied the feasibility of GF-PEI/Ti gr. 2. The influence of the rotational speed on the mechanical performance and joints formation was

evaluated based on three different joining conditions. The authors observed that joints produced with high rotational speed (10000 rpm) increased approximately 16.5% on the deformation of the rivet tip compared with joints produced with lower rotational speed (8000 rpm). The highest volumetric ratio (simplified analytical model describing the anchoring efficiency of the rivet) achieved for joints produced with 10000 rpm led to the highest ultimate tensile force (4 kN). In addition, the process parameters were optimized to reduce the amount of volumetric flaws in the anchoring zone as well as damage in the fiber network of the fiber woven reinforcement glass.

Altmeyer *et al.* [35] studied the effect of the friction riveting process parameters on the joint formation and mechanical performance of commercial pure titanium grade 3 (Ti gr. 3) and short-carbon-fiber reinforced polyether-ether-ketone (PEEK-30CF). The authors showed that high rotational speed, friction time and forging pressure led to higher pull-out forces. Increasing these parameters more energy for the plastic deformation of the titanium rivet tip was provided. The deformed rivet tip was correlated with the mechanical performance of the joints. Mechanical strengths up to 10.7 kN were achieved for joints with higher width of the plastic deformation in the rivet tip.

Borba *et al.* [38] addressed the feasibility of the FricRiveting technology for pultruded glass-fiber reinforced polyester plates and Ti-6Al-4V rivets. The author observed microvoids in the thermo-mechanically affected zone. In addition, two zones were also observed in the polymer thermo-mechanically affected zone (PTMAZ) based on the extension of the process-related damages on the fiber-network and matrix. Ultimate lap shear forces up to 8.3 kN were achieved for the friction-riveted joints produced with Ti-6Al-4V/P-GF.

3.1.3. Ultrasonic joining

Ultrasonic joining (U-Joining, to short) is a new direct-assembly technique developed by Helmholtz-Zentrum Geesthacht (European Patent Application EP3078480A1, 2015 [22]). This technology uses ultrasonic energy to join polymers-composites to surface-structured metallic parts (MIMStruct) produced by metal injection molding (HZG's patent EP 2 468 436 B1 [39]). As a result, a metal-

composite hybrid joint with improved out-of-plan mechanical strength is achieved [40].

The friction-based joining process (U-Joining) is divided through five joining steps (Figure 4). Firstly, the parts are clamped in a single-lap configuration (MIM-structured pins configured to touch the polymer surface) (Figure 4-1). In the second step, the sonotrode go down applying clamping pressure and the ultrasonic vibration initiates (Figure 4-2). Subsequently, the vibrational is transferred to the interface between the polymer and composite parts. The vibration motion combined with joining pressure create frictional heat, softening a thin layer of the polymer matrix around the pins, allowing a smooth penetration of the metallic part. Finally, the pins are inserted in the polymer/composite part (Figure 4-3). When the pins are fully plunged and the MIM-structured surface is wetted by molten polymer, the sonotrode vibration stops (Figure 4-4) and the joining process is completed. Finally, the sonotrode is retracted from the metal-polymer/composite hybrid joint (Figure 4-5) [40, 41].

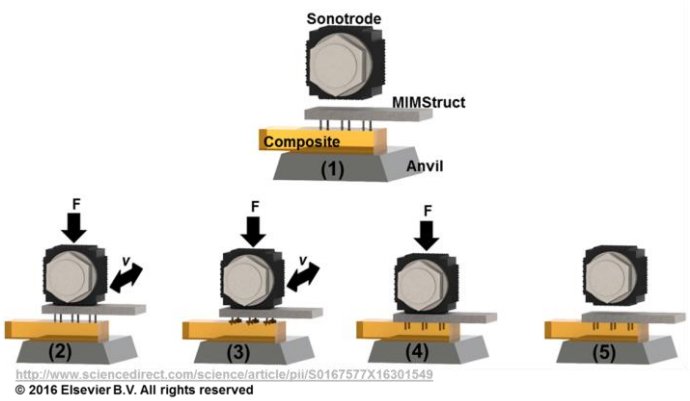

Figure 4 - Schematic illustration of the U-Joining process. (1) Positioning of polymer and composite parts. (2) Ultrasonic vibration and axial force applied. (3) Polymer softened by frictional heat at the pin-polymer interface and onset of the plunge of the pin. (4) Polymer consolidated under pressure and (5) Retraction of the sonotrode (Reproduced from [40]).

There are four main process parameters controlled during the U-Joining process: joining energy, joining force, clamping force and oscillation amplitude [41]. Two bonding mechanisms are responsible for the bonding area: mechanical interlocking and adhesion forces created at the metal-polymer interface [40].

Feistauer *et al.* [41] introduced ultrasonic joining as a new direct-assembly technique for metal-composite hybrid structures. The authors addressed the technology feasibility for metal injection molded Ti-6Al-4V/glass-fiber-reinforced polyetherimide joints. They demonstrated that, the ultrasonic energy-based technique can be used to produce metal-composite hybrid structures. The new joining process developed by HZG presented very short joining cycles and is an excellent solution to join damage-tolerant and crash-resistant hybrid structures.

In another work, Feistauer *et al.* [40] investigated the U-Joining feasibility of through-the-thickness reinforced Ti-6Al-4V and unreinforced polyetherimide (PEI). The author reported that the through-the-thickness reinforcement (conical pins structured by MIM) was completely inserted into the PEI plate, with the following set of joining parameters: 2000 J of joining energy, 42 µm of amplitude and 15 psi of joining pressure. Additionally, the measured process temperature (362 ± 32°C) was within the degradation range of PEI. The joining cycles were very short (1.26 ± 0.04 s) and thus no extensive degradation of the polymeric part is expected, according to the authors. Moreover, a significant increase of about six times in ultimate lap shear force was observed in comparison to non-reinforced reference joints.

3.2. X-Ray micro-computed tomography

X-Ray micro-computed tomography (microCT, in short) has been an alternative technique used within the material science community to obtain 3D digital information of materials [42]. This method has a period of faster development over the last 15 years with considerable advances in spatial resolutions and image reconstruction methods. As a non-destructive technique, microCT has a great potential to improve the amount of information that can be gleaned from 3D imaging, being tested successfully on a vast range of materials, such as rocks, polymers, ceramics and metals [43].

The principle of microCT is shown in the schematic illustration in Figure 5. Basically, to produce a three-dimensional microCT image, a whole set of two-dimensional projections need to be acquired. Prior to the measurement, the sample is placed on a turntable object stage between the X-Ray source and a detector [44].

The sample is rotated through 360º with a certain angular increment while an X-Ray beam is emitted by the X-Ray source. The X-Ray beam is transmitted through the sample along many different paths and directions. Several interactions can occur between the X-Ray beam and the sample, varying the X-Ray attenuation [45]. Due to the correlation between X-Ray absorption and material density, 3D internal features can be inferred and visualized from the images. Thus, yielding an image which displays differences in density at thousands of points in a sequence of 2D slices through the sample [46].

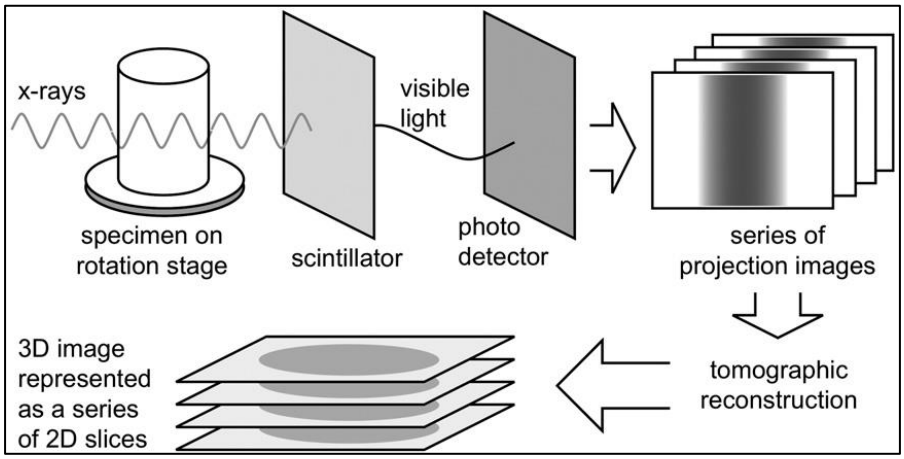

Figure 5 - Schematic illustration of X-Ray micro-tomography processes. A series of X-Ray projection images is acquired and mathematically reconstructed to produce a 3D map of X-Ray absorption in the volume (Adapted from [44]).

As discussed previously in Section 3.1 [24, 26, 27, 34, 35, 36, 40, 41] several studies have shown the influence of microstructural changes (*i.e.* voids, metallic fragments, agglomerates, plastic deformation) induced by the joining process (FSpJ, FricRiveting and U-Joining) on the global mechanical performance of the hybrid joints based on 2D characterization analysis (conventional microscopy). Two dimensional analysis can provide detailed images of the representative internal features and microstructure of the joints, but is limited to only one plan of the specimen and most of the times requires destructive specimen preparation. In order to better understand the correlation between internal features and joints' mechanical performance, it is necessary to perform a non-destructive evaluation through 3D images. The images in high-spatial resolution allow a detailed evaluation of the

microstructural changes. Only few studies have been performed to investigate hybrid joint properties by microCT.

Amancio-Filho [30] introduced Friction Riveting as a new joining technique for polymer-metal multi-materials structures. The author used microCT to evaluate the influence of the joining parameters on the joint formation and features of the friction-riveted joints in three dimensions. The author concluded that, the internal flaws tend to be concentrated around the non-deformed rivet volume for joints produced with small rotation speed (RS), joining time (JT) and joining pressure (JP). Joints produced with higher RS, JT and JP presented flaws distributed in the polymeric volume around the whole rivet (Figure 6). Such result was further used to explain the mechanical performance of the joints.

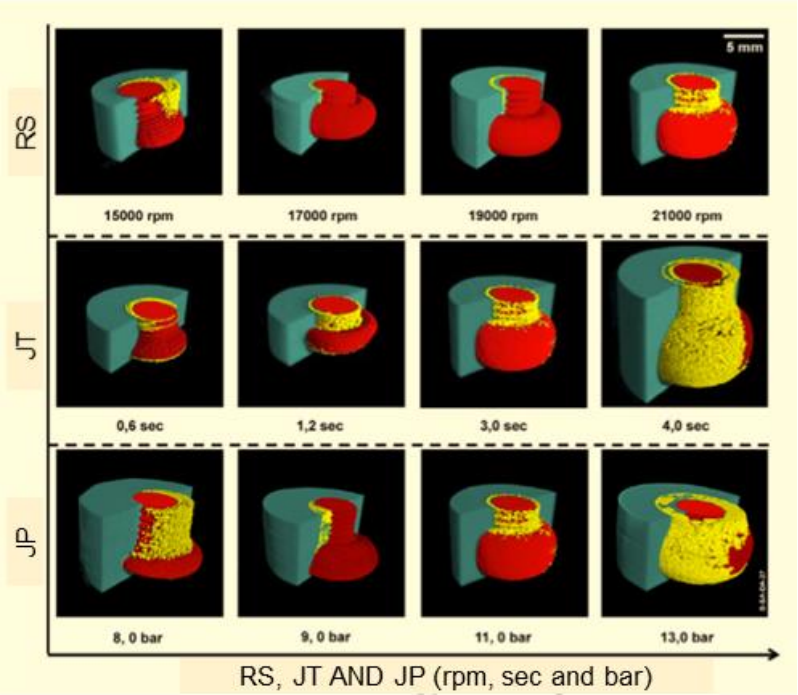

Figure 6 - 3D images of friction-riveted joints produced with different joining parameters and evaluated through microCT. Internal flaws are presented by yellow volumes while deformed rivet is in red and polymeric plate in green (Adapted from [30]).

Gude *et al.* [47] studied thermoclinching as a novel joining process for lightweight structures in multi-materials design. For an improved understanding of the composite fiber reorientation inside the joint and during the joining process, the

authors used microCT to analyze the microstructure of the material (Figure 7). The author concluded that the deformed reinforcement network was relocated into the neck and head area of the joint, which has a considerable contribution to the mechanical strength of the joints. Joints produced with reinforced thermoplastics withstood up to 50% higher loads compared to joints produced with no-reinforced thermoplastics.

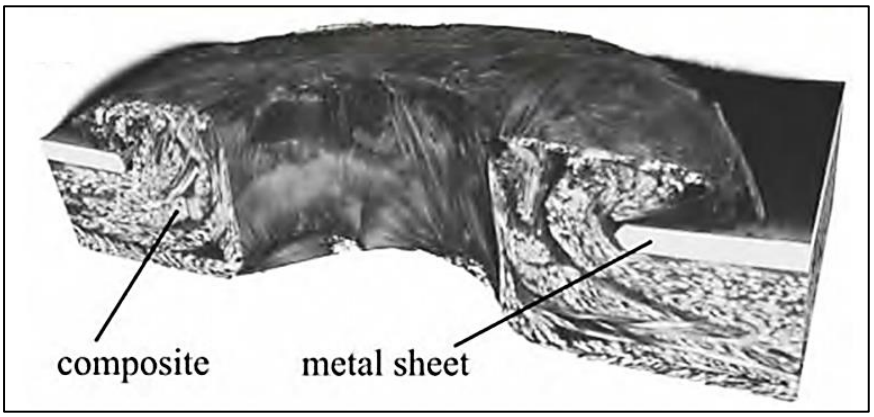

Figure 7 - Analysis of thermoclinched joint microstructure by microCT analysis (Adapted from [47]).

Abibe [48] introduced Friction-based Injection Clinching Joining (F-ICJ) process as an alternative technique to join multi-materials structures. The author used microCT to visualize the cavity filling of F-ICJ joints. Joints with high effective cavity filling achieved superior mechanical strength under lap shear testing as well as formed a slightly wider stake head, which contributes to the better joint mechanical performance of the joints.

In another work, Abibe *et al.* [49] investigated the mechanical and failure behavior of overlap metal-polymer staked joints. MicroCT post mortem analysis was performed to investigate the failure mechanism of ICJ joints tested through lap shear testing. The author observed, based on 3D images obtained by microCT, two failure modes: net tension and rivet pull-out, and explained that both are related to the bearing of the formed rivet against the internal walls of the hole in the metallic plate. In addition, they concluded that the mechanical performance of ICJ joints produced in this preliminary study was satisfactory.

4
Materials and Methods

Section 4 presents a description of the main properties of the materials used in this work as well as the methods used to produce and evaluate friction-based hybrid joints. The joints were produced at the Helmholtz Zentrum Geesthacht (HZG), Germany, and evaluated in cooperation with the Department of Chemical and Materials Engineering at PUC-Rio, Brazil.

4.1.
Base Materials

4.1.1.
Friction Spot Joining

4.1.1.1.
Aluminium Alloy 2024-T3 (AA2024-T3)

Two-millimeter-thick rolled aluminum alloy 2024 bare sheets in condition T3 (supplied by Constellium, France) were used as the metallic part for producing the joints. This alloy was chosen due to its excellent tensile strength (up to 435 MPa in T3 condition), good fatigue resistance and fracture toughness [50]. Copper (in the range of 3–6 wt. %) and magnesium (in the range of 1.2–1.8 wt. %) are the main alloying elements [51]. The microstructure of this alloy in the rolling direction is shown in Figure 8. The black spots are microvoids generated by the chemical removal of intermetallic (secondary) particles during the hardening process of the alloy based on controlled precipitation. The matrix is composed by elongated grains in the rolling direction of the alloy.

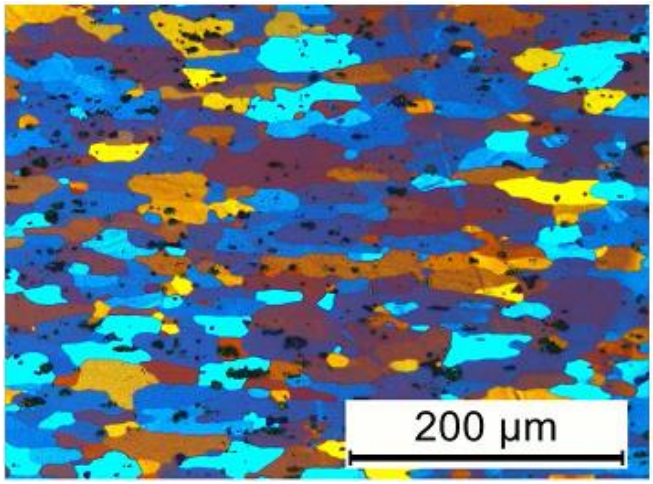

Figure 8 - Microstructure of AA2024-T3 (Reproduced from [52]).

This aluminum alloy has been used in the aeronautical industry due to its good machinability, conformability and surface finish capabilities, in applications where stiffness and good fatigue performance are required. Furthermore, the AA2024-T3 has also been applied in truck wheels, scientific instruments and screw machines products [50]. Table 1 [51] displays some of the main mechanical and physical properties of the AA2024-T3 used to produce the friction spot joints.

Table 1 - Main properties of the AA2024-T3 used in this work.

Property	**Value**
Tensile strength	435 MPa
Tensile modulus	70 GPa
Hardness	137 HV 0.2
Thermal conductivity	121 (W m^{-1} K^{-1})
Incipient melting temperature	502 °C
Density	2.78 g cm^{-3}

4.1.1.2.
Carbon-Fiber-Reinforced Polyphenylene Sulfide (CF-PPS)

The composite laminate used in this work (CETEX®, supplied by Tencate, Netherlands [53]) is composed by a matrix of polyphenylene sulfide (PPS) reinforced with 43 wt% of carbon-fiber. The laminate sheet has a nominal thickness

of 2.17 mm. Figure 9 shows the cross-section of the CF-PPS composite laminate in the weft direction.

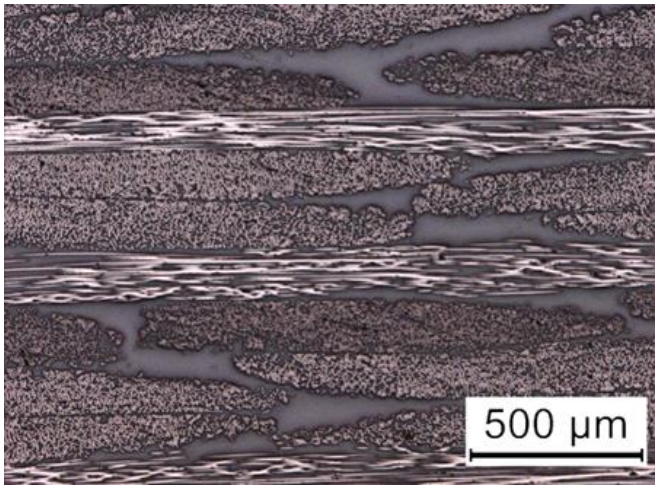

Figure 9 - Microstructure of CF-PPS (Reproduced from [52]).

The excellent mechanical strength of the carbon-fibers combined with the physicochemical and thermal properties of PPS result in a tough, rigid, chemical resistant, dimensionally stable, and weldable composite laminate. CF-PPS is a high performance engineering composite qualified by renowned companies for multiple structural applications, such as the "J-Nose" subframe wings of Airbus A340-500/600 [54]. Table 2 [53] lists the main mechanical and physical properties of the CF-PPS used to produce the friction spot joints.

Table 2 - Main properties of the CF-PPS used in this work.

Property	**Value**
Tensile strength	790 MPa (Warp) / 750 (Weft) MPa
Tensile modulus	53 GPa
In-plane shear strength	131MPa
Thermal conductivity	0.19 (W m^{-1} K^{-1})
T_g/T_m	120 °C/280 °C
Density	1.35 g cm^{-3}

4.1.1.3. Polyphenylene Sulfide Film (PPS)

The friction spot joints were produced using an additional film interlayer in between the metal and the composite to increase the mechanical strength of such joints [29]. The material employed is a 100 μm thick PPS film (supplied by LITE, P., Austria). This is a thermoplastic film, with low degree of crystallinity (7%) and presents high hydrolysis and chemical resistance. The main mechanical and physical properties of the PPS film used in this work are listed in Table 3 [55].

Table 3 - Main properties of the PPS film used in this work.

PROPERTY	VALUE
Tensile strength at 23 °C	85MPA
Tensile modulus	2.4 GPa
Thermal conductivity	0.24 (W m^{-1} K^{-1})
T_g / T_m	92 °C / 280 °C
Density	1.33 g cm^{-3}

4.1.2. Friction Riveting

4.1.2.1. Extruded Ti-6Al-4V

Extruded Ti-6Al-4V rivets (supplied by HENSCHEL, Germany) with 5 mm diameter and 60 mm length were used as metallic joining part, due to their high specific strength, good corrosion and creep resistances. Aluminum (6.2 wt. %) and vanadium (4.5 wt. %) are the main alloying elements [56]. Figure 10 shows a typical microstructure of the Ti-6Al-4V in the longitudinal direction of extrusion. The morphology of the alloy is composed by equiaxed α-grains (Al enriched phase) with β-grains (V enriched phase) in their boundaries.

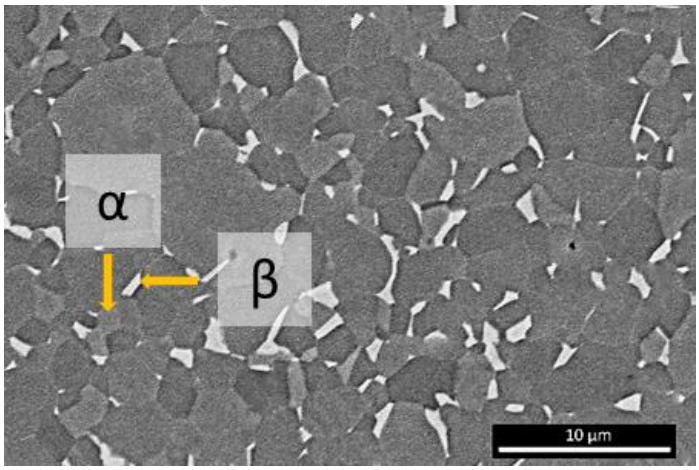

Figure 10 - Microstructure of extruded Ti-6Al-4V.

Ti-6Al-4V alloy, commonly called titanium grade 5, has been widely used in automotive, aeronautical, aerospace, medical, petrochemical and energy applications [57, 58]. Due to its high specific strength, excellent toughness, fatigue resistance at elevated temperatures and good resistance to corrosive environments, the material has been used in main parts of the Boeing 757 such as fasteners and engine components [59, 60]. Table 4 summarizes the main mechanical and physical properties of the Ti-6Al-4V used in the friction-riveted joints.

Table 4 - Main properties of TI-6Al-4V [56, 61].

Property	**Value**
Ultimate Tensile strength	950 MPa
ß-*Transus* temperature	995 MPa
Hardness	349 $HV_{0.5}$
Thermal conductivity	6.7 ($W\ m^{-1}\ K^{-1}$)
T_m	1660 °C
Density	4.43 $g\ cm^{-3}$

4.1.2.2.
Carbon-Fiber-Reinforced Polyether-Ether-Ketone

The composite used as polymeric plate of the friction-riveted joint is a 21.2 mm plate of polyether-ether-ketone reinforced with 30 wt% of short carbon-fiber

(PEEK-30CF) (KETRON®, supplied by Arthur Krueger, Germany). The outstanding properties of the material include high strength, toughness along with wear, heat and chemical resistance at elevated temperatures [37, 62]. Figure 11 depicts the cross-section of PEEK-30CF, showing the random distribution of the fibers through the polymeric matrix.

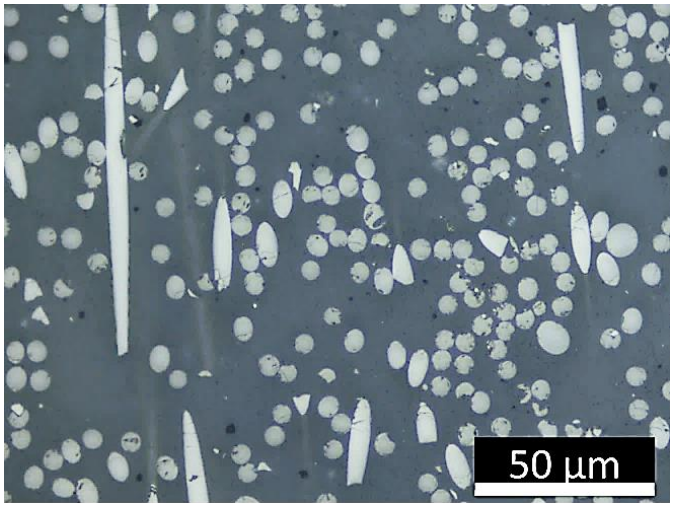

Figure 11 - Microstructure of PEEK-30CF.

PEEK-30CF has been extensively applied in automotive, aeronautical, and biomechanics industry as well as in robots and machines due to the high strength and low density as compared to conventional materials [62, 63]. Some of the main properties of 30% short-carbon-fiber-reinforced PEEK are listed in Table 5 [62].

Table 5 - Main properties of PEEK-30CF.

Property	**Value**
Tensile strength	130 MPa
Tensile modulus	7700 MPa
Hardness	35 $HV_{0.1}$
Thermal conductivity	0,92 ($W\ m^{-1}\ K^{-1}$)
T_m	334 °C
Density	1.41 $g\ cm^{-3}$

4.1.3.
Ultrasonic Joining

4.1.3.1.
Metal Injection Molded Ti-6AL-4V-0.5B

The 15.5 x 35 x 3 mm MIM-structured metallic part was produced with Ti-6Al-4V-0.5B alloy by metallic injection molding [39]. The metallic parts present six round-tip conical pins 3 mm high [41]. The addition of boron (0.5 wt% in weight) to the conventional Ti-6Al-4V alloy leads to higher mechanical strength and fatigue resistance. It is a result of the microstructure with α colonies (lamellar structure) and α grains (equiaxed structure) generated with the boron addition compared to the fully lamellar microstructure in Ti-6Al-4V alloy [64]. Figure 12 shows the microstructure of MIMStruct Ti-6Al-4V-0.5B where borides in the form of needles are indicated by grey arrows. Table 6 [56, 64] lists selected mechanical and physical properties of the Ti-6Al-4V-0.5B used in the ultrasonic joints.

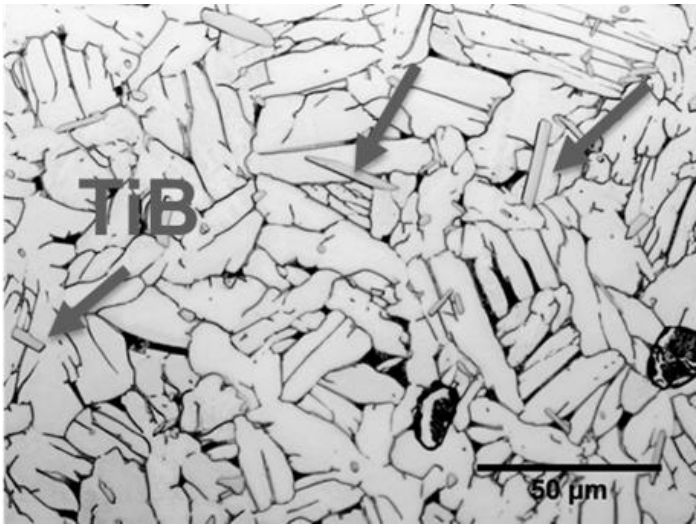

Figure 12 - Microstructure of MIM-structured Ti-6Al-4V-0.5B part.

Table 6 - Main properties of Ti-6Al-4V-0.5B.

Property	Value
ß-*Transus* temperature	995 °C
Residual porosity	1.7 ± 6%
Thermal conductivity	6.7 (W m^{-1} K^{-1})
Tensile strength	902 ± 2 MPa
Tensile modulus	787 ± 1 MPa

4.1.3.2.
Polyetherimide

The 15.5 x 35 x 6. 5 mm polyetherimide (Duratron U1000 PEI provided by Arthur Krüger, GmbH, Germany) was used as the polymeric part of the hybrid joint. PEI is a high-performance amorphous thermoplastic [65] and presents high mechanical strength and rigidity at room and elevated temperature, good long-term heat resistance as well as excellent dimensional stability [30]. The important chemical groups present in this polymer structure are aromatic imide (responsible for high thermal resistance and polymer stiffness), propylene and ether (good processability). Figure 13 shows the polyetherimide molecular structure.

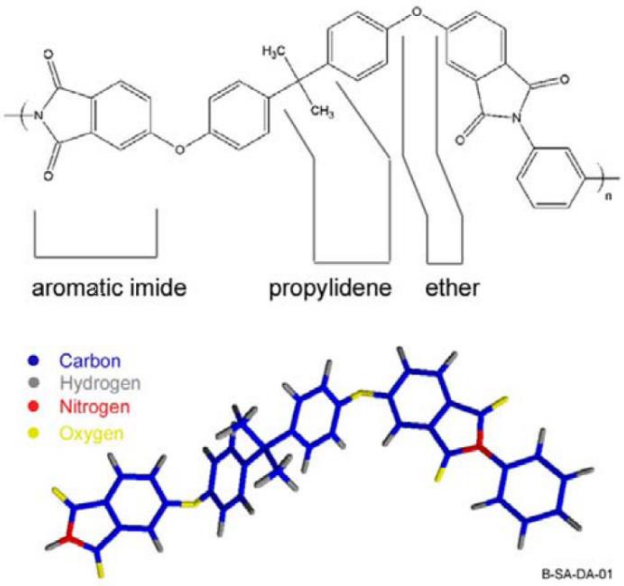

Figure 13 - Polyetherimide molecular structure (Reproduced from [30]).

The improved mechanical and physicochemical performance of PEI led to its use in several industrial applications such as automotive, electrical/electronic, aerospace (i.e. flooring, lighting, seating and other secondary and tertiary structures) [66], as well as in the medical industry [30]. Table 7 [30, 67] lists selected mechanical and physical properties of the polyetherimide used in the ultrasonic joints.

Table 7 - Main properties of the polyetherimide.

Property	Value
Tensile strength	100 MPA
Tensile modulus	3.4 GPa
Thermal conductivity	0.22 (W m^{-1} K^{-1})
Glass transition temperature (T_g)	215-220 °C
Thermal degradation:	
Stage 1: crosslinking	320-380 °C
Stage 2: chain scission	400 °C

4.2. Methods

4.2.1. Joining Procedures

4.2.1.1. Friction Spot Joining

AA2024-T3/PPS film/CF-PPS joints were produced with a displacement-controlled joining equipment (RPS 200, Figure 14) provided by Harms&Wende. The FSpJ tool (pin, sleeve and clamping ring) used in this work was made of Hotvar® (DIN 1.6358) and a special sample holder and clamping system were used to ensure an intimate contact between the parts during the joining process [68].

Surface pre-treatments were used on both aluminum and composite parts to improve the adhesion between these joining parts to the PPS film interlayer. Sandblasting was carried out using a Normfinish® equipment (Holland) in HZG

facilities. For this work, corundum (Al_2O_3) with average particles size of 100-150 μm was employed as the blasting medium. The distance between the samples and the pistol was fixed at 20 cm and the angle between the samples and the pistol was 45°. During the surface pre-treatments a pressure of 0.6 MPa and 10 seconds was used for the aluminum part and 0.3 MPa and 5 seconds for the composite part. The parameters of sandblasting were selected based on previous investigations [52].

Figure 14 - FSpJ machine RPS 200 (Reproduced from [69]).

Prior to the joining process, acetone was used to remove particles and debris from the aluminum surface as well as ethanol on the composite part. The joints were in an overlap configuration in such a way that CF-PPS was on the bottom, AA2024-T3 on the top and PPS film interlayer in between. The overlap area was 25.4 x 25.4 mm^2 as shown in Figure 15.

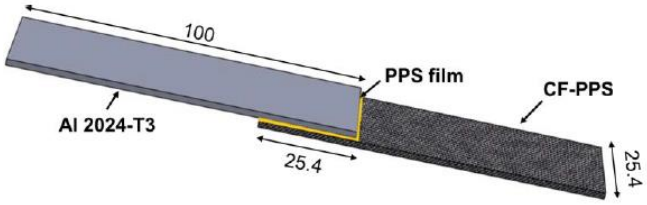

Figure 15 - Configuration and dimensions (in mm) of the Friction spot joining parts (adapted from [52]).

The joining parameters used in this work (Table 8) were selected based on previous investigations of AA2024-T3/PPS/CF-PPS joints [29], to evaluate the

effects of heat input on the internal features and mechanical strength of the joints. The low heat input condition was selected due to the small amount of internal flaws created during the joining process whereas the high energy input condition was chosen due to the better mechanical performance of produced joints.

Table 8 - Friction spot joining process parameters.

	Low heat input	**High heat input**
Rotational speed [rpm]	1900	2900
Plunge depth [mm]	0.8	0.8
Joining time [s]	4	4
Joining force [kN]	3	5

4.2.1.2.
Friction Riveting

Joining was performed using an automated FricRiveting gantry system (RNA, H. Loitz-Robitik, Germany), as shown in Figure 16. RNA consists of a spindle (i.e. friction welding head) and a tri-axial moving equipment coupled with several sensors including torque sensors, allowing precise monitoring of the joining parameters during the process and delivering forces up to 24 kN, rotational speed of 21000 rpm, and maximum axial torque of 20 Nm. Moreover, the equipment allows the process to be controlled and limited by force, time and displacement.

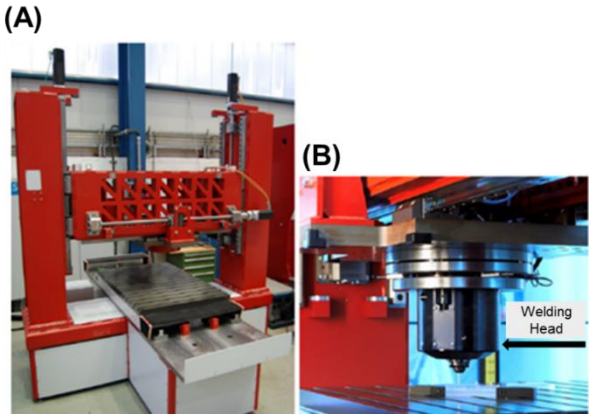

Figure 16 - RNA Friction Riveting system used to produce friction-riveted joints: (a) triaxial gantry system (b) welding head (Reproduced from [70]).

The joints were produced in a metallic-insert configuration, as shown in Figure 17. Prior to the joining process, the parts surfaces were cleaned with isopropyl alcohol to remove impurities.

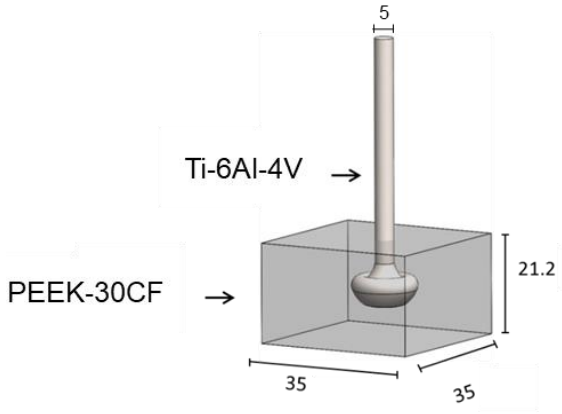

Figure 17 - Configuration and dimensions (in mm) of the FricRiveting joining parts.

A force-control process variant limited by displacement was adopted in this work. The joining parameters were selected based on previous studies [70], to investigate the effect of the applied mechanical work accomplished by the rivet during FricRiveting on the joint formation and mechanical performance. Table 9 summarizes the joining conditions used. In Appendix B, the monitoring curves of the joining parameters for each condition are presented.

Table 9 - Friction Riveting process parameters.

	Low energy input	**High energy input**
Rotational speed [rpm]	15000	20000
Displacement at friction [mm]	15	15
Consolidation time [s]	10	10
Friction force [N]	15000	15000
Energy input [J]	286 ± 9	310 ± 10

The energy input was calculated using equation 1 [71]. E_{total} is the total energy generated by the inserted rivet during the process which has frictional and axial contributions (E_{fr} and E_{ax}). M_z is the frictional torque associated to the rotation of

the rivet (N.m), w is the angular velocity (rad.s^{-1}), F is the axial force (N) and the burn-off rate is represented by v_0 (m.s^{-1}).

$$E_{total} = E_{fr} + E_{ax} = \int M_Z \, x \, w \, dt + \int F \; x \, v_0 \, dt \, [J] \qquad (1)$$

By increasing the rotational speed, the contribution of the energy generated by friction is increased. As reported by Amancio-Filho [72], the friction generated between the parts during the joining process has the most significant contribution in the heat generation during FricRiveting.

4.2.1.3.
Ultrasonic Joining

The equipment used during the ultrasonic joining process was a commercially available metal ultrasonic joining system, Ultraweld L20 metal welder (Figure 18), from Branson Ultrasonics. This equipment allows the control of the following process parameters: joining energy, joining and clamping pressures and sonotrode oscillation amplitude. Moreover, the Ultraweld L20 works with adjusted sonotrode amplitude (from 5 to 52 μm) and delivers joining power up to 4 kN. The sonotrode oscillation frequency in set at 20 kHz and cannot be modified. The equipment is coupled with several sensors that monitor the power and sonotrode displacement [40].

Figure 18 - Ultraweld L20 metal welder from Branson Ultrasonics (Reproduced from [73]).

Prior to the joining process, the parts surfaces were cleaned with isopropylic alcohol, to remove impurities or dirt. The overlap area of U-Joining joints was 15.5 x 21 mm, as shown in Figure 19.

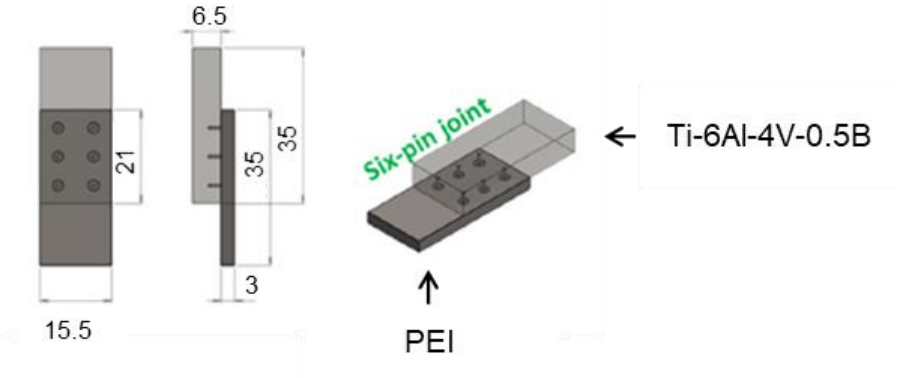

Figure 19 - Configuration and dimensions (in mm) of the U-Joining parts (adapted from [41]).

The joining parameters (Table 10) were selected based on an exploratory study performed with similar material (*i.e*. PEI and Ti-6Al-4V [41]).

Table 10 - Ultrasonic joining process parameters.

	Low heat input	**High heat input**
Joining Energy [J]	2000	2800
Clamping and joining pressure [MPa]	0.1	0.1
Amplitude [J]	42	42
Joining cycle [s]	1.15 ± 0.1	1.75 ± 0.1

4.2.2. Monitoring of temperature evolution

The temperature evolution during the joining processes was recorded using a high-speed infrared thermo-camera (model ImageIR® 8300 hp, Infratech, Germany) set in the range of 150 – 700 °C with a data acquisition frequency of 80 Hz. These parameters were used for the three joining process used in this work [74] (Figure 20).

The peak temperature achieved in Friction Riveting was observed on the material expelled from the composite part (flash) during the rivet drilling. It is assumed that the material temperature in contact with the plasticized rivet tip has almost the same average temperature affecting the flash [34]. An example of a snapshot of the peak temperature obtained during the FricRiveting process is shown in Figure 20.

The process temperature evolution monitored for Friction Spot Joining was obtained on the aluminum surface while for Ultrasonic Joining it was recorded at the interface between the polymer and the pin tip. The set up for the thermography measurement is schematically illustrated in Figure 21-A and B for FSpJ and U-Joining processes, respectively. The camera positioning and focused area were maintained fixed during all measurements.

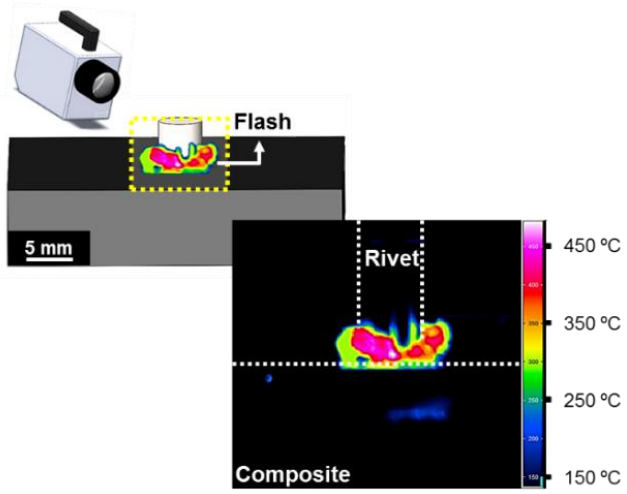

Figure 20 - Set up for the measurement of temperature evolution during FricRiveting process using an infrared camera along with an example of a snapshot showing the maximum process temperature achieved on the composite flash, outward the joining area.

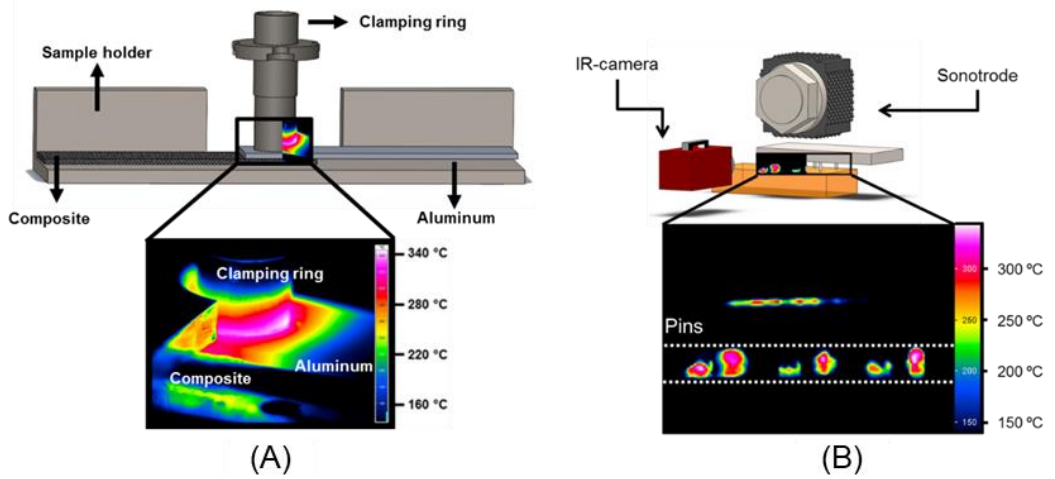

Figure 21 - Set up for the measurement of temperature evolution during FSpJ and U-Joining process using an infrared camera. (A) An example of a snapshot showing the maximum process temperature achieved on the surface of the aluminum during the manufacturing of an FSp joint (Adapted form [52]). (B) Example of the highest temperature measured at the interface between polymer and pin´s tip in a U-Joining joint (Adapted from [40]).

4.2.3. Microstructural analysis

Microstructural analyses were performed on joint mid-cross sections of the joining case-study using reflected light optical (OM) (DM, IRmicroscope, Leica, Germany) and scanning electron microscopy (SEM) (Quanta FEG 650 microscope, FEI, USA). The joints were cutted using an automatic cut-off machine (Secotom-50, Struers, Germany) equipped with a Si-C cutting wheel. The samples were embedded in a low curing temperature epoxy resin followed by standard grinding and polishing materialographic procedures.

For U-Joining samples, etching using Kroll reagent (96 mL H_2O, 6 mL HNO_3 and 2 mL HF) was adopted on joint mid-cross section to reveal the microstructure of the MIM-structured Ti-6Al-4V-0.5B part after the joining process. Friction-riveted and U-Joining samples underwent a gold sputtering step (Q150R ES equipment, Quorum Technologies, England) to increase their conductivity before the SEM, avoiding electric charging on the specimen surface. The SEM was carried out at 10 kV, with 2.5-4.0 spot size.

SEM was used to understand the fracture behavior of U-Joining samples. Additionally, confocal laser scanning microscopy (Keyence VK9700, Japan) was applied to investigate the geometric features of the metallic part in friction spot joints after lap shear testing.

4.2.4. Local mechanical performance

Process-related changes on the local mechanical properties of friction-riveted joints and the metallic base materials (*i.e.* Ti-6Al-4V) were evaluated through Vickers microhardness mapping. The measurements were performed based on the ASTM E384-10 standard, using a Zwick/Roell-ZHV microhardness equipment. Assuming symmetry of the case-study joints, microhardness maps were acquired on half of the specimens, on the longitudinal direction from the base material processing direction, with indentation load of 4.9 N, holding time of 15 s and distance between the indentations of 0.3 mm. Figure 22 schematically illustrates the analyzed region.

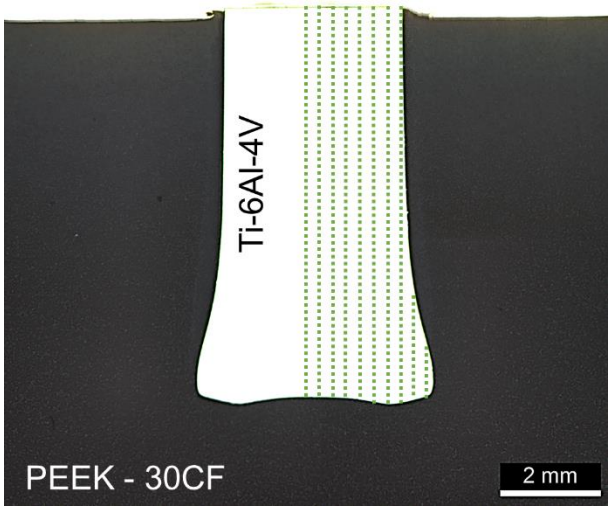

Figure 22 - Schematic representation of the indentation used to obtain the hardness maps for Ti-6Al-4V.

4.2.5. Global mechanical performance

4.2.5.1. Lap-shear testing

Global mechanical performance of ultrasonic and friction spot joints was assessed by lap shear testing. Three replicates of each joining condition were tested following the ASTM D3163-01 standard. The test was carried out at HZG facilities using a universal testing machine (Zwick/Roell, 1478) with a load cell capacity of 100 kN, crosshead speed of 2 $mm.min^{-1}$ (ultrasonic joining) and 1.27 $mm\ min^{-1}$ (friction spot joining), at room temperature.

4.2.5.2. T-Pull testing

The mechanical strength of friction-riveted joints was assessed through T-Pull tensile testing and two replicates of each joining condition were tested. The test was carried out using a universal testing machine (Zwick/Roell, 1478) with a load cell capacity of 100 kN at HZG facilities, crosshead speed of 1 $mm.min^{-1}$, at room temperature.

4.2.6. Non-destructive evaluation and image analysis

4.2.6.1. X-Ray micro-computed tomography

Non-destructively testing using X-Ray micro-computed tomography was performed at the Department of Chemical and Materials Engineering of PUC-Rio facilities to evaluate internal features of the joints produced with FSpJ, FricRiveting and U-Joining. The Zeiss-XRadia Versa 510 equipment (Figure 23) was used and the selected process parameters of X-Ray micro-computed tomography for each joining technologies are summarized in Table 11.

Figure 23 - Zeiss-XRadia Versa 510 [75].

Table 11 - X-Ray micro-computed tomography parameters.

	FSpJ	**FricRiveting**	**U-joining**
Optical magnification	0.4x	0.4x	0.4x
Number of projections	3201	1601	1601
Voltage [KV]	100	160	160
Exposure time [s]	2.2	36	10
Resolution [µm]	14	5.5	10
Binning	2	1	1

The specifications of the equipment can be found in Appendix-A. Scout and Scan Control System is the software used to set the parameters (*i.e.* voltage, lens, current, adjustment of the sample position, camera, pixel size, exposure time, rotation step) and to acquire projection images. The parameters were selected for specimens of each joining process based on the compromise between the visibility and resolution along with the transmittance of each material combination (*e.g.* according to the density of the objects analyzed) when exposed to the X-Ray beam.

4.2.6.1.1.
Limitations and Optimization of Tomography Conditions

Although the X-ray beam is attenuated by the physical characteristics (atomic number, density, and thickness) of the material, some difficulties to discriminate internal flaws was observed during the digital image processing and analysis due to the large difference in X-Ray absorption and scattering between the metal and polymer used as joining parts. First of all, the titanium used in FricRiveting and U-Joining as the metallic part, appeared much brighter than the polymer/composite parts, making it hard to discriminate dark defects at the metal-polymer interface. Strong scattering artifacts due to the titanium parts also hindered the detection of the defects. This problem was minimized by increasing the X-Ray energy to its maximum value (160 kV) and using a higher energy filter which contributed to the reduction of scattering, leading to a better discrimination of defects.

Furthermore, the second limitation observed was caused by the so-called cone effect of the X-Ray beam that reduces the projection image intensity at the cone edges. As the internal flaws showed very low contrast, any intensity variation would render them undetectable. This was solved with a mosaic setup, in which the sample was scanned with a combination of vertical volumes, such that the relevant part of the sample was far away from the mosaic edges. Even though this setup wastes a fair amount of the scanned volume, it eliminates the cone edge effect.

4.2.6.2.
Digital image processing and analysis

Digital image processing was carried out by Dragonfly and FIJI software for each friction-based joining technique. The joints were segmented, colored and the internal features were quantitatively and qualitatively evaluated. The volumes of interest for each joining technology are presented in the following sub-sections to better understand the image analyses carried out in this work.

4.2.6.2.1.
Friction spot joining

Dragonfly software was used to perform the measurements and volumes deconvolution. The volumes of interest for friction spot joints were the metallic nub inserted into the composite part and internal micro-voids at the metal-composite interface. The same volume of material was selected for a quantitative evaluation of micro-voids. Figure 24-A exemplifies by the red area the 3D volume measurement of the nub, while Figure 24-B depicts the segmentation into three parts (composite, micro-voids and aluminum) used to quantitatively and qualitatively evaluate the internal flaws.

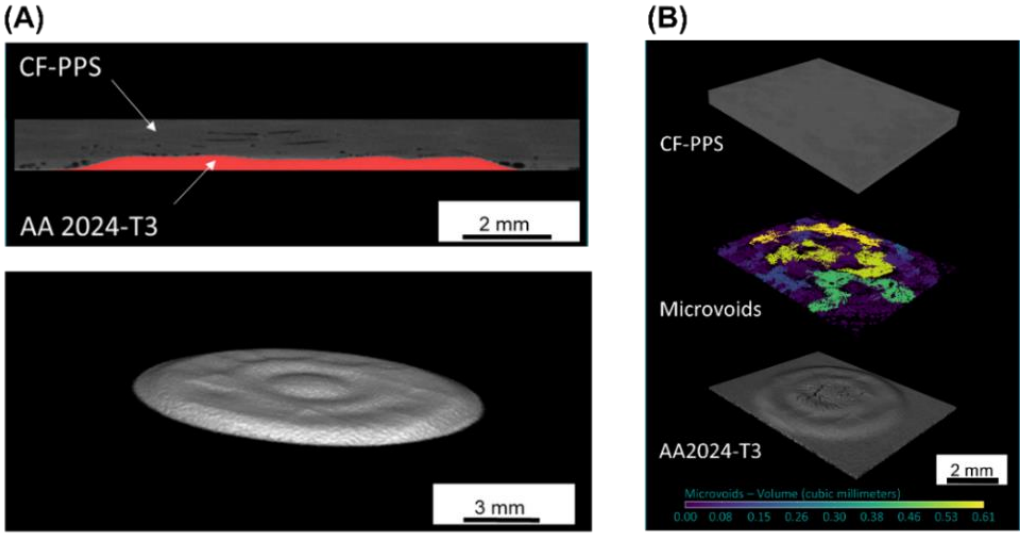

Figure 24 - (A) Segmented volume of the metallic nub in 2D and 3D views and (B) segmented and colored micro voids subdivided in a scale of color based on volume.

4.2.6.2.2.
Friction riveting

Dragonfly software was used to perform the volumes deconvolution and measurements of the rivet inserted into the composite plate (yellow volume), as shown in Figure 25-A and Figure 25 -B. Figure 25-C highlights the accomplished geometry measurements of the rivet, including the total volume of the rivet into the composite, rivet penetration depth (H), rivet tip width (W) and depth in which the rivet diameter starts to widen into the composite plate (D). FIJI and Dragonfly software were used to assess and measure the volume of polymer above the

deformed rivet tip, respectively. The cylinder shape was used to extract the volume of polymer above the deformed rivet tip, as presented in Figure 25-B.

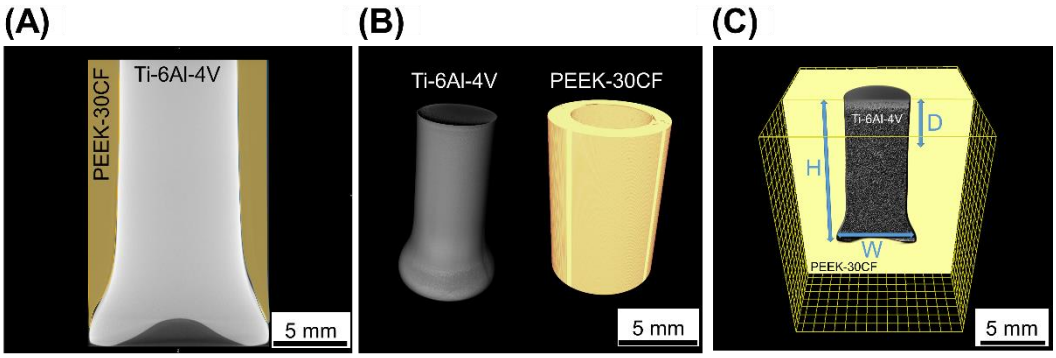

Figure 25 - (A) 2D and (B) 3D views of the volume of plasticized pin inserted into the composite plate and the volume of polymer above the deformed rivet (yellow volume). (C) Example of a Ti-6Al-4V/PEEK-30CF friction-riveted joint, showing the Rivet penetration depth (H) the maximum rivet tip width (W) and the depth in which the rivet diameter starts to widen into the composite plate (D).

Additionally, micro-cracks and micro-voids were qualitatively evaluated, as exemplified in Figure 26-A and B.

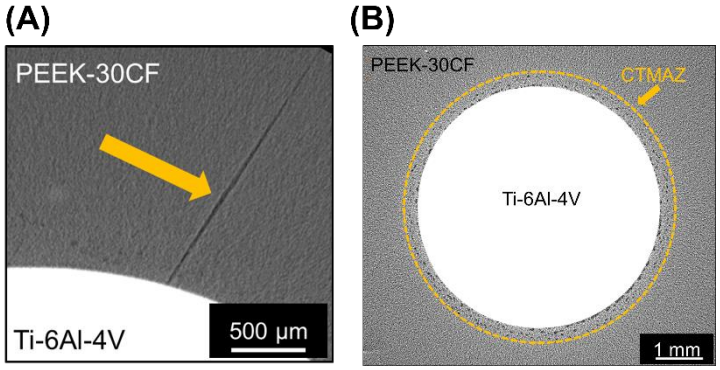

Figure 26 - (A) Top-view of an example of micro-cracks and (B) micro-voids in a specific layer in the composite plate around the rivet.

4.2.6.2.3.
Ultrasonic Joining

3D images obtained by micro CT were used to evaluate the insertion of the six conical pins into the polymeric plate (Figure 27 - A). In addition, the MIM-

structured metallic part was evaluated to confirm that no pin damage or deflection by plastic deformation was induced during the pin plunging. Moreover, the total volume of softened polymer inserted into the geometrical undercut was measured (Figure 27-B). Finally, a detailed analysis was carried out to visualize microvoids at the metal-polymer interface of the joints. Figure 27-C shows the microvoids concentrated in the surroundings of the pins (indicated by orange arrow).

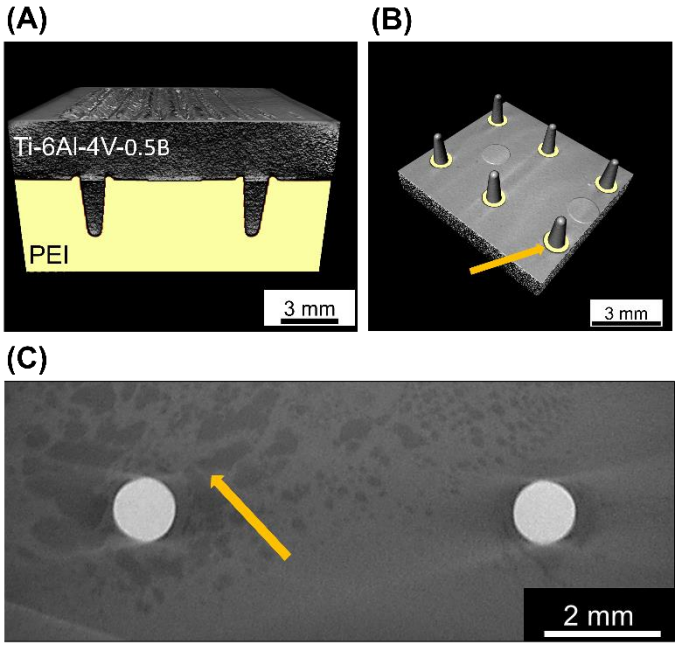

Figure 27 - (A) 3D view obtained by micro CT, showing the conical pins totally inserted into the polymeric plate and the (B) geometrical undercut filled by the softened polymer (orange arrow). (C) Top-view of the joint showing the micro-voids around the pins at the pin-polymer interface (orange arrow).

5
Results and Discussion

5.1.
Friction Spot Joining

5.1.1.
Temperature evolution

The process temperature evolution observed on the surface of aluminum for the overlap joints produced under low (LHI) and high heat input (HHI) joining conditions are demonstrated in Figure 28.

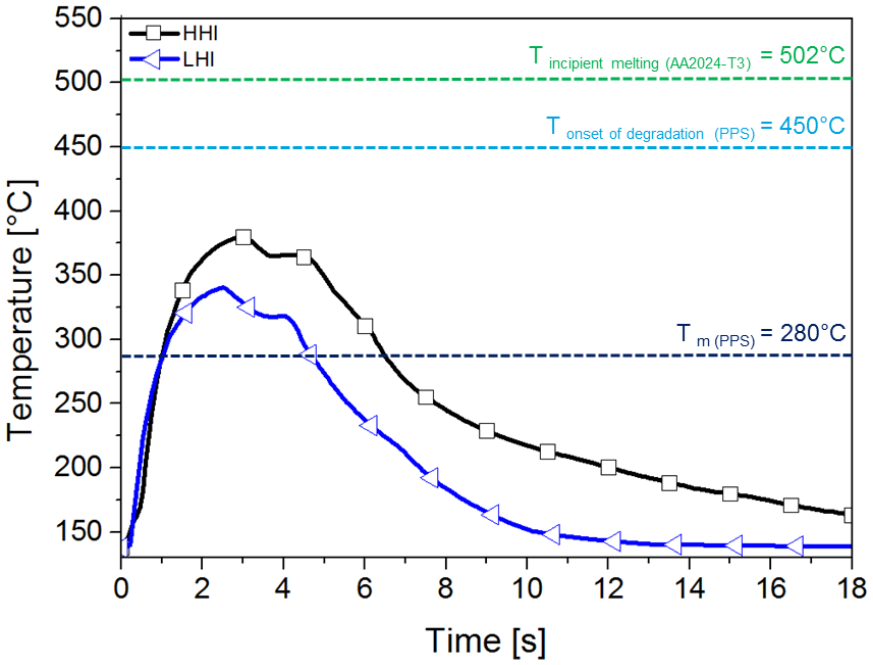

Figure 28 - Process temperature evolution on the surface of aluminum for joining conditions involving low and a high heat input. The temperatures of the onset of thermal degradation and melting point of PPS matrix as well as the incipient melting of the AA2024-T3 are schematically shown in the figure.

The average peak temperature observed on the aluminum surface for the HHI joining condition was 385 ± 5 ºC, while 332 ± 9 ºC was observed for the LHI joining

condition. The maximum process temperature achieved on the aluminum surface for HHI and LHI, represent, respectively, 76 % and 68% of the incipient melting point of AA2024-T3. Moreover, the observed peak temperatures are above the melting point of the PPS matrix and the PPS film interlayer (280 ºC). Therefore, a thin layer of the PPS composite matrix and the PPS film interlayer were melted during the joining process in a volume around the tool.

Furthermore, extensive thermal degradation of the PPS matrix and the PPS film is not expected to occur during the joining process for both HHI and LHI conditions, due to the fact that the peak temperatures (maximum 340 ºC for LHI and maximum 380 ºC for HHI) observed are below the onset temperature for PPS degradation (450 ºC).

5.1.2. Joints formation

5.1.2.1. Metallic nub formation

During the joining process, the metal is plasticized and plastically deformed by the tool plunging movement into the composite part, creating an undercut: the metallic nub. The macro-mechanical interlocking between the parts is provided by the metallic nub, as previously discussed in Section 3.1.1. Figure 29 presents a detailed view of the metallic nub obtained by micro CT for the LHI and HHI joints.

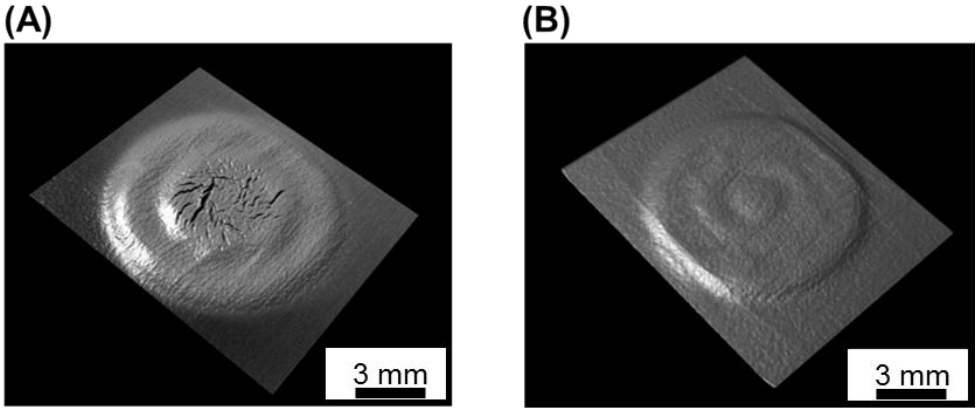

Figure 29 - 3D image of the metallic nub obtained by micro CT (A) for HHI and (B) LHI joints.

The volume of metal inserted into the composite part was measured for HHI and LHI joints. Figure 30 shows the measured volume of metal in 2D and 3D views. The combination of high frictional heat and joining force during the joining process for the HHI joints (Table 8) led to a slightly higher volume of metal inserted into the composite part (21.90 mm^3) in comparison to the LHI joints (19.75 mm^3). Although, the volume of inserted metal was very similar for both HHI and LHI conditions, different geometries for the metallic nubs were observed, as discussed next.

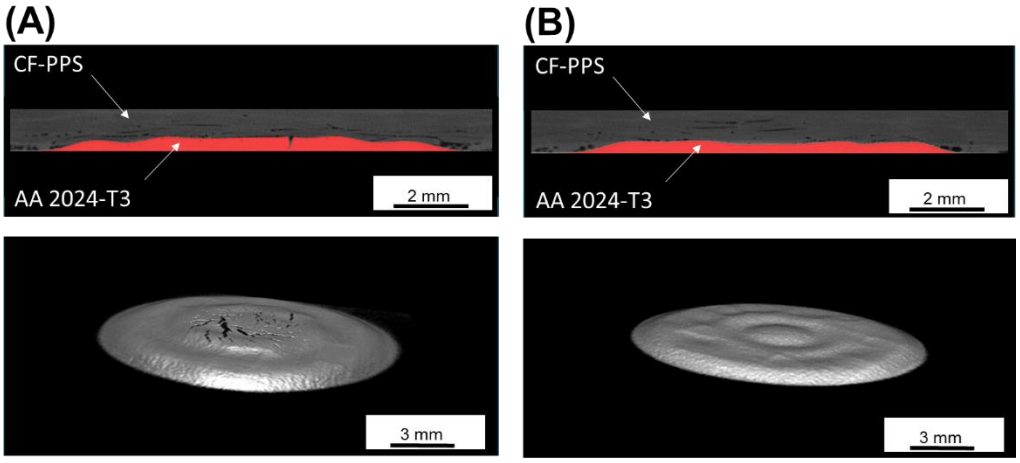

Figure 30 - Schematics of the measurement of the volume of the metallic nub for (A) HHI and (B) LHI joints in 2D and 3D views.

Figure 31 consists of the 3D images obtained by confocal laser microscopy of the fracture surface of the joints (on the aluminum part) showing the topography of the metallic nub for joints produced with high (HHI) and low heat input (LHI). Different geometries for the metallic nubs were observed. On one hand, the HHI joints showed a metallic nub deformed in a shape of two rings (Figure 31-A), as a result of the high frictional heat (2900 rpm; peak temperature of 380°C) and joining force (5 kN) applied during the process. On the other hand, a flat metallic nub was observed for LHI joints (Figure 31-B). The lower temperature (340°C) achieved during the process for the LHI joints due to the lower rotational speed (1900 rpm) and joining force (3 kN) applied, led to a flat deformation of the metal in this case.

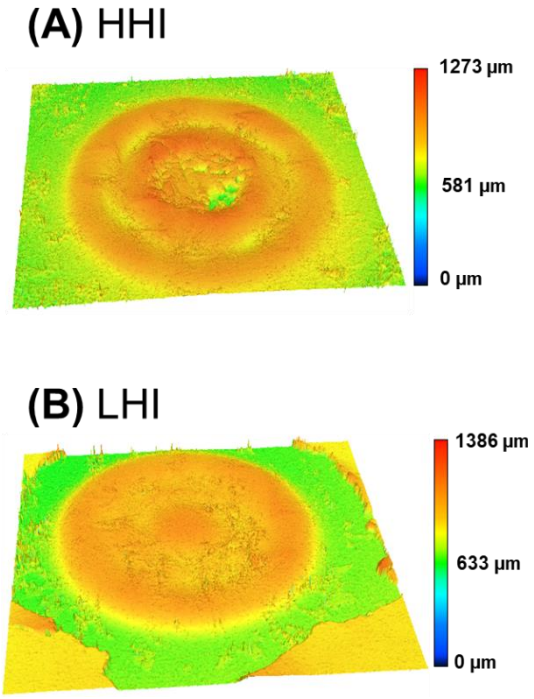

Figure 31 - 3D images of the aluminum surface after the fracture of the joint obtained by confocal scanning laser microscopy. (A) Metallic nub shaped in two rings for HHI joints. (B) Flat metallic nub for LHI joints.

Furthermore, some micro-cracks were observed in the metallic nub in HHI joints, as shown in Figure 32-A. It is believed that the micro-cracks are a result of the high joining force applied to the thin layer of plasticized metal below the tool during the plunging of the sleeve. Micro-cracks were not identified for the LHI joint (Figure 32 - B), probably due to the lower joining force used during the joining process.

Figure 32-B to E consists of a sequence of images showing the distribution of the micro-cracks into the volume of the metallic nub. The level of the different layers analyzed are indicated by arrows (B to E) in Figure 32 - A. It is important to note that the micro-cracks are observed just into the volume of the metal inserted into the composite part. The first micro-crack was identified in layer B (at the level of the interface between non-deformed aluminum and composite) (Figure 32-B). The size and distribution of the micro-cracks can be observed as the scanning advances into the plastically deformed volume of metal (metallic nub) in Figure 32-C to E.

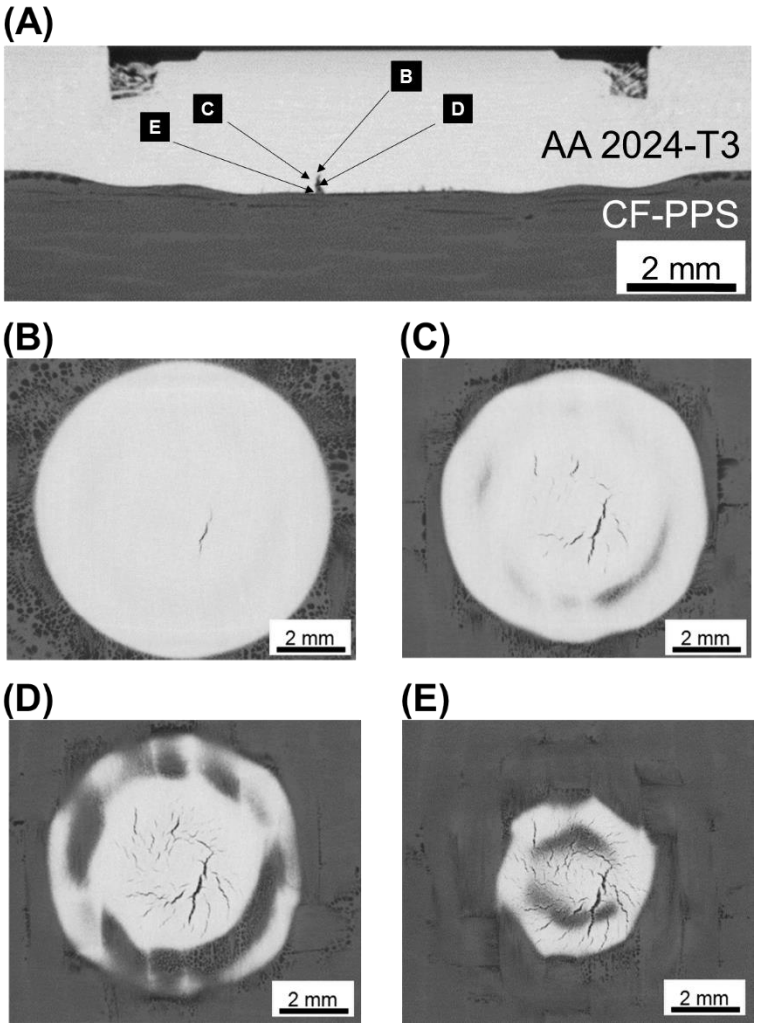

Figure 32 - (A) Cross section of a representative HHI joint. The size and distribution of the micro-cracks can be observed as the scanning advances into the metallic nub from (B) to (E).

5.1.3. Analysis of joints interface

This section presents the analysis of the joints interface produced under high and low heat input joining conditions. Different features were observed at the joint interface through a detailed optical and laser microscopy analysis of the cross-section of the joints. The micro-mechanical interlocking is an important bonding mechanism of FSp joints, as discussed in Section 3.1.1. Such mechanical interlocking between the parts is microscopically provided by the entrapment of PPS matrix/film and fibers into the irregularities of the metal. Crevices and irregularities were created on the surface of the aluminum and composite parts through sandblasting performed prior to the joining process. This surface pre-

treatment was used to improve the adhesion between the joining parts and the PPS film interlayer, as discussed in detail by André [29]. The sandblasting parameters used in this work are reported in Section 4.2.1.1. An average surface roughness of 6.33 ± 0.44 µm was achieved for the aluminum part, while 5.34 ± 0.62 µm was achieved for the composite part.

Figure 33-A presents the cross section of a representative HHI joint. The regions of the interface analyzed in detail are marked as B and C. As discussed earlier (Section 5.1.1), the PPS matrix is molten and its viscosity is reduced during the process due to the peak temperature achieved (380°C). Figure 33-B shows that carbon fibers are entrapped by the plasticized aluminum. Simultaneously, the crevices and micro-cracks (Section 5.1.2.1, Figure 30) on the rough aluminum surface are filled with molten PPS (Figure 33-C). Both features are responsible for the micro-mechanical interlocking at the joint interface. A few micro-voids are also observed on the composite part in the center of the joint (Figure 33-C). The micro-voids will be discussed in detail in Section 5.1.3.1.

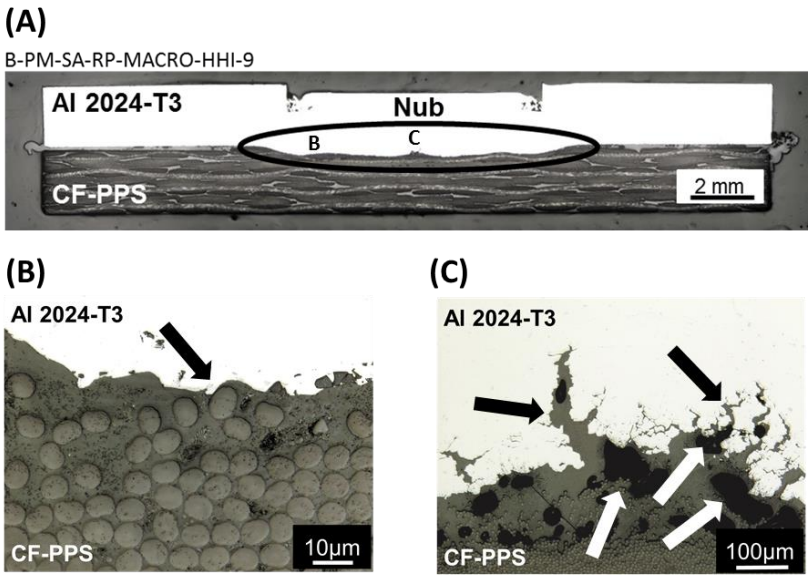

Figure 33 - Microstructural details of the joint interface produced under high heat input: (A) cross-sectional view of a representative FSp joint with interlayer produced with HHI, (B) carbon fibers embedded by the aluminum (black arrow), (C) entrapped molten polymer into the crevices of sandblasted aluminum surface (black arrows) and micro-voids into the polymeric matrix (white arrows).

The same features were identified for the LHI joint. The cross section of a representative joint produced with LHI is shown in Figure 34-A. Fiber and polymer matrix entrapment on the aluminum surface were observed in Figure 34-B and C, respectively. The micro-voids discussed previously for the HHI joint were also identified for the LHI joints (Figure 34-D) and will also be discussed in detail in Section 5.1.3.1.

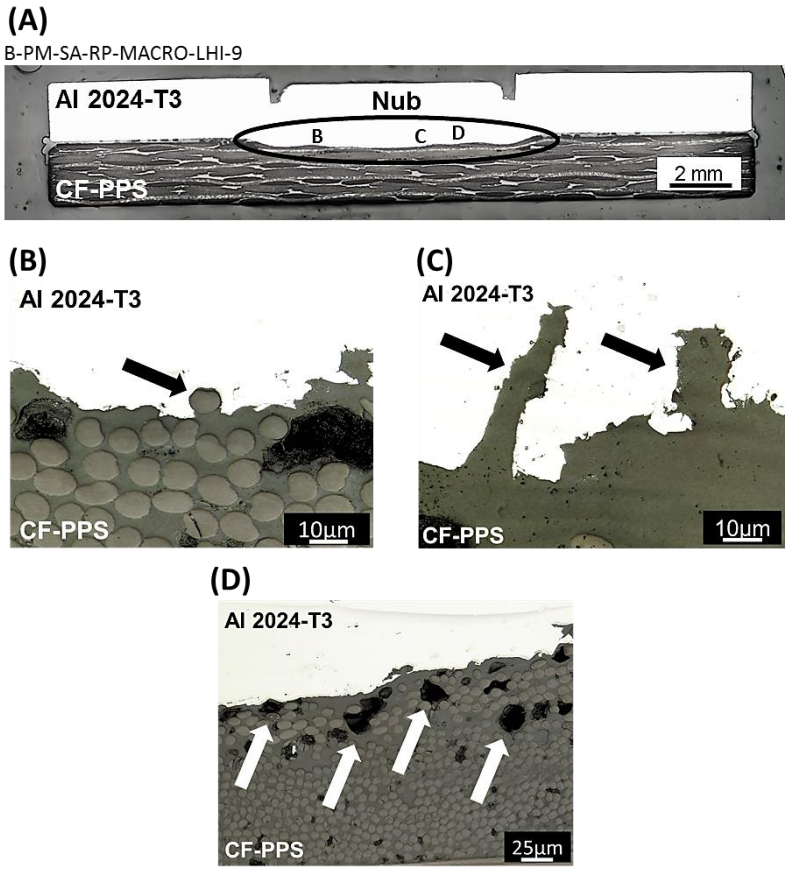

Figure 34 - Microstructural details of the joint interface produced under low heat input: (A) cross-sectional view of a representative FSp joint with interlayer produced with LHI, (B) carbon fibers embedded by the aluminum (black arrow), (B) entrapped molten polymer into o the crevices of sandblasted aluminum surface (black arrows) and (D) micro-voids into the polymeric matrix (white arrows).

5.1.3.1.
Internal Flaws

As discussed previously in Section 5.1.3, micro-voids were observed in the composite part close to the interface with the metal for HHI (Figure 33) and LHI

(Figure 34) joints. Tan [76] reported that flaws are formed either by small thermal degradation or by shrinkage of the heat-affected polymer. However, in this work it is believed that such micro-voids are not related to thermal degradation, since the peak process temperatures (380º C for LHI and 340º C for HHI) were not high enough – the onset of degradation of PPS is 450°C [55]. According to Goushegir *et al.* [26], air might be entrapped into the molten PPS during the joining process due to its outward flow induced by the axial movement of the tool. As a result, micro-voids are formed after the joint consolidation.

The distribution and quantification of the micro-voids for both joining conditions were evaluated with microCT. A representative distribution of the micro-voids were observed in different layers of the composite, as shown in Figure 35-A and Figure 36-A, for HHI and LHI joints respectively.

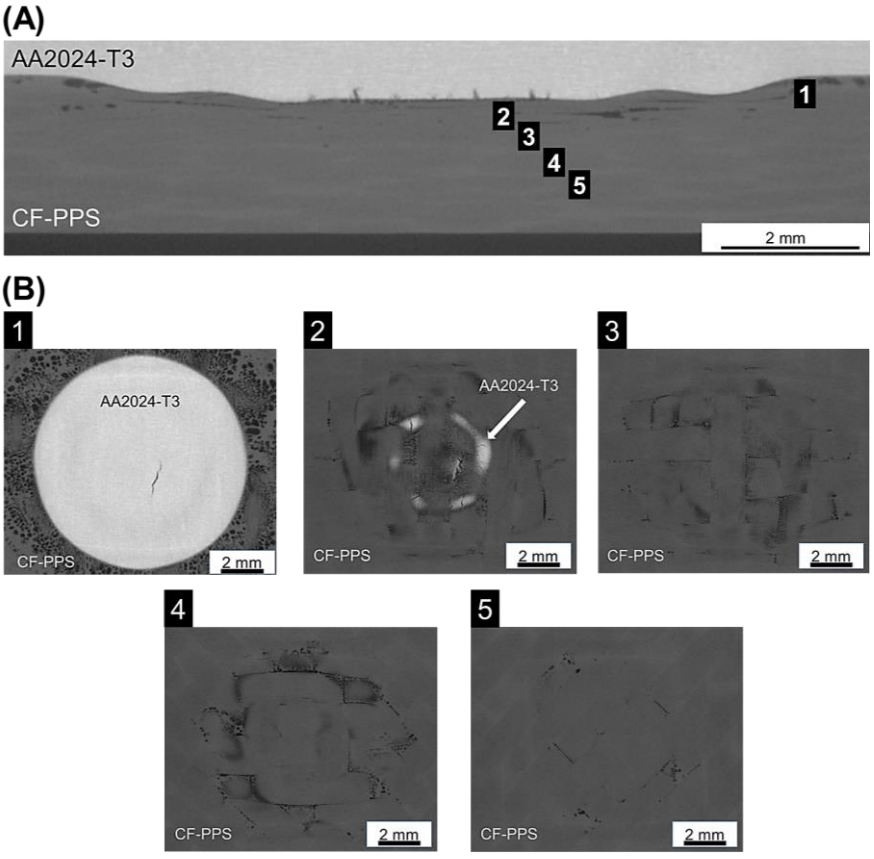

Figure 35 - (A) Cross-sectional view of HHI friction spot joint obtained by X-ray micro-computed tomography. (B) Magnified view of micro-voids in different layers of the composite under the nub region.

The maximum depth (starting from the top surface of the non-deformed composite) where micro-voids could be identified into the composite part was 1.04 mm for HHI and 0.93 mm for LHI joints.

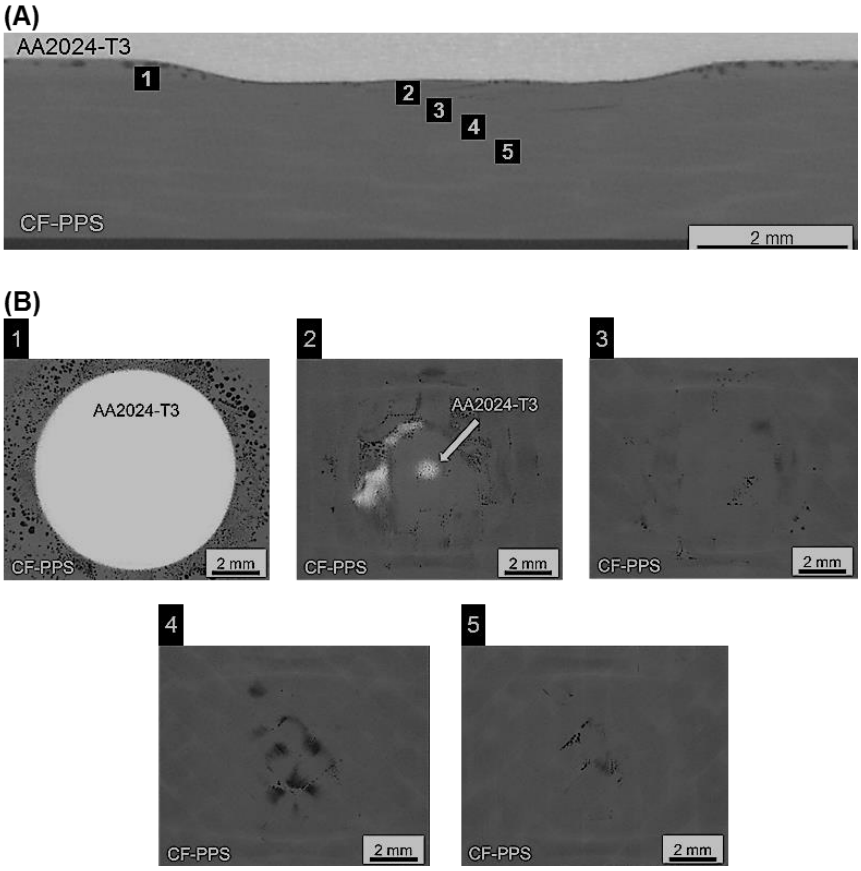

Figure 36 - (A) Cross-sectional view of LHI friction spot joint obtained by X-ray micro-computed tomography. (B) Magnified view of micro-voids in different layers of the composite under the nub region.

The overlap joint was separated in three parts (composite, micro voids and aluminum) by using Dragonfly software, as shown in Figure 37. The volume of micro-voids at the metal-composite interface was segmented and colored for a better visualization. The total volume of micro-voids into the HHI joint was 4.32 mm^3, whereas 1.63 mm^3 of micro voids were identified for the LHI joint. The LHI condition led to a lower peak process temperature (332 ± 9 ºC) compared to the HHI condition (385 ± 5 ºC), as discussed in Section 5.1.1. Therefore, the volume of PPS matrix affected by the frictional heat is lower compared to the HHI condition.

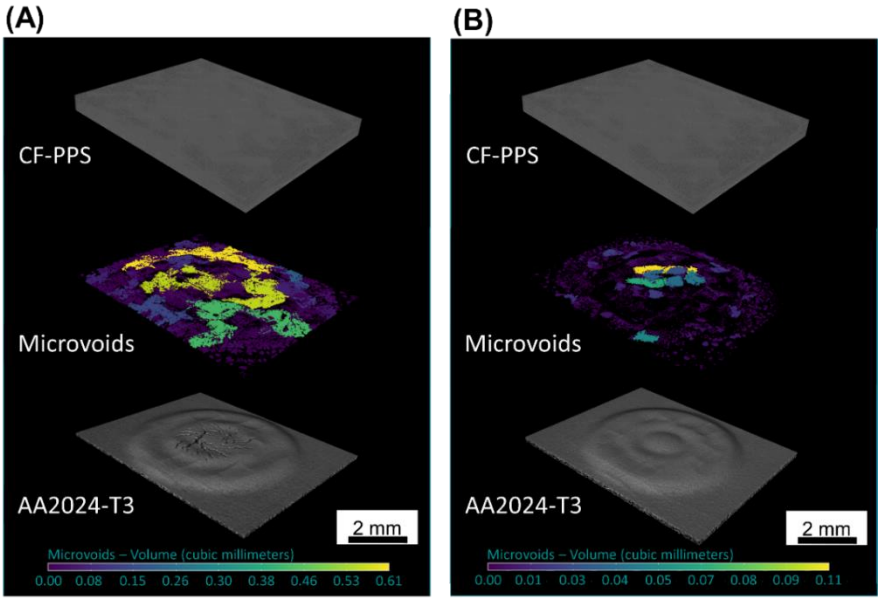

Figure 37 - Example of X-ray micro-computed tomography for micro-voids quantification of (A) HHI and (B) LHI joints, showing segmented and colored volumes.

The segmented and colored micro-voids were subdivided in a scale of color based on volume differentiation. When analyzing Figure 38, it is possible to note that bigger micro voids tend to be concentrated below the metallic nub due to the higher temperature achieved in the center of the joints. Additionally, smaller micro-voids tend to be distributed in the PPS matrix around the metallic nub, where lower temperatures are achieved.

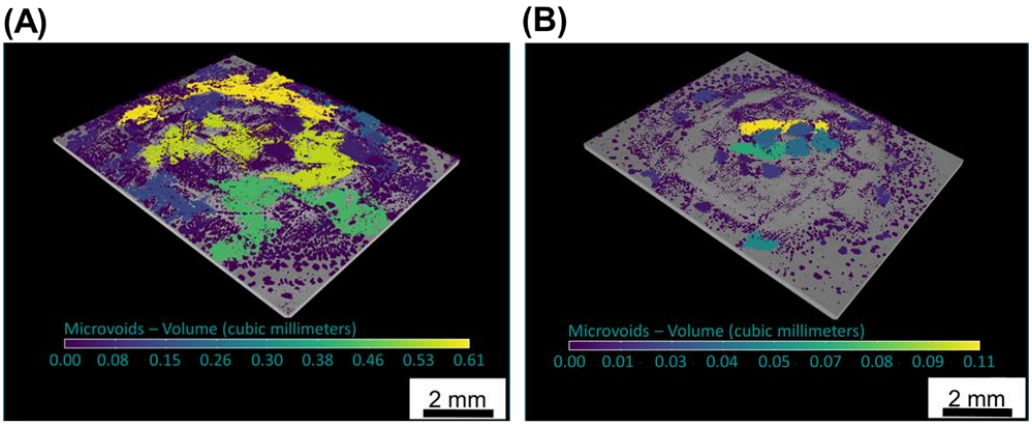

Figure 38 - 3D view of micro-voids distribution for (A) HHI and (B) LHI joints.

5.1.4.
Global mechanical performance and failure mechanisms

The quasi-static mechanical performance of the joints was evaluated through lap shear testing following the procedure described in Section 4.2.5.1. The influence of the frictional heat generated during the joining process on the mechanical performance of the joints was addressed in this section. Three replicates of joints produced under high and low heat input conditions were selected to analyze the mechanical performance of the joints, as shown in Figure 39. The HHI joints presented an ultimate lap shear force (ULSF) 43 % higher (2738 ± 162 N) than the LHI joints (1915 ± 225 N).

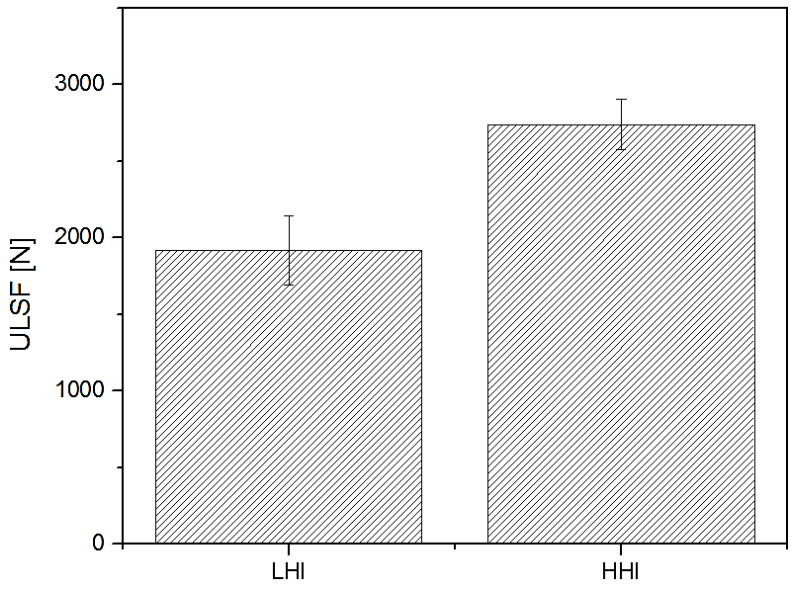

Figure 39 - Ultimate lap shear force of FSp joints produced under high and low heat input conditions.

As described in previous investigations [26], the plastically deformed zone (PDZ) is the strongest bonding zone in friction spot joints. It comprises the central region of the spot joint where the metal is deformed into the composite, creating the metallic nub. In this zone, the PPS matrix and film are dislocated from the center to the edges of the joint, exposing some fibers. Therefore, an effective micro-mechanical interlocking between composite and aluminum is expected in this region due to polymer and fiber entrapment into the aluminum irregularities. Figure 40-A and B highlights the PDZ in the center of the overlap area of the joints

produced with HHI and LHI conditions (yellow dash circles). As a result of the higher frictional heat generated during the joining process, the HHI joints present 60% larger plastically deformed zones (249 ± 28 mm^2) compared to the LHI joints (155 ± 11 mm^2).

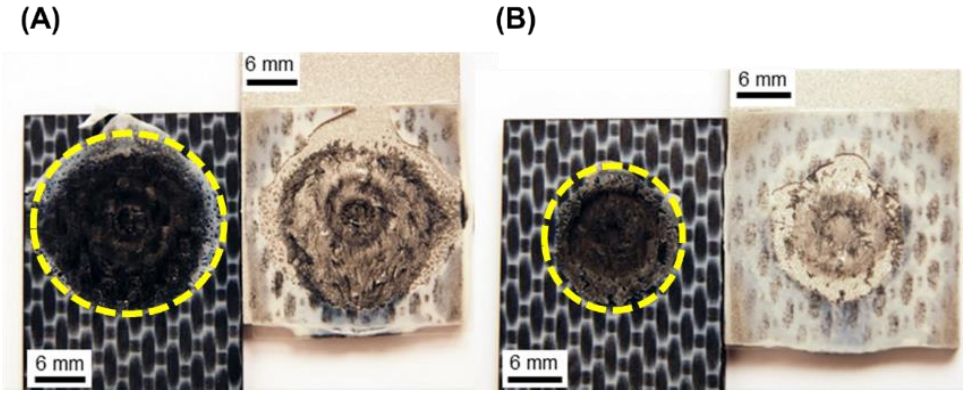

Figure 40 - Representative examples of fracture surfaces of FSp joints produced with (A) HHI and (B) LHI joining conditions.

Additionally, the HHI and LHI joints presented different geometries of the nub (Section 5.1.2.1). The HHI joints showed a metallic nub deformed in a shape of two rings (Figure 31-A), while a flat metallic nub was observed for LHI joints (Figure 31-B). The high frictional heat (2900 rpm; peak temperature of 380°C) and joining force (5 KN) applied during the HHI joining process led to a better pinning effect compared to the LHI condition (1900 rpm; peak temperature of 340°C and joining force of 3 KN). This suggests that the nub deformed in a shape of two rings in a spot area creates two points of macro-mechanical interlocking. Moreover, superior lap shear strength of the HHI joints (43%) can be related to the different geometry of the metallic nub.

As discussed in Section 5.1.2.1, micro-cracks were observed in the metallic nub of the joint produced with HHI, as a result of the high frictional heat (380°C) and joining force (5 KN) applied during the manufacturing of the HHI joints (Figure 32). It is worth mentioning that such features were not identified for the LHI joint. It is believed that the molten PPS flowed into such micro-cracks during the joining process. The entrapped polymer into the micro-cracks in the aluminum provides additional micro-mechanical interlocking at the interface of the HHI joints, leading to the higher mechanical strength of these joints.

5.2.
Friction Riveting

5.2.1.
Temperature evolution

The process temperature evolution in friction-riveted joints produced under high and low energy input conditions was measured by high-speed infrared thermo-camera, as shown in Figure 41. The peak temperature achieved for each joining conditions was observed on the flash material expelled from the joining area during the rivet insertion, as discussed earlier in Section 4.2.2.

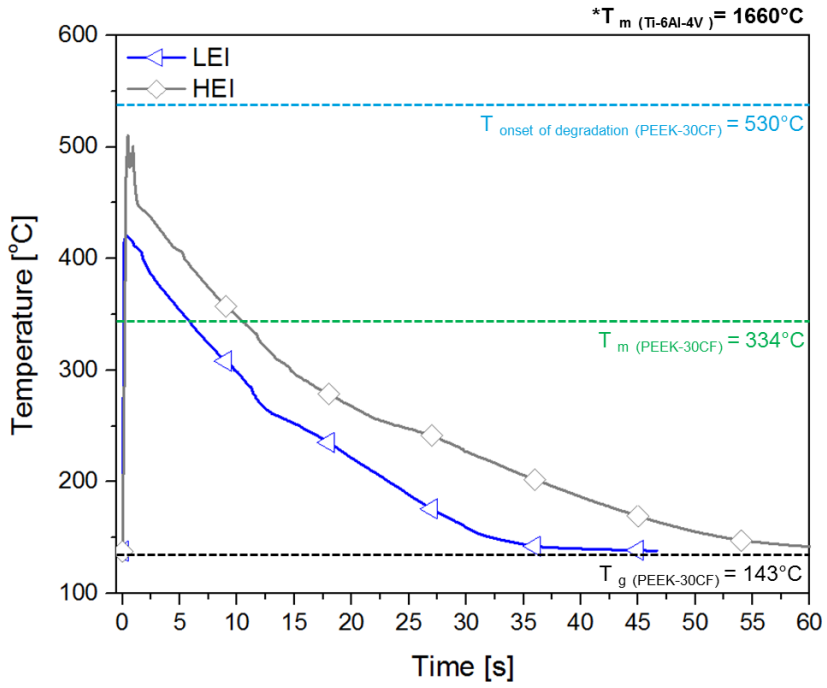

Figure 41 - Process temperature evolution on the flash material expelled for joints produced with low and a high heat input. The temperatures of the onset of thermal degradation, glass transition and melting point of PEEK-30CF matrix as well as the melting temperature of the Ti-6Al-4V are schematically shown in the figure.

The peak temperature observed on the flash material expelled from the joining area for HEI condition was 510 ºC, while 421 ºC was observed for the LEI condition, which are below the degradation temperature of PEEK-30C (530 ºC) [62, 63]. Therefore, no extensive thermomechanical degradation is expected in the composite matrix volume in the surroundings of the rivet. Additionally, the melting

temperature (334 ºC) of PEEK-30C was reached, decreasing the polymer viscosity and promoting the material flow. The recorded temperature on the flash expelled by LHI and HHI were peaking at 25-30 % of the Ti-6Al-4V melting temperature (1660 ºC). Although no melting is taking place, the temperature is enough to plasticize the metal. Considering the peak temperatures below the β-transus temperature of the Ti-6Al-4V (995ºC) [77], no microstructural changes are expected through the rivet length during the joining process for both HEI and LEI joining conditions.

5.2.2. Joints Formation

During the joining process, the metal is plasticized and plastically deformed into the composite part, creating an anchoring zone. Figure 42-A and B presents a detailed view of the metallic rivet and the composite volume above the deformed rivet tip obtained by microCT for the LEI and HEI joints.

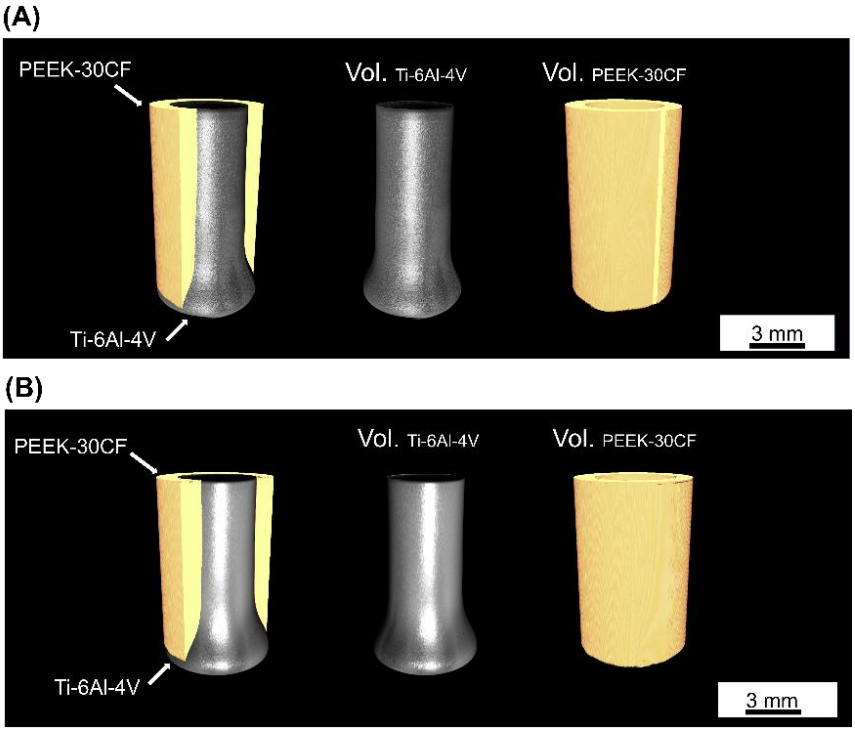

Figure 42 - Microstructural appearance of a Ti-6Al-4V/PEEK-30CF friction riveted joint produced under (A) high and (B) low energy input conditions. Isolated volume of Ti-6Al-4V inserted into the composite part and the volume of polymer above the deformed rivet.

The geometric measurements of the anchoring zone including the average rivet penetration depth (H), width of the rivet tip (W), depth of initial rivet plastic deformation (D) and volumes of Ti-6Al-4V ($Vol_{Ti\text{-}6Al\text{-}4V}$) and of PEEK-30CF ($Vol_{PEEK\text{-}30CF}$) above the deformed rivet for LEI and HEI joints are summarized in Table 12. It is important to notice that no replicates were evaluated for the measurements carried out using the microCT, hence, no deviations were calculated. Therefore, further experiments are needed to statistically evaluate and confirm the results obtained so far.

Table 12 - Geometric measurements of the anchoring zone of joints produced under high and low heat input.

	Low energy input	**High energy input**
H [mm] []	12.05 ± 46	12.49 ± 88
W [mm]	7.38 ± 0.40	8.17 ± 0.69
D [mm]	4.51	3.61
$VOL_{TI\text{-}6AL\text{-}4V}$ [mm^3]	294	320
$VOL_{PEEK\text{-}30CF}$ [mm^3]	239	247

By increasing the rotational speed and consequently the energy input, 4% increase of rivet penetration depth was observed (from 12.05 ± 0.46 mm to 12.49 ± 0.88 mm). HEI joints also achieved higher width of the plastically deformed rivet tip (8.17 ± 0.69 mm) compared to LEI joints (7.38 ± 0.40 mm). Consequently, HEI joints showed a higher volume of the rivet inserted into the composite plate ($Vol_{Ti\text{-}6Al\text{-}4V}$ = 320 mm^3) compared to LEI joints ($Vol_{Ti\text{-}6Al\text{-}4V}$ = 294 mm^3).

As discussed early in Section 3.1.2, high rotational speed combined with pressure applied during the joining process generates frictional heat which rises locally the temperature at the rivet tip. Such temperature overcomes the melting temperature of the polymer (334 ºC) [62, 63] resulting in a thin softened/molten polymeric layer formed around the rivet tip. The axial force applied facilitates the outward flow of the molten polymer, which therefore leads to the rivet insertion into the polymeric plate. The higher the energy, more polymer is affected by higher

temperatures on the rivet tip surface and consequently the higher is the rivet penetration and plastic deformation of the rivet tip.

On the other hand, at higher rotational speed the plastic deformation of the rivet occurs earlier. The rivet diameter starts to widen for HEI joints at depth of 3.61 mm while for LEI joints, the widening starts at 4.51 mm (Table 12). In this case, at higher rotational speed, the joining time is shortened (see monitoring curves in Appendix B) and all the generated heat is quickly delivered, plasticizing the metal and inducing earlier rivet deformation. As a result, no significant change of polymer volume above the deformed rivet tip was identified ($Vol_{PEEK\text{-}30CF}$ = 247 mm^3 for HEI joints and $Vol_{PEEK\text{-}30CF}$ = 239 $mm^3$for LEI joints), as shown in Table 12.

The deconvoluted volumes were used to calculate the volumetric ratio (VR) which represents the polymer interaction volume above the deformed rivet tip, mainly responsible to carry the load during tensile test and to provide the anchoring efficiency of metallic-insert joints [37]. Two methods were adopted: a quotient between $Vol_{PEEK\text{-}30CF}$ and the sum of $Vol_{Ti\text{-}6Al\text{-}4V}$ and $Vol_{PEEK\text{-}30CF}$ (measurements provided by microCT) ($VR_{\mu\text{-}ct}$), and a simplified geometric model proposed by Blaga *et al.* [37] (VR_A).

Table 13 lists the values obtained by the two methods for both energy input values. $VR_{\mu\text{-}ct}$ method was used to validate the VR_A proposed by Blaga *et al.* which is mathematically expressed by Equation 2, where H is the penetration depth of the metallic rivet, W is the maximum width of the deformed rivet tip, D is the original diameter of the rivet and B is the height of the anchoring zone. Figure 43 highlights the main geometric features considered in Equation 1.

Table 13 - Summary of Volumetric Ratio measured by analytical method (VR_A) and quotient provided by the microtomography analysis ($VR_{\mu\text{-}ct}$)

	VR_A	**$VR_{\mu\text{-}CT}$**
Low energy input	0.50 ± 0.05	0.44
High energy input	0.58 ± 0.06	0.44

$$VR = \frac{(\mathrm{H}-\mathrm{B})(W^2-D^2)}{W^2.\mathrm{H}} \quad (2)$$

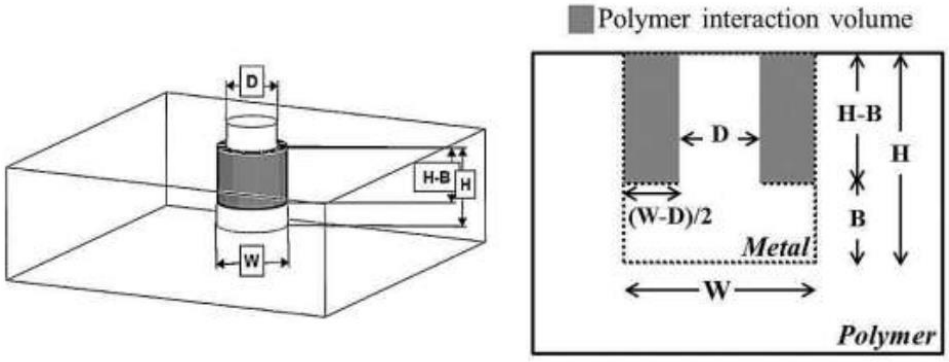

Figure 43 - Simplified geometry used to calculate the polymer interaction volume above the deformed rivet tip (emphasizing the interaction volume in gray) [78].

The methods showed similar volumetric ratio for HEI and LEI joining conditions. The VR_A measured for HEI joints was (0.58 ± 0.06) while for LEI joints was (0.50 ± 0.05). The $VR_{\mu\text{-}ct}$ for both conditions was 0.44. Despite the similar trend, the averages obtained by the analytical model was slightly superior to the measurement method, what can be explained by the absence of replicates for microtomography and simplifications adopted by the analytical method such as symmetry of the deformed rivet and features on the rivet surface. The virtual similarities between the joining conditions may be explained by the reduction of the polymeric volume above the deformed rivet tip for HEI joints which compensates the increase of the metallic rivet inserted into the composite observed for such condition. Therefore, LEI and HEI achieved similar volumetric ratios, which may induce similar mechanical behavior.

Figure 44-A and B are the typical 3D- reconstructed images of HEI and LEI joints and their respective cross sections. As highlighted by yellow dashed circles, a cavity is formed at the rivet tip which decreases with energy input. Such cavity reduces the total volume of the anchoring zone (sum of metal and polymer volume). This rivet feature is not considered in the analytical method, and can contribute to mismatching between the methods.

Figure 45-A and B depicts irregularities on the rivet surface (yellow arrows) which shows an asymmetric deformation of the rivet tip for joints produced under high and low energy input. This rivet asymmetry is also not considered by Equation 1, leading to differences between the VR methods.

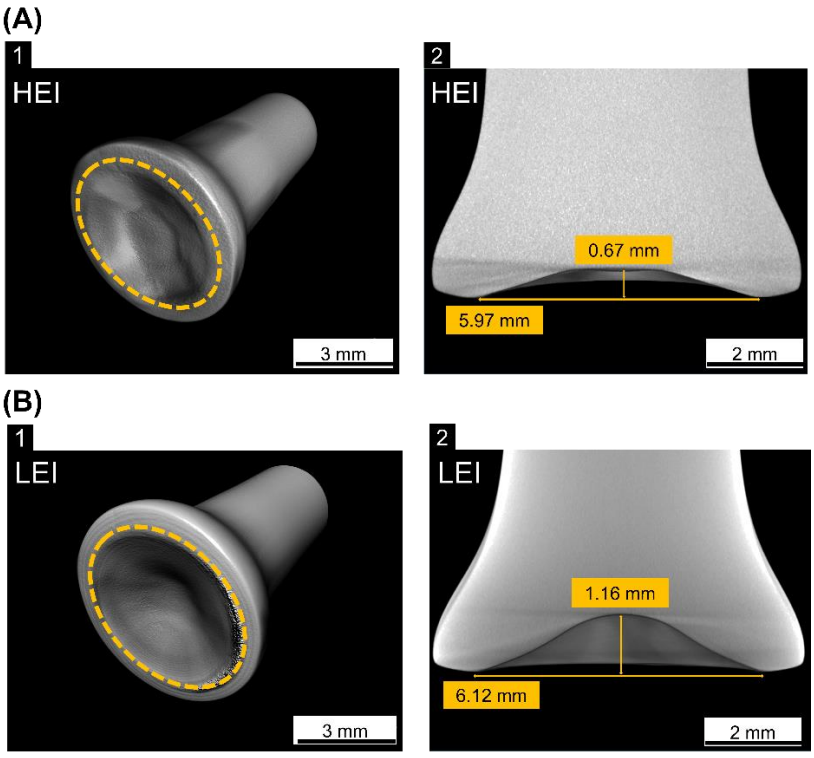

Figure 44 - 3D view obtained by miroCT of a Ti-6Al-4V/PEEK-30CF friction-riveted joint for (A) HEI and (B) LEI joining conditions. Cross section magnified view of the cavity formed during the joining process on the tip of the rivet for HEI (A - 2) and LEI (B - 2) joints, respectively.

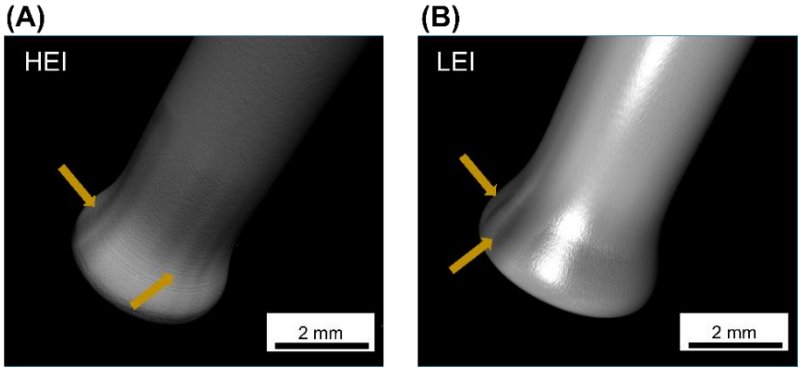

Figure 45 - Irregularities on the rivet surface (yellow arrows) of joints produced under high (A) and low (B) heat input conditions.

Although small variations were identified between VR measured by VR_A and $VR_{\mu\text{-}ct}$, the simplifications assumed by Equation 1 did not highly affect the results and showed to be in a good agreement with the trends identified by the microCT. Therefore, VR_A is a good approach to efficiently calculate the polymer interaction volume, and consequently, the anchoring efficiency. Further, the influence of VR on the mechanical performance of the HEI and LEI joints will be discussed in Section 5.2.5.

5.2.3. Analysis of joints interface

As discussed previously in Section 5.2.1, the composite matrix is molten and its viscosity is reduced during the joining process due to the peak temperature achieved. Amancio-Filho [30] investigated the effect of the frictional heat generated during the joining process on the microstructure of the friction-riveted joints. The author reported that, due to the peek temperature achieved (above t_g and t_m) a polymer thermo-mechanically affected zone (PTMAZ) is formed at the vicinities of the rivet inside the composite plate. The complete description of the microstructural zones identified into the friction-riveted joints can be found in [30, 33].

The internal features observed in the thermo-mechanically affected zone (CTMAZ) of the joints will be addressed in the present section. Figure 46 -A presents the cross section of a representative HEI joint obtained by optical microscopy. The composite thermo-mechanically affected zone (CTMAZ) analyzed in detail is highlighted by yellow dashed lines.

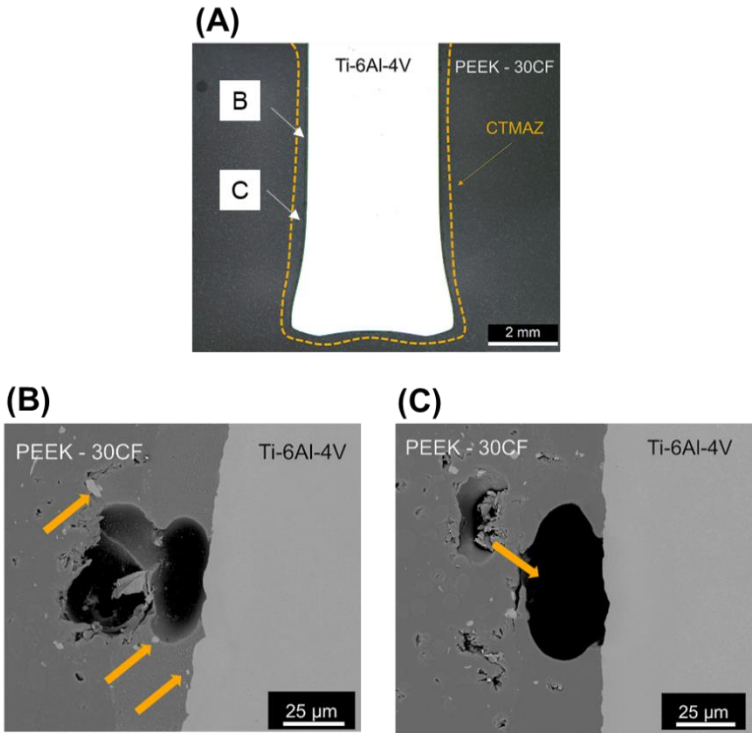

Figure 46 - Cross-sectional view of a Ti-6Al-4V/PEEK-30CF friction-riveted joint produced under high ENERGY input joining condition (A). Detailed images of metallic fragments (B) and (C) micro voids in the thermo-mechanically affected zone, CTMAZ.

Figure 46-B shows scattered metallic fragments in the composite part close to the interface (yellow arrows), as a result of the wear generated between the metal and composite parts during the joining process. The chemical composition of such fragments was analyzed by energy dispersive spectroscopy (EDS) and can be found in Appendix C.

Micro-voids were also observed on the composite part close to the metallic surface, as highlighted by yellow arrows in Figure 46-C. As discussed early in Section 5.1.3.1, it is believed that such micro-voids are not related to thermal degradation, since the peak temperature achieved during the joining process (510º C) was inferior to the onset degradation of PEEK (530°C) [63]. Therefore, air might be entrapped into the molten polymer during the joining process due to the outward material flow from the joining area. As a result, micro-voids can be formed during the joint consolidation.

The same features were identified for LEI joints. The cross section of a representative joint produced with LEI joining condition is shown in Figure 47 -A. By decreasing the energy input and consequently the frictional heat generated during the joining process, the wear between metal and composite is increased due possibly to higher friction between the joining parts. Therefore, higher amount and size of scattered metallic fragments in the metal-composite interface was observed for LEI joints. Figure 47 -B shows the bigger metallic fragments identified in the composite part, close to the interface in the joint produced under low heat input (yellow arrows). The micro-voids discussed previously for HEI joints were also identified for the LEI joints, as shown in Figure 47 -C. The micro-voids will be qualitatively described in detail in Section 5.2.3.1.

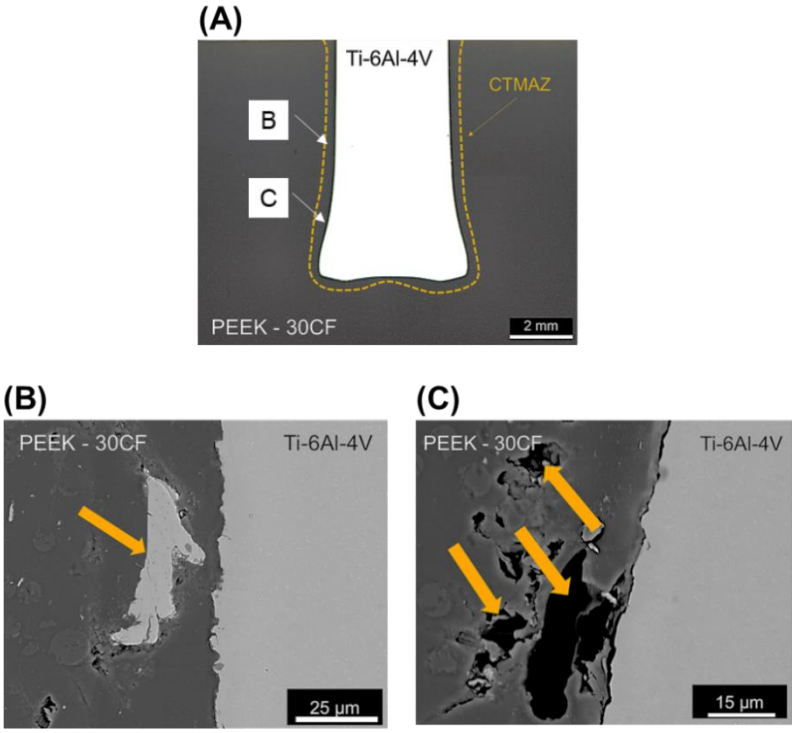

Figure 47 - Cross-sectional view of a Ti-6Al-4V/PEEK-30CF friction-riveted joint produced under low ENERGY input joining condition (A). Detailed images of metallic fragment (B) and (C) micro voids in the thermo-mechanically affected zone, CTMAZ.

Additionally, some micro-cracks were observed by microCT in the composite part in HEI joints. The micro-cracks are concentrated in the surroundings of the deformed rivet tip in the composite part, as shown in Figure 48-A. A representative

distribution of the micro-cracks was observed in different layers of the composite, indicated by white arrows (Figure 48-B). The cracks were concentrated only close to the deformed rivet tip what may be caused by stresses induced by the plastic deformation. It is believed that such flaws can be also the result of the high joining force applied to the still solid composite at the rivet shaft. Additionally, differences in thermal expansion coefficients can also create such effect.

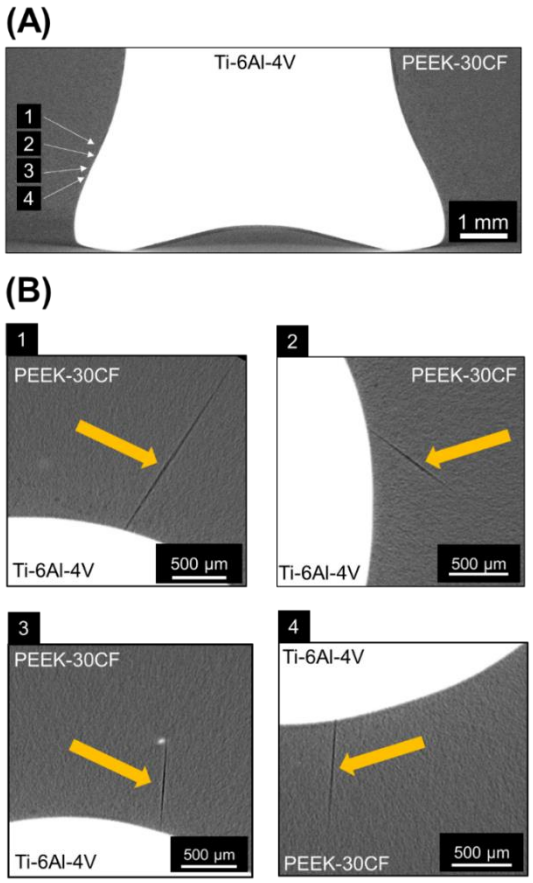

Figure 48 - (A) Cross-sectional view of a representative HEI joint in the plastically deformed zone of the rivet tip. (B) The distribution of the micro-cracks can be observed as the scanning advances into the composite part from B (1 to 4) (yellow arrows).

Micro-cracks were also identified for joints produced under low heat input joining condition. Figure 49-A shows the cross section of the HEI joint and the composite layers where the cracks were identified. The Regions 1-3 in Figure 49-B (1 to 3), which are located far from the joining area, depict the first micro-cracks observed around the inserted rivet. Considering the low energy input, the high

forces applied into the solid volume of composite during the rivet insertion can induce cracks radially to the rivet shaft. In Region 4 (Figure 49-B (4)), where the rivet tip widening occurs, longer cracks were identified. Due to the high plastic deformation, internal stress may cause the flaws. Additionally, differences in thermal expansion coefficient can also lead to such effect during the cooling of the joints.

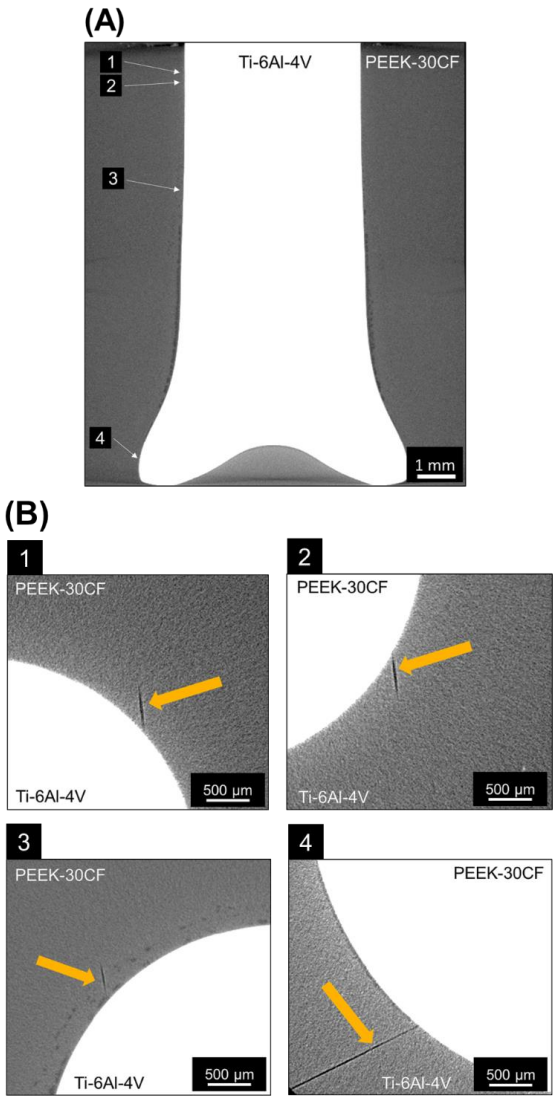

Figure 49 - Cross-sectional view of a representative LEI joint in the anchoring zone. The distribution of the micro-cracks can be observed as the scanning advances into the composite part from B (1 to 4) (yellow arrows).

5.2.3.1.
Internal flaws

The distribution of the micro-voids through the composite-thermo-mechanically affected zone (CTMAZ) in different layers along the rivet shaft were assessed for HEI and LEI joints, as shown in Figure 50 and Figure 51, respectively. The extension of micro-voids increased around the deformed rivet tip for both joining conditions. The material in this region is exposed to temperatures above the melting temperature of the composite (Section 5.2.1), leading to decrease of the polymer viscosity. Therefore, such material can easily flow outward the joining area during the rivet insertion and deformation, contributing to the lack of material in the region and formation of micro-voids.

By comparing the internal features of HEI and LEI joints, it is possible to note that micro-voids are more pronounced around the deformed rivet in joints produced under low energy input joining condition (Figure 51 -B (2 to 4) magnified view) than in joints produced under high energy input joining condition (Figure 50-B (2 to 4) magnified view). Moreover, the adhesion of the molten polymer on the rivet surface in HEI joints is better when compared to LEI joints, as shown in Figure 50-B (2 to 4) magnified view) and (Figure 51-B (2 to 4) magnified view). The high amount of internal micro-voids around the deformed rivet might be an indication of less effective micro-mechanical interlocking between the parts in LEI joints. It's also believed that the low adhesion observed between polymer and metal interface is a result of the differential contraction (shrinkage) by the materials during the joint consolidation under pressure.

However, the volume of polymer matrix affected by the frictional heat and consequently the volume of micro-voids formed during the joining process in LEI joints was expected to be less pronounced compared to HEI joints due to the low peak temperature achieved. It is important to notice that the microtomography analysis was carried out for just one replicate, requiring further experiments to further understand the results obtained so far.

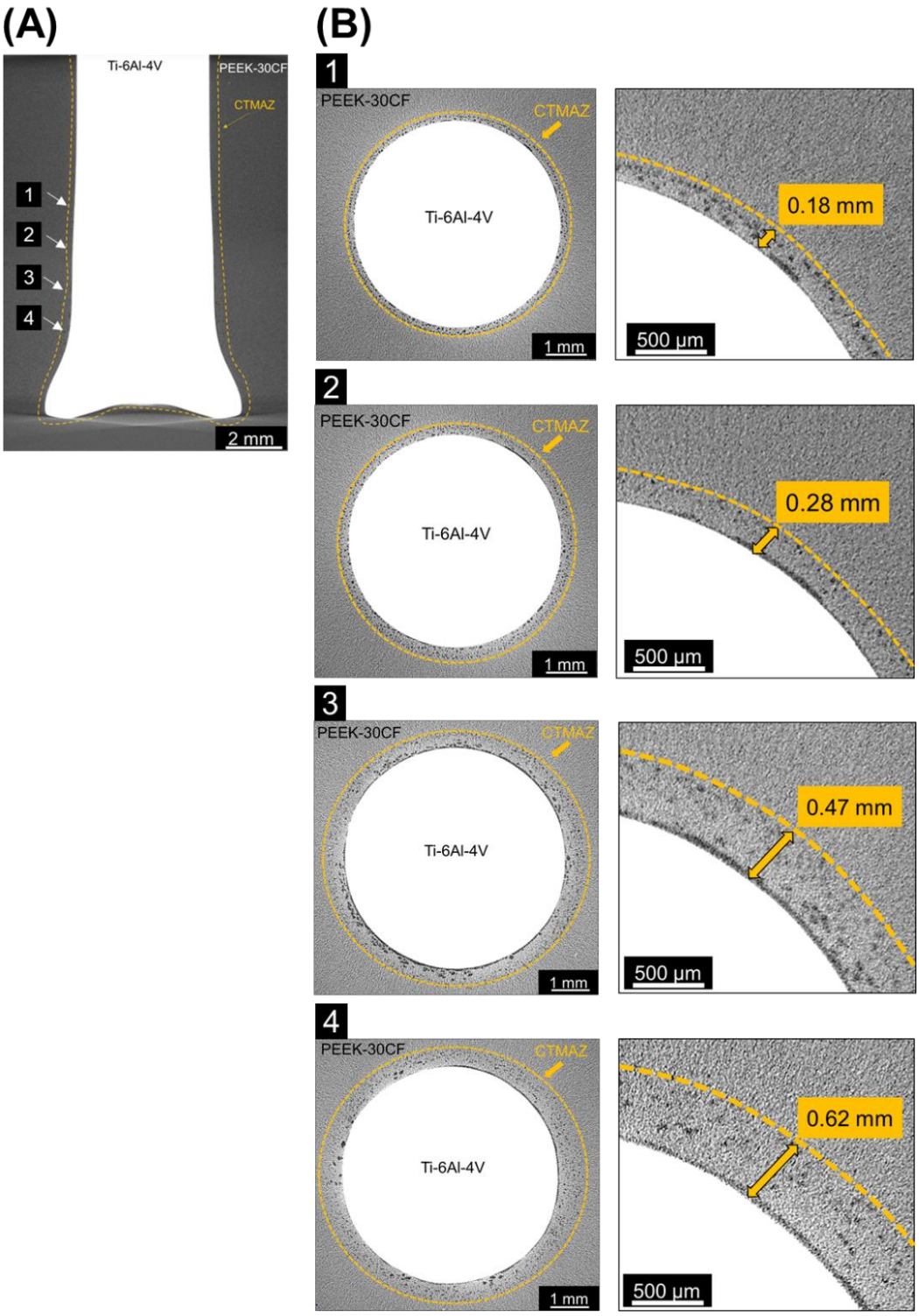

Figure 50 - (A) Overview of a HEI joint, where four regions of interest at the metal-composite interface are indicated at the CTMAZ (highlighted by yellow dashed lines). The distribution of micro voids in the surroundings of the plasticized rivet can be observed as the scanning advances into the composite part from B (1 to 4).

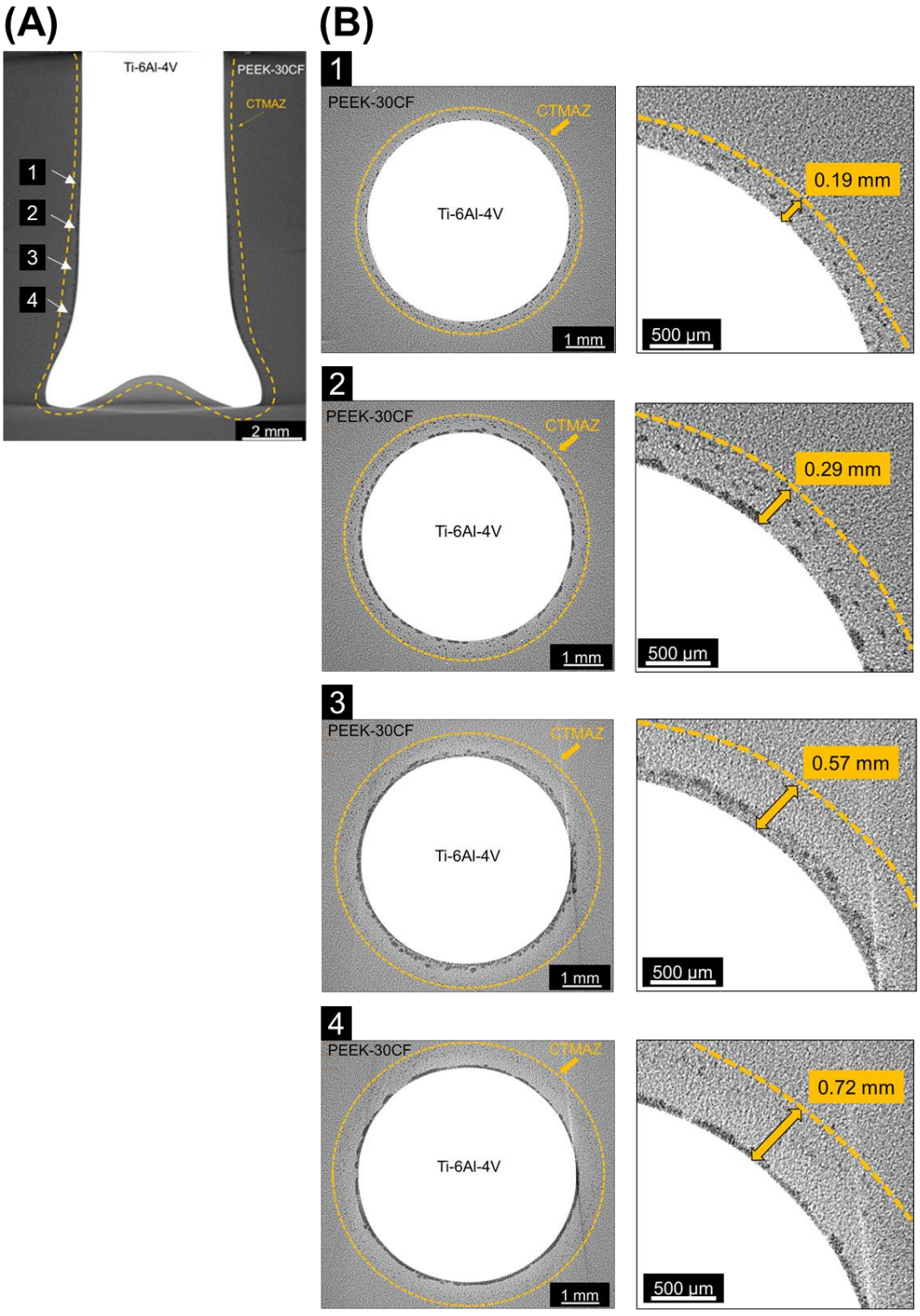

Figure 51 - (A) Overview of a LEI joint, where four regions of interest at the metal-composite interface are indicated at the CTMAZ (highlighted by yellow dashed lines). The distribution of micro voids in the surroundings of the plasticized rivet can be observed as the scanning advances into the composite part from B (1 to 4).

5.2.4.
Local mechanical performance

Figure 52 shows a typical cross-section of HEI and LEI friction-riveted joint along with the Vickers microhardness mapping of half of the Ti-6Al-4V rivet. The local mechanical measurements were carried out according to the procedure described in Section 4.2.4. As reported by Amancio-Filho *et al*. [79] the microhardness distribution of joints produced by Friction Riveting is influenced by the process-related microstructural changes in the metal and composite.

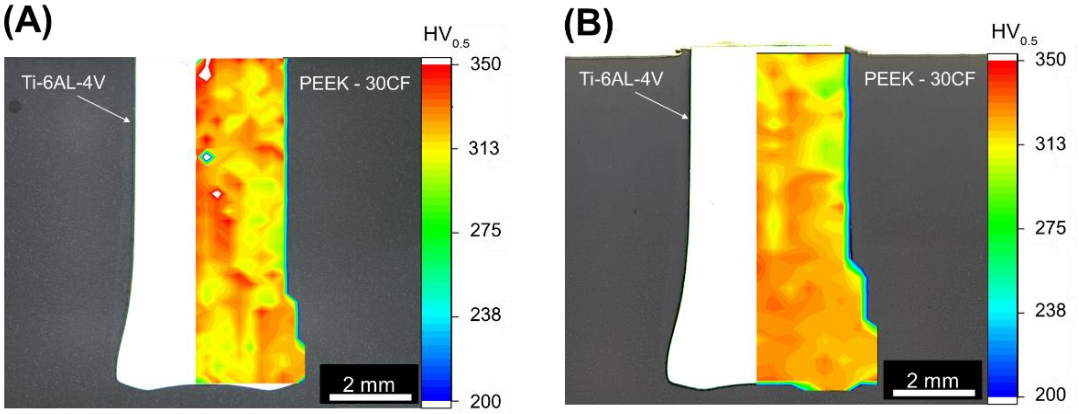

Figure 52 - Cross-sectional view and microhardness distribution of the Ti-6Al-4V deformed rivet produced under high (A) and low (B) joining condition.

The hardness along the rivet length ranged from 322 HV to 336 HV for HEI joint while for LEI the range was from 320 HV to 337 HV. A decrease of 19% in microhardness was observed at the plastically deformed rivet tip for HEI and LEI joints in comparison to Ti-6Al-4V base material (345 HV). As previously discussed in Section 5.2.1, no microstructural transformation is expected through the rivet length during the joining process for both joining conditions since the peak temperatures achieved (510 ºC for HEI joints and 421 ºC LEI joints) are below the β-transus temperature of the Ti-6Al-4V. Figure 53-A and B, illustrates the microstructure of the deformed rivet tip for HEI and LEI joints, showing no morphological changes compared to the equiaxed microstructure of the Ti-6Al-4V base material (Figure 10). It is believed that the microhardness decreased in this region near to the deformed rivet tip due to the possible dynamic recovery phenomena [80]. This phenomena can occur in the surrounds of the deformed rivet

tip due to this region being responsible for the higher frictional heat generated between the parts during the rivet insertion. As a result, dislocations are eliminated which decrease the local microhardness.

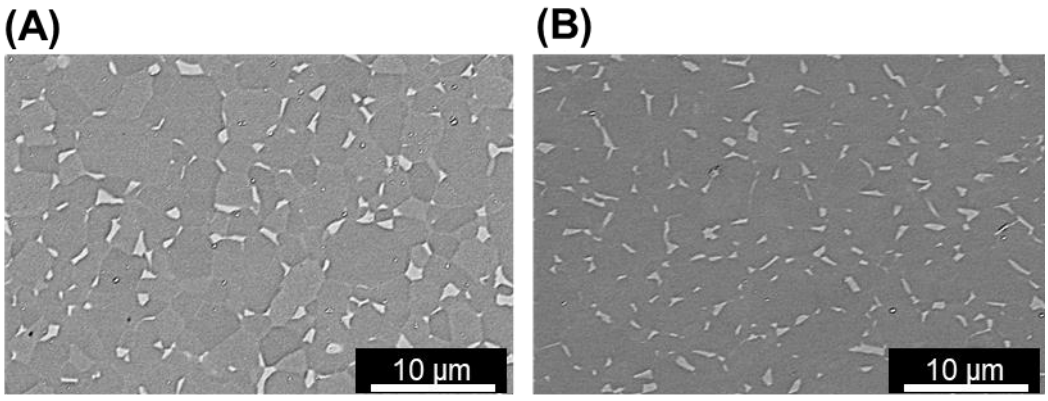

Figure 53 - Microstructural details in the Ti-6Al-4V rivet tip for (A) HEI and LEI.

5.2.5. Global mechanical performance and failure mechanisms

T-Pull testing was performed to investigate the quasi-static mechanical performance of friction-riveted joints following the procedure described in section 4.2.5.2. Figure 54 shows a comparison of the mechanical performance (ultimate tensile force, UTF) of joints produced under both joining conditions.

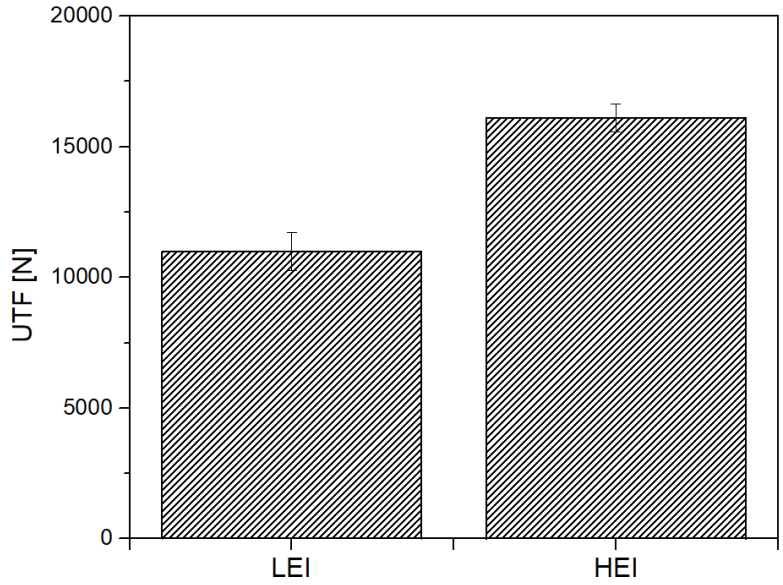

Figure 54 - Ultimate tensile force (UTF) of friction-riveted joints produced under high and low heat input conditions.

Joints produced under high heat input joining condition achieved ultimate tensile force (UTF) 46 % higher (16110 ± 530 N) than low heat input joints (10993 ± 739 N). This may be related to the influence of the joining conditions on the joints internal features. As described in previous investigations [37], by increasing the rivet tip widening and rivet penetration depth, the anchoring of the rivet into the composite is improved, leading to stronger joints. Therefore, as a result of the higher frictional heat generated during the joining process, the HEI joints present 10% larger plastically deformed rivet tip (W = 8.17 ± 0.69 mm) compared to the LEI joints (W = 7.38 ± 0.40 mm), as shown in Section 5.2.2.

Additionally, the HEI and LEI joints presented different concentration of internal defects at the metal-polymer interface (Section 5.1.2.1). HEI joints showed lower amount of micro-voids (Figure 50) in comparison to LEI joints (Figure 51) which led to a better micro-mechanical interlocking between the parts. Although, the LEI showed a higher amount of micro-voids at the metal-polymer interface, it is believed that the rivet tip widening of the joints had the most significant contribution in the tensile force of friction-riveted joints.

HEI joints, which presented higher mechanical performance, failed by shear through the rivet while weak joints produced under LEI conditions failed by full-

rivet pull-out, as shown in Figure 55-A and B. It is worth to note that the maximum loads recorded for HEI joints comprised about 89% of the rivet base material tensile strength (950 MPa). As discussed in Section 5.2.4, no microstructural transformation was observed through the rivet length during the joining process for both joining conditions. Furthermore, a deeper investigation may be carried out to understand the influence of the grips used during the T-PULL testing machine on the failure mode observed for HEI joints. The joints failed by shear through the rivet inside the grips before reaching the maximum material (Ti-6Al-4V) tensile strength. However, this analysis is not within the scope of this work and will not be addressed in this dissertation.

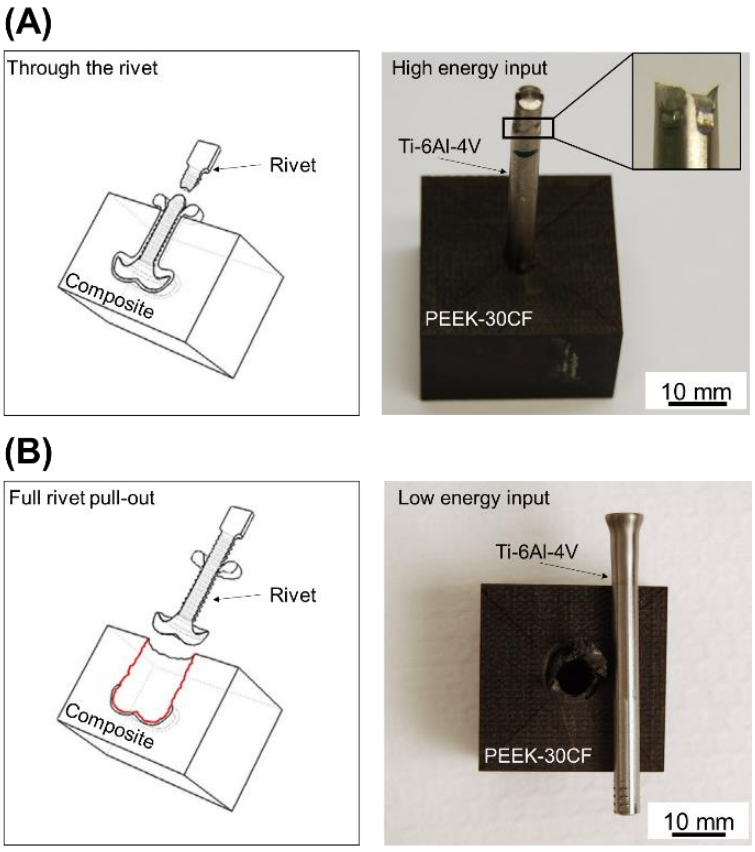

Figure 55 - (A) Representative description of “Through the rivet” failure mode (adapted from [81]) and an example of the ductile fracture on the rivet outside of the joint area in HEI joint. (B) Representative description of “full rivet pull-out” failure mode (adapted from [81]) and an example of HEI joint where the rivet is completely removed, leaving an orifice with a diameter similar to the deformed rivet tip.

5.3.
Ultrasonic joining

5.3.1.
Temperature evolution

The temperature development during the U-Joining was recorded at the interface between polymer and pin for the joints produced with both high and low energy input, as shown in Figure 56. After approximately 0.5 seconds, the gap between the metallic and polymeric parts is closed, due to the complete penetration of the pins, i.e. when the surface of the MIMStruct touches the polymeric part. As a result, a cut-off point for the temperature recording is reached. Therefore, the maximum temperature recorded by the infrared camera may not reflect the maximum temperature experienced by the materials during the joining process.

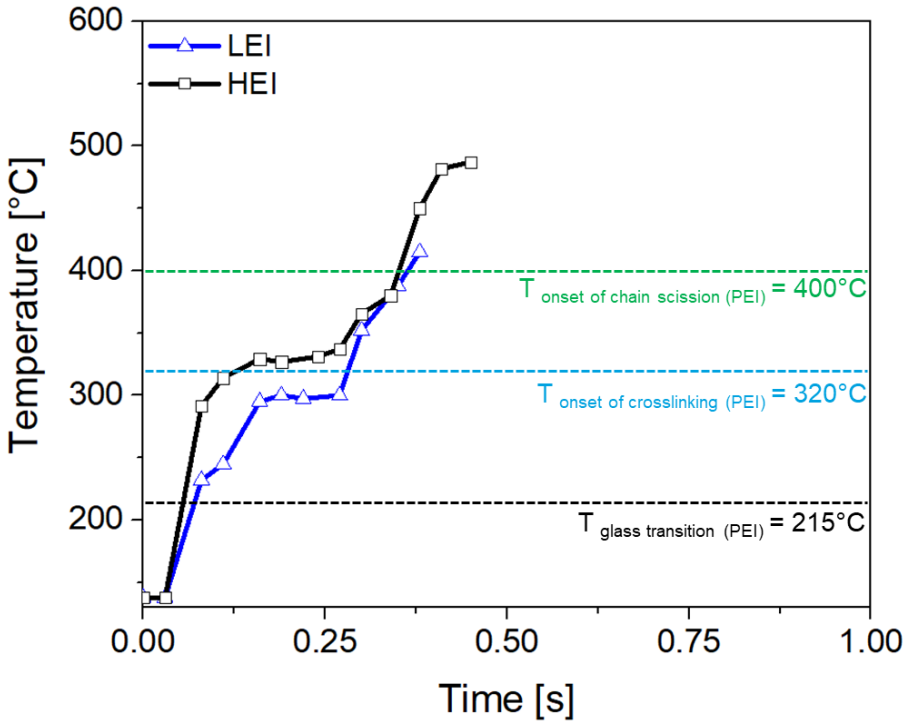

Figure 56 - Process temperature evolution recorded by infrared thermography at the interface between polymer and pin tip for both low and a high energy input condition. The temperature of glass transition, onset of crosslinking and onset of chain scission are schematically shown in the figure by the green, blue and black dotted lines respectively.

Nevertheless, the recorded temperatures at the interface were significantly high and correspond to 487 ± 39 ºC for the HEI and 414 ± 39 ºC for the LHI condition. These temperature levels are above the T_g of PEI (215 ºC) [67]. Therefore, during the joining process, a low viscosity state of the polymer, especially around the pins, is expected. Moreover, the maximum recorded temperature levels are within the degradation temperature range of PEI, which occurs in two stages: crosslinking and chain scission [82]. Kuroda *et al.* [67] reported crosslinking is found to lie between 320 - 380 °C, whereas the onset of chain scission occurs at 400 °C.

Although the degradation temperature range was reached during the U-Joining, one should take into consideration that the joining cycles were very short (1.15 ± 0.1 and 1.75 ± 0.1 for the LEI and HEI condition respectively), as shown in Table 10. Consequently, an extensive thermal degradation of the PEI part is not expected. Moreover, the maximum recorded temperature for LEI and HEI conditions corresponding to about 27-32 % of the Ti-6Al-4V melting point (1660 ºC [56]) and considerably below the β-transus temperature of the Ti-6AL-4V (995 ºC [56]). Thus, no microstructural changes are expected through the joint metallic part during the U-Joining, as previously reported in the literature [40, 41].

5.3.2. Joints formation

Figure 57 and Figure 58 present the 3D-reconstructed microCT images of the analyzed samples. As can be seen, the through-the-thickness reinforcement, structured on the Ti-6Al-4V-0.5B, was fully inserted into the polymer plate. As discussed previously in Section 5.3.1, the recorded average peak temperature observed for HEI (487 ± 39 ºC) and LEI (414 ± 39 ºC) joints was high enough to decrease the polymer viscosity. This suggests that the heat created by friction at the interface combined with joining pressure (Table 10) led to a smooth penetration of the pins. As a result, an effective macro-mechanical interlocking is achieved for both joining conditions, as shown in Figure 57-B (1 to 3) and Figure 58-B (1 to 3). Furthermore, one may expect significant improvement in terms of out-of-plane mechanical performance of such hybrid joints, due to an improved load transfer between metal and polymer [40, 41].

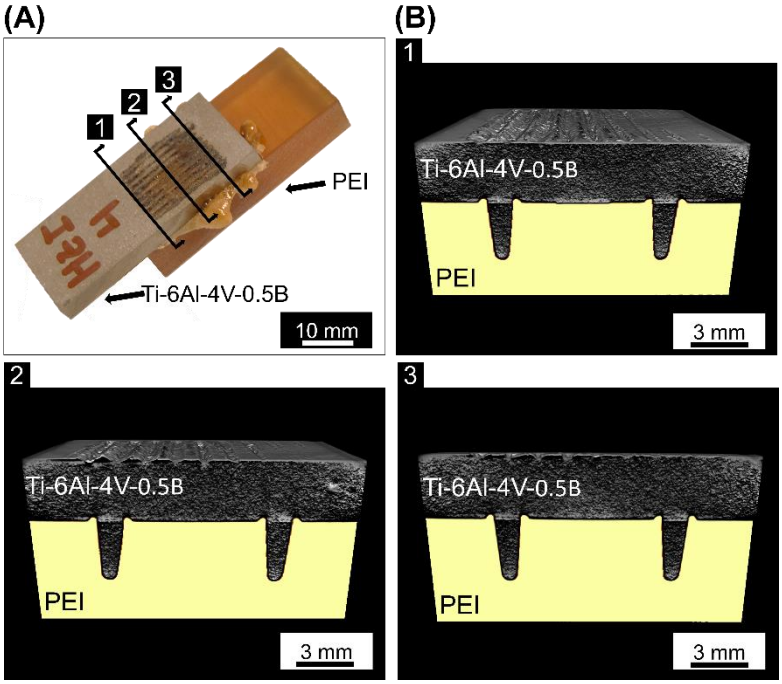

Figure 57 - (A) Schematic cut view of the three different cross-sections (black lines) evaluated in the 3D-reconstructed image of the HEI joint. (B) Detailed 3D-reconstructed images of the mentioned cross sectional cut 1, 2 and 3.

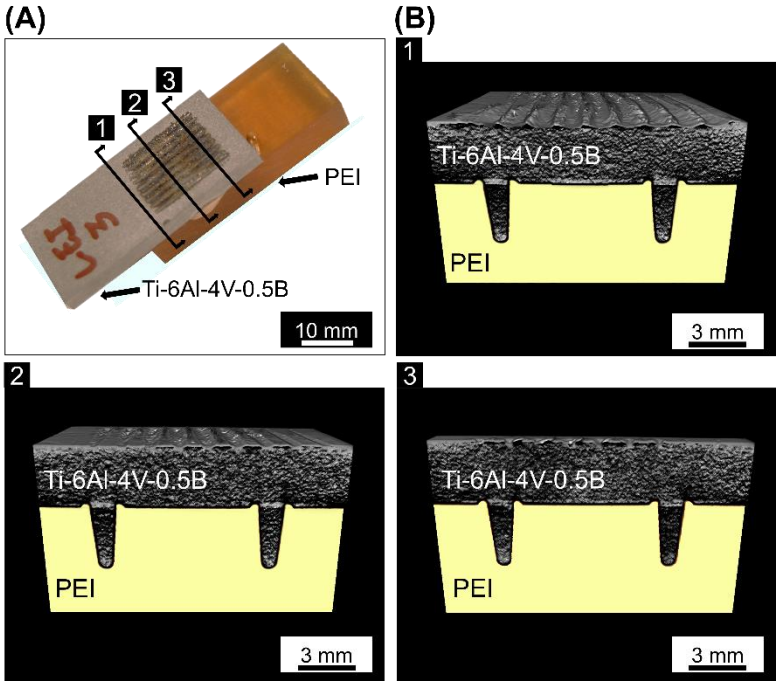

Figure 58 - (A) Schematic cut view of the three different cross-sections (black lines) evaluated in the 3D-reconstructed image of the LEI joint. (B) Detailed 3D-reconstructed images of the mentioned cross sectional cut 1, 2 and 3.

As can be seen in Figure 59-A (HEI) and B (LEI) in the 3D-reconstructed image of the MIMStruct, the pins integrity was preserved. Therefore, no damage or deflection of the structured trough-the-thickness reinforcement was observed after the joining process for HEI and LEI conditions.

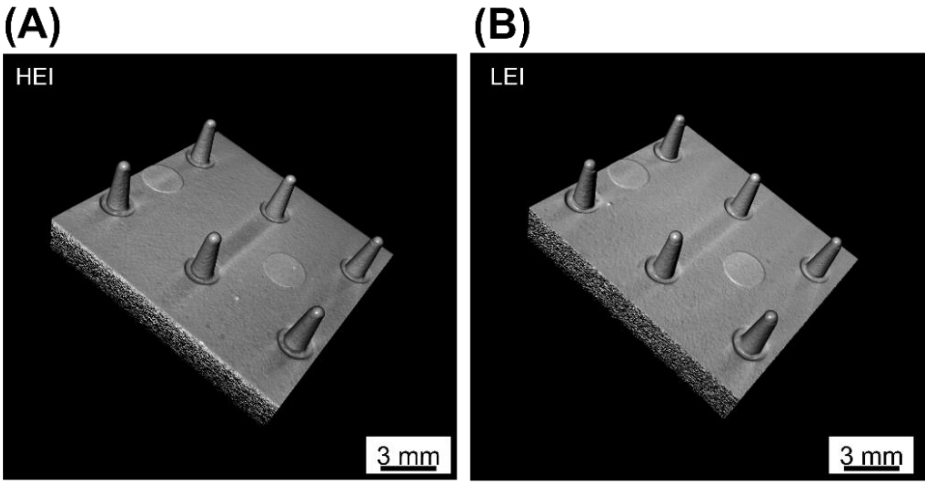

Figure 59 - 3D-reconstructed image of the MIMStruct for HEI (A) and LEI (B) joining conditions.

Furthermore, it is possible to note that the MIM-structured metallic part produced by metal injection molding has a geometrical undercut around the six conical pins, as shown in Figure 60-A and B (Magnified view of a selected pin) indicated by yellow arrows. The designed geometrical undercut was created on the surface of the metallic part to reduce the stress concentrations around the base of the pins. As discussed previously, the polymer matrix is molten during the joining process and flows upwards filling the undercut around the six pins due to the intimate contact between the joining parts provided by the axial force applied. Figure 61-A (HEI) and B (LEI) presents the 3D-reconstructed images obtained by microCT, showing the consolidated molten polymer entrapped into the geometrical undercut around the six conical pins (indicated by white arrows) for joints produced under HEI and LEI joining conditions. In addition, the macro- and micro-mechanical interlocking between the joining parts were also improved, as reported by Feistauer *et al.* [40, 41].

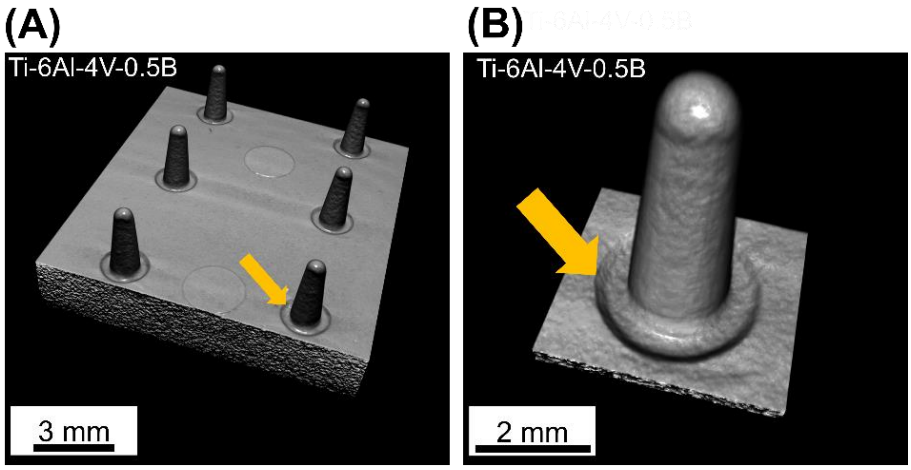

Figure 60 - (A) 3D view of MIM-structured metallic part produced by metal injection molding and (B) magnified view of a selected pin, showing the undercut.

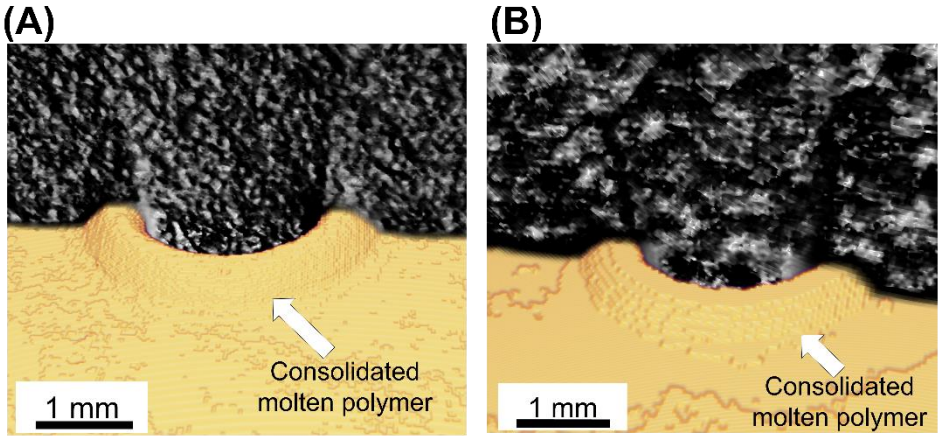

Figure 61 - 3D microCT images of the reconsolidated molten polymer at the undercut region for (A) HEI and LOW (B) joints.

In addition, the volume of consolidated molten polymer around the undercuts was segmented and measured, as shown in a 3D view in Figure 62-A and B (indicated by yellow dashes). The higher the joining energy, the higher is the expected process temperature, as previously discussed and measured. Thus, during the joining it is also expected an increased volume of softened polymer around the pins. The combination of higher volume of molten polymer and axial force applied by the sonotrode might increase the material flow and improve the undercut filling by this material and the bonding area. As a result, it might improve macro-mechanical interlocking between the parts. The measured volume of consolidated

molten/softened material around the undercut corroborates this assumption. The volume measured for the HEI was 69 mm^3 and for the LEI was 40 mm^3.

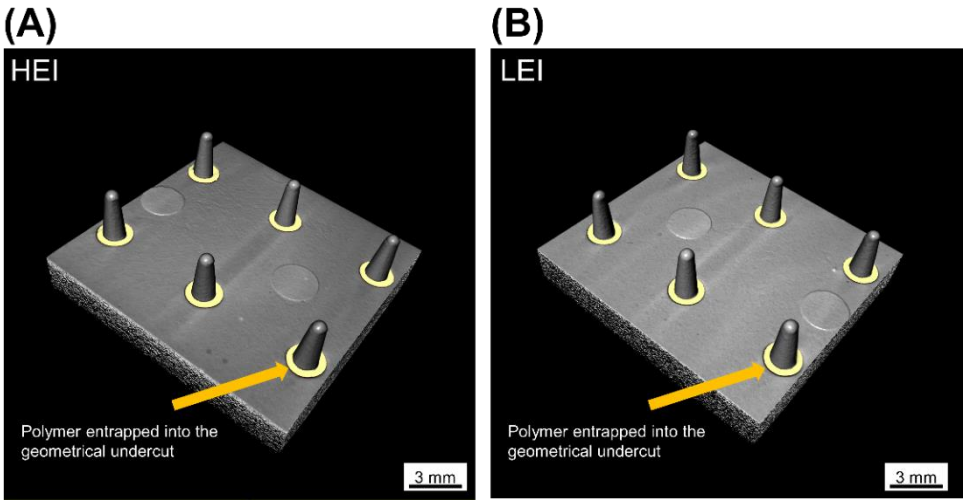

Figure 62 - 3D representation of the consolidated molten polymer volume around the undercuts for the HEI (A) and LEI (B) joints views.

5.3.3. Analysis of joints interface

The effect of the joining process on the microstructural changes of the base materials was evaluated by optical microscopy. As reported by Feistauer [41], the micro-mechanical interlocking is one of the bonding mechanisms at the metal-polymer interface responsible for the strong shear strength of the ultrasonically joined joints [40]. Such micro-mechanical interlocking between the parts is microscopically provided by the entrapment of softened polymer into the irregularities of the MIM-structured metallic part. In this way, this section presents the analysis of the metal-polymer interface of the HEI and LEI joints.

Figure 63-A and Figure 64-A present the cross sections of representative HEI and LEI joints. The regions of the metal-polymer interface analyzed in detail are marked as B, C and D and highlighted by yellow dashed lines (polymer thermo-mechanical affected zone).

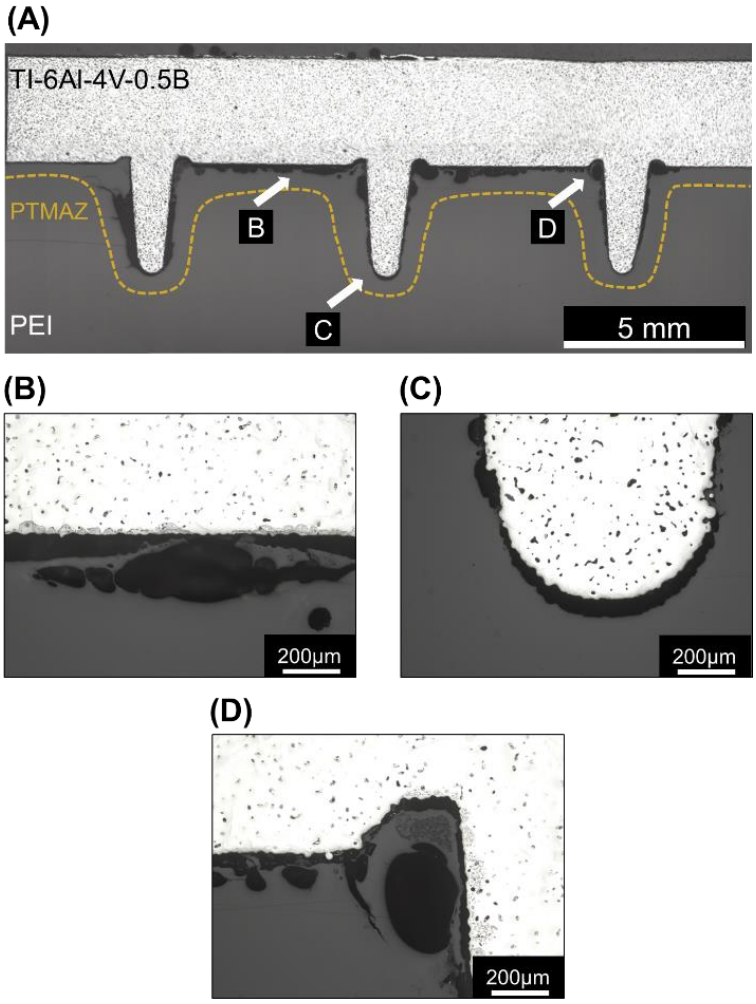

Figure 63 - (A) Cross-sectional view of HEI joint obtained by metallographic preparation. Detailed images of metal-polymer interface (B), pin-polymer interface (C) and pin undercut filling (D).

Figure 63-B and C shows the contact between metal-polymer surface and pin-polymer interface, respectively. As previously shown by microCT images, Figure 63-D also presents the geometrical undercut filled with consolidated molten polymer. As can be seen, both images presented a considerable amount of thermal induced micro-voids. It is believed that micro-voids can be related to the thermal degradation of polymer due to the peak temperature achieved (as shown in Section 5.3.1), air entrapped or differential contraction (shrinkage) by the materials during the joint consolidation.

The same regions were analyzed in detail for LEI joints, as shown in Figure 64-B to D. However, by decreasing the energy input and consequently the frictional

heat generated during the joining process, micro-voids are less pronounced at the metal-polymer interface in LEI joints.

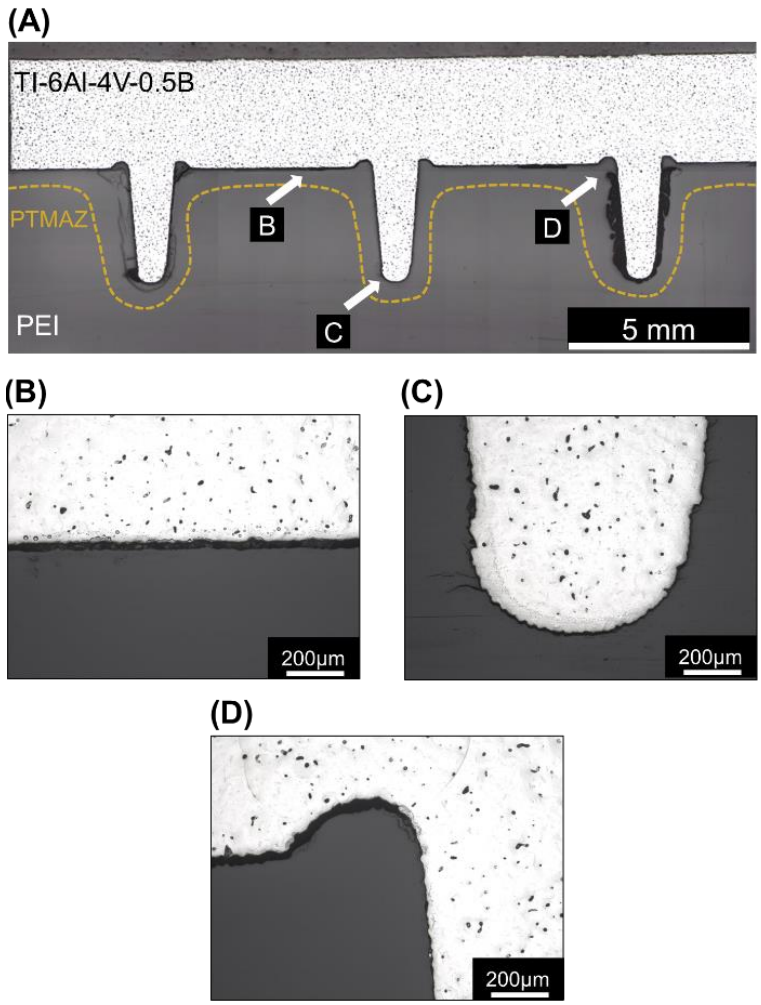

Figure 64 - (A) Cross-sectional view of HEI joint obtained by metallographic preparation. Detailed images of metal-polymer interface (B), pin-polymer interface (C) and pin undercut filling (D).

5.3.3.1.
Internal flaws

The thermal-induced flaws created during the joining process were non-destructively evaluated by microCT. As previously discussed in Section 5.3.2, micro-voids were observed distributed in the PTMAZ at the metal-polymer interface and around the pins. Moreover, the PEI in U-Joining joints in this work was only exposed to high temperatures in very short joining cycles. As previously given in Table 10, the average joining cycles in LEI joints was (1.15 ± 0.1 s),

whereas (1.75 ± 0.1 s) was achieved in HEI joints. Therefore, extensive thermal degradation of PEI during the process is not expected to occur in such conditions. Therefore, Feistauer *et al*. [40] reported that an extensive degradation of the polymeric part is not expected to occur in U-Joining joints due to the very short joining cycles achieved during the process. The author also reported that the temperature development during the U-Joining is restricted to small volumes at the interface between polymer and pin tips which leads to a localized volume of process-affected polymer.

The description of the micro-voids distribution in the polymeric parts is important due to the fact that these features influence the joint global mechanical performance and failure modes. Figure 65-A depicts the HEI ultrasonically joined joint, showing the layers of different pins analyzed in details. These layers are marked as 1, 2, and 3 showing the microstructural features observed in the cross section of the joint. Figure 65-B indicates that micro-voids are just concentrated in the surroundings of the pins in cross section 1 and 2 as well as in the interface between the MIMStruct plate and the upper plate of the polymeric part, as we can also see in Figure 65-B, especially for layer 2. This observation demonstrated that the volume of process-affected polymer formed around the pin was higher in layers 1 and 2.

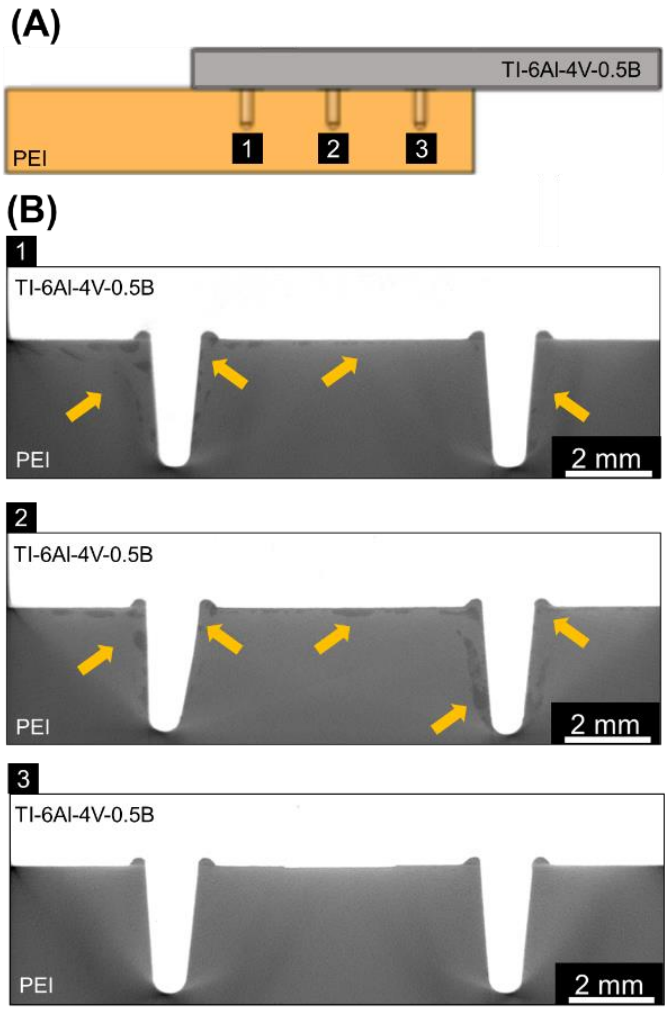

Figure 65 - (A) Representative description of the level of different pins analyzed in joint produced under high energy input joining condition (adapted from [40]. (B) Cross sectional views showing the distribution of the micro voids observed as the scanning advances at the metal-polymer interface.

For this reason, a detailed analysis was carried out in the pins located in layers 1 and 2, as shown in Figure 66 and Figure 67. The regions of the metal-polymer interface analyzed in detail are marked as A, B and C in both cross sectional views in Figure 66-1 and Figure 67-1. The distribution of micro-voids observed at the metal-polymer surface, as a result of the process-affected polymer expelled from the joining area, can be observed in Figure 66-1 (A) and Figure 67-2 (B). In addition, micro-voids were also observed in the surroundings of the pins, as shown in Figure 66-1 (B and C) and Figure 67-2 (B and C), highlighted by yellow arrows.

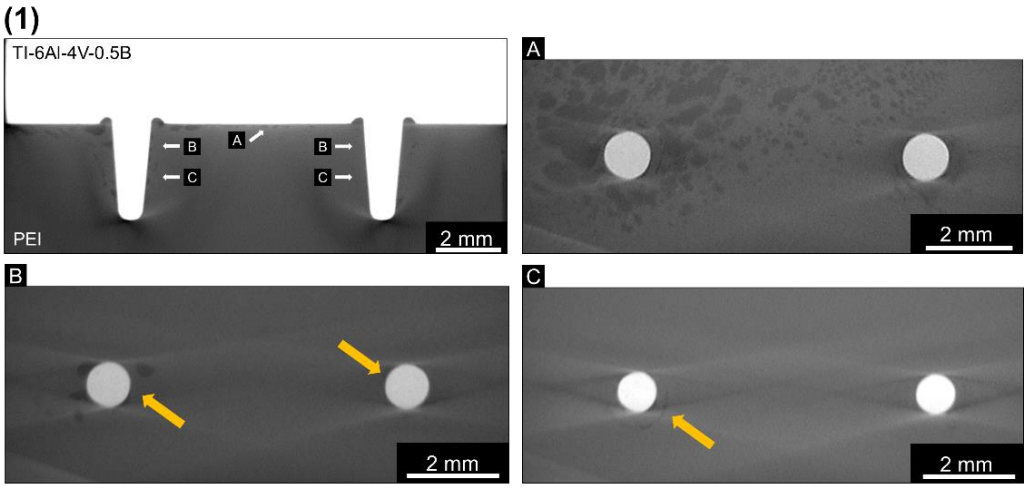

Figure 66 - (1) Cross-sectional view of HEI joint. Top-view of the joint showing the micro-voids located at the metal-polymer surface (A) and pin-polymer interface (B and C).

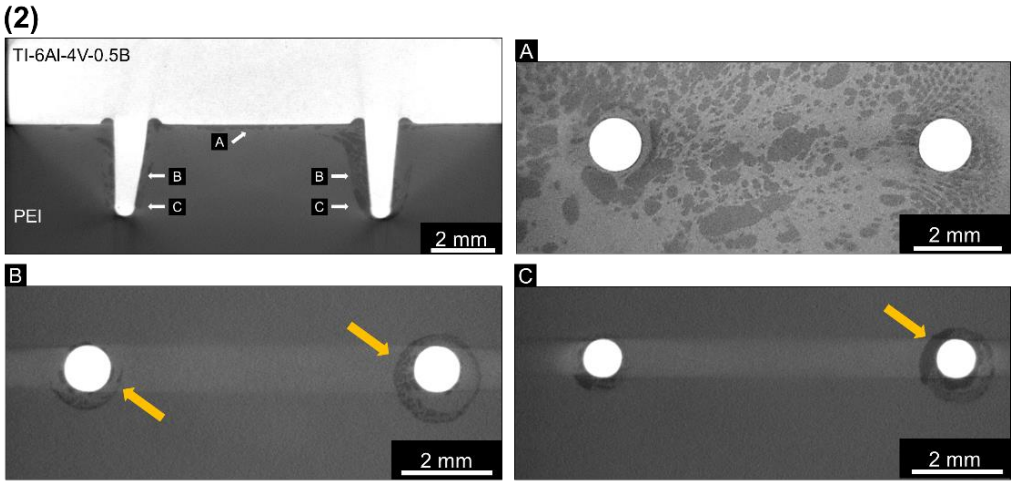

Figure 67 - (2) Cross-sectional view of HEI joint. Top-view of the joint showing the micro voids located at the metal-polymer surface (A) and pin-polymer interface (B and C).

It is worth to note, as indicated in Figure 68-A (by black arrows), that microvoids were also observed at the end of the overlap joint between metal and polymer surface (Figure 68–B), which explains the failure mode observed in joints produced with HEI joining condition. The mechanical behavior and failure modes of this joints will be addressed in detail in Section 5.3.4.

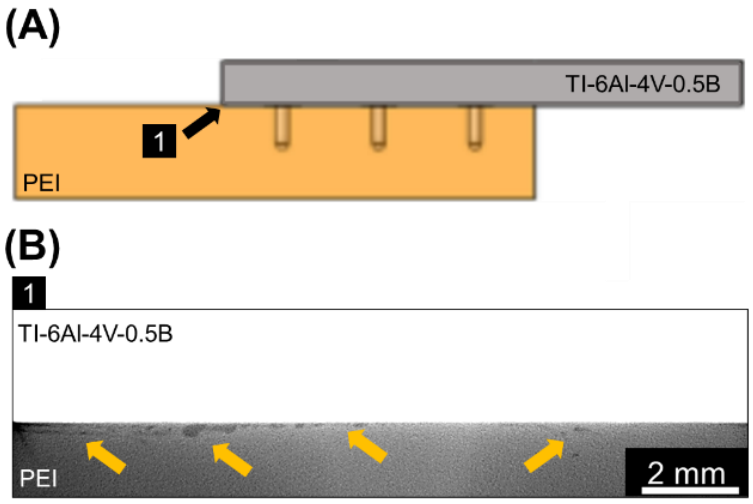

Figure 68 - (A) Representative description of the level of different layer analyzed in joint produced under high energy input joining condition (adapted from [40]). (B) Cross sectional view showing the distribution of the micro-voids in the selected layer at the metal-polymer interface.

Detailed evaluation of micro-voids through X-Ray micro-computed tomography for LEI joints could not be addressed in this work as the micro-voids were not visualized at the metal-polymer interface for this condition. It is important to notice that the microCT parameters (Table 11) used to obtained 3D digital images were identical for both joining conditions. However, as shown in Section 5.3.3, by decreasing the energy input a less pronounced volume of microvoids was observed at the metal-polymer interface. In this way, further investigations should be carried out to visualize these internal features and understand their influence on the mechanical performance and failure mode of LEI joints.

5.3.4. Global mechanical performance and failure mechanisms

The quasi-static mechanical performance of the through-the-thickness reinforced joints was assessed through quasi-static lap shear testing following the procedure described in Section 4.2.5.1. Figure 69 shows a comparison of the mechanical performance (ultimate lap shear force, ULSF) of HEI and LEI joints.

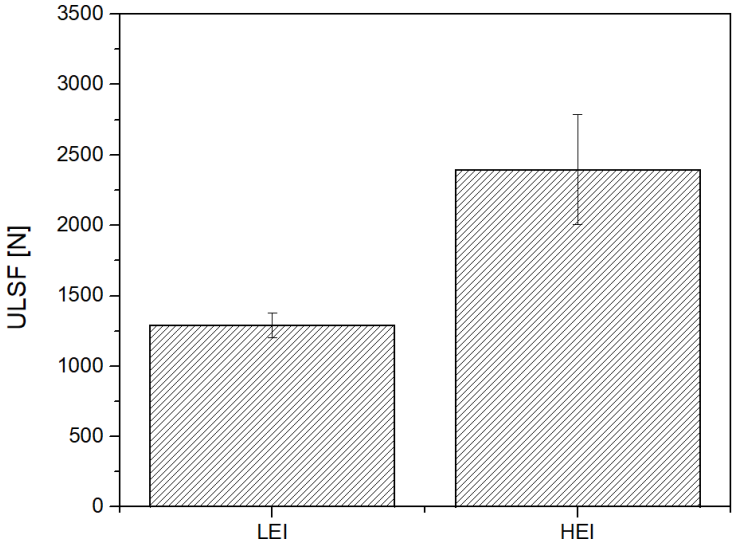

Figure 69 - Ultimate lap shear (ULSF) of U- Joining joints produced under high and low heat input conditions.

The joints produced with HEI achieved ultimate lap shear force (ULSF) 85% higher (2394 ± 553) than LEI (1291 ± 91). This may be related to the influence of the joining conditions on the bonding area created between metal and polymer part. As discussed previously in Section 5.3.3, the higher frictional heat (2800 J; peak temperature of 487 ± 39 ºC) generated between the joining parts led to a higher volume of molten polymer expelled from the joining area compared to joints produced under low heat input joining condition (2000 J; peak temperature of 414 ± 39 ºC). It suggests that the higher volume of molten polymer generated by frictional heat combined with joining pressure led to the increased bonding area between the metal and polymer in HEI joints, especially at the interface between the MIMStruct plate and PEI lower.

Although the presence of higher amount of defects in the HEI condition did not affect negatively its quasi-static mechanical performance, it has changed its failure mechanisms in comparison with the LEI joints. The joints produced under high energy input failed catastrophically (through the polymer) due to “secondary bending”. Abibe [48] reported “secondary bending” as a stress concentration point which occurs in joints loaded in tension. It is believed that, the presence of microvoids (Figure 68-B (1)) at regions of stress concentration can work as nucleation sites for failure during the quasi-static loading test. In this case study, the cracks at the polymer base plate initiated from the microvoids observed at the

stress concentration point (red disk), as shown in Figure 70-A and B (indicated by yellow arrows), during the lap shear testing.

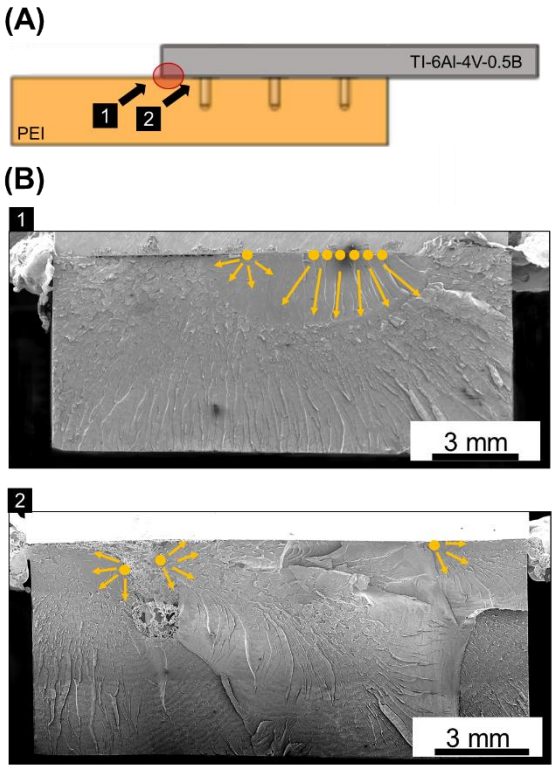

Figure 70 - (A) Schematic view of the zone in which the cracks initiated from the micro-voids at the polymer base plate in HEI joints (adapted from [40]). The red disk represent the stress concentration point in U-Joining joints. (B) 1 and 2 Cross section of the HEI fracture surface showed the crack propagation from micro voids at the stress concentration point (indicated by yellow arrows).

Joints produced under low heat input failed through a combination of shearing of the metallic pins and a mixed cohesive (CF) and adhesive (AF) failure in the consolidated molten polymer at the interface between upper and lower parts, as shown in Figure 71-A and B. After the fracture, reconsolidated molten polymer was found attached to the surface of the metallic part (black arrow), suggesting that an effective contact between the parts was achieved and corroborating the assumption of adhesive failure. On the other hand, plastic deformation (dimples on the pin fracture surface) was observed in the six metallic pins (Figure 71-A (2)), which led to a ductile fracture and consequently to a non-catastrophic final failure mode of the joints produced under LEI, as shown in picture (Figure 71-A (3)).

The cohesive-adhesive failure can be observed in the consolidated polymer molten layer at the polymeric plate surface, as shown in Figure 71-B (2). The torn polymer can be clearly observed into the cohesive failure part in Figure 71-B (2) (indicated by yellow arrow) as well as in the high magnification picture Figure 71-B (3). This is an indication that the polymer suffered plastic deformation prior to the final failure, what also contributed to a ductile fracture of the joints.

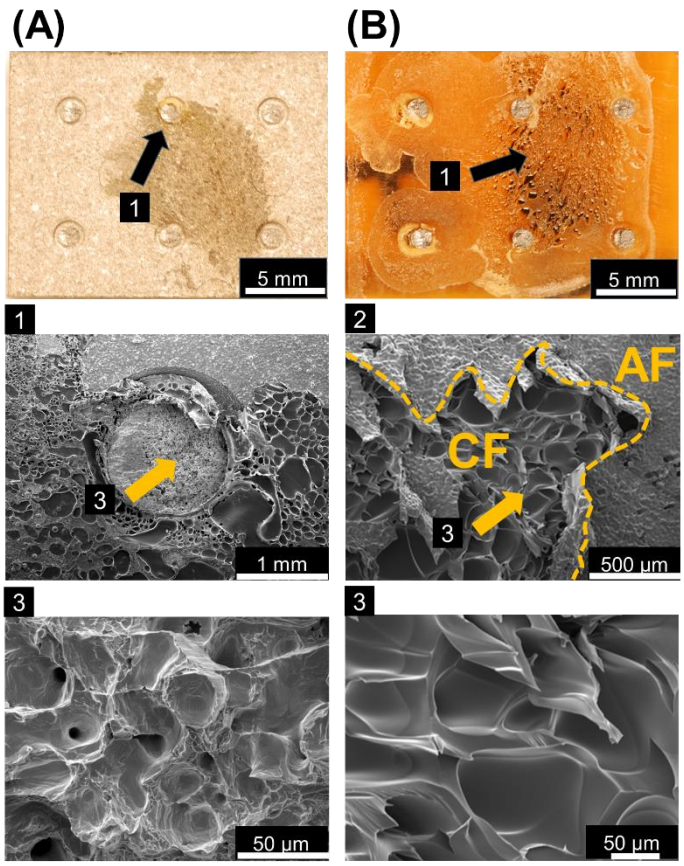

Figure 71 - Top-view (fracture surface) of the metallic (A) and (B) polymeric part after lap shear testing. (1) Detailed SEM micrograph at the pin region marked in (A) with the respective high-magnification image showing the fracture surface (3). (2) Detailed SEM micrograph of the polymeric molten layer marked in (B) with the respective high-magnification image showing the fracture surface (3).

6.
Conclusions

This master dissertation was devised to investigate the joint formation along with process-related changes of internal features and their correlation with joint mechanical performance. In the present work, metal-polymer/composite hybrid joints were produced using three new friction-based joining techniques: Ultrasonic Joining (U-Joining), Friction Spot Joining (FSpJ) and Friction Riveting (FricRiveting). Two joining conditions with different heat input levels (low and high) were selected to produce hybrid joints for each joining technology. The scope of the study included the evaluation of process temperature evolution, microstructural features, thermomechanical-induced flaws and interface quality, as well as the correlation with quasi-static mechanical performance. Moreover, the respective failure mechanisms of the joints were also investigated. This section is divided into four sub-sections to better present the final remarks of the work. The important findings led to the following conclusions:

6.1.
Advantages and drawbacks of X-Ray microCT

High-resolution tridimensional microCT characterization of the hybrid joints' internal features (i.e. micro-voids, micro-cracks, agglomerates, process-related joint geometrical changes) was performed to evaluate joint feature shape, size, and distribution. The microCT parameters were optimized for each joining process based on the compromise between the visibility and resolution along with the transmittance of each material combination. In addition, digital image processing and analysis was carried out by Dragonfly and FIJI software. The joints were segmented, colored and the internal features of the joints were quantitatively and qualitatively evaluated.

The microCT images, in combination with digital analysis, provided a great contribution to understanding the correlation between internal features and mechanical

performance of the friction-based joints, since it is a non-destructive 3D technique with potentially high precision of analysis.

Although satisfactory results were achieved by using microCT, some difficulties to quantify internal micro-voids were observed during the digital image processing for FricRiveting and U-Joining joints, due to the strong brightness and scattering between the metal-polymer/composite parts. In order, to obtain high quality images of these joints, further optimization of the microCT parameters is required, what can lead to a better discrimination of the internal flaws.

6.2. Friction spot joining

The maximum peak temperature observed on the aluminum surface for joints produced under HEI was 385 ± 5 ºC, while 332 ± 9 ºC was observed for the LEI joining condition. The highest peak temperatures achieved for both joining conditions are above the melting point of the PPS matrix and the PPS film interlayer (280 ºC). Nevertheless, extensive thermal degradation of the PPS matrix and the PPS film is not expected to occur during the joining process, due to the fact that the peak temperatures observed are below the onset temperature for PPS degradation (450 ºC).

Micro-voids were identified in the composite part close to the interface with the metal for HHI and LHI joints. It is believed that such micro-voids are not related to thermal degradation, air might be entrapped into the molten PPS during the joining process due to its outward flow induced by the axial movement of the tool. Micro-cracks were also observed into the metallic nub of HHI joints. It is believed that the micro-cracks provide additional sites for entrapment of PPS into the aluminum for the HHI joints, which is not found in the LHI joints.

The quasi-static mechanical performance of the joints was evaluated through lap shear testing. An ultimate lap shear force (ULSF) 43 % higher was observed for HHI joints compared to LHI joints. It is believed that it is a result of the larger plastically deformed zones achieved for the HHI joints (249 ± 28 mm^2) compared to the LHI joints (155 ± 11 mm^2). Furthermore, the HHI joints present two features which maximize the mechanical interlocking in this joints in comparison with the LHI joints: a metallic nub deformed in two rings (two points of macro-mechanical

interlocking) and the micro-cracks into the nub (additional sites for micro-mechanical interlocking). The higher amount of micro-voids observed at the metal-polymer interface for HHI joining condition has not significant influence on the mechanical performance of the joints.

6.3. Friction riveting

Extensive thermomechanical degradation was not observed in the composite matrix volume in the surroundings of the rivet as the peak temperatures achieved for HEI (510 ºC) and LEI (421 ºC) joints are below the degradation temperature of PEEK (530 ºC). The recorded temperature were peaking at 25-30 % of the Ti-6Al-4V melting temperature (1660 ºC). Although no melting is taking place, the temperature was enough to plasticize the metal but no morphological changes compared to the equiaxed microstructure of the Ti-6Al-4V base material were observed.

The volumetric ratio measured by analytical method (VR_A) and quotient provided by the microtomography analysis (VRμ-ct) presented similar trend. The averages obtained by analytical model were slightly superior to the measurement method what could be explained by the absence of replicates for microtomography and simplifications adopted by the analytical method such as symmetry on the deformed rivet and features on the rivet surface. Therefore, VR_A showed a good approach to efficiently calculate the polymer interaction volume, and consequently, the anchoring efficiency of friction-rivet joints.

Micro-cracks were observed by microCT in different layers of the composite. It is believed that such flaws can be a result of the high joining force applied to the still solid composite at the rivet shaft as well as related to the differences of coefficient of thermal expansion of the materials. Although, the LEI joints showed a higher amount of micro-voids at the metal-polymer interface, the higher plastic deformation on the rivet tip of HEI joints displayed the most important influence on the tensile force of friction-riveted joints. The joints produced under HEI joining condition achieved ultimate lap shear force (ULSF) 85% higher (2394 ± 553 N) than LEI joints (1291 ± 91 N).

Two different fracture mechanisms were observed: HEI joints failed by shear through the rivet while weak joints produced under LEI joining condition failed by full-rivet pull-out.

6.4. Ultrasonic joining

The recorded temperatures at the metal-polymer interface were significantly high and correspond to 487 ± 39 ºC for the HEI and 414 ± 39 ºC for the LHI joining conditions. These temperature levels are above the Tg of PEI (215 ºC) and caused a low viscosity state of the polymer, especially around the pins, what was expected. Although the degradation temperature range was reached during the process, an extensive thermal degradation of the PEI part was not observed due to short joining cycles (1.15 ± 0.1 s and 1.75 ± 0.1 s for the LEI and HEI condition respectively).

The pins were fully inserted into the polymeric plate and no damage or deflection of the structured trough-the-thickness reinforcement was observed after the joining process for HEI and LEI conditions. The consolidated molten polymer was entrapped in the geometrical undercut around the six conical pins what contributed to improve the macro- and micro-mechanical interlocking between the parts.

The joints produced with HEI achieved ultimate lap shear force (ULSF) 85% higher (2394 ± 553 N) than LEI (1291 ± 91 N) due to the increased bonding area between the metal and polymer in HEI joints, especially at the interface between the MIMStruct plate and PEI lower. Although a higher amount of defects was observed in the HEI condition it did not affect negatively the quasi-static mechanical performance of the joints. Moreover, the higher amount of flaws at the PTMAZ changed the fracture mode of the HEI joints and it failed catastrophically. Joints produced under low heat input joining condition failed through a combination of shearing of the metallic pins and a mixed of cohesive (CF) and adhesive (AF) failure in the consolidated molten polymer at the interface between upper and lower parts.

6.5.
Recommendations for future work

Although this master thesis fulfilled the proposed objectives, some points remain open for future investigations. This may include:

- The polymer interaction volume above the deformed rivet tip (VR) in friction-riveted joints was calculated through two methods: a quotient between $Vol_{PEEK\text{-}30CF}$ and the sum of $Vol_{Ti\text{-}6Al\text{-}4V}$ and $Vol_{PEEK\text{-}30CF}$ (measurements provided by microCT) ($VR_{\mu\text{-}ct}$), and a simplified geometric model (VR_A). The averages obtained by the analytical model was slightly superior to the measurement method by microCT which was performed with absence of replicates. Further, experiments are needed to statistically evaluate and confirm the results obtained by microCT.
- Friction-riveted joints produced under high energy input failed by shear through the rivet inside the grips before reaching the maximum material (Ti-6Al-4V) tensile strength. Thus, a deeper investigation on the grips can be performed to access their influence on the rivet base material during the test and consequently on the joints mechanical strength.
- Further investigations should be carried out through microCT parameters which can allow visualize microvoids and understand their influence on the mechanical performance of U-Joining joints produced under LEI joining condition.

7
Bibliography

[1] MALLICK, P. K. **Materials design and manufacturing for lightweight vehicles**. Woodhead Publishing Limited, Vol. 1, 2010.

[2] Boeing 787: From the Ground Up. <www.boeing.com/commercial/aeromagazine/articles/qtr_4_06/article_04_2> . Accessed: Aug/2017.

[3] <http://altairenlighten.com/in-depth/fiber-reinforced-composites>. Accessed: Aug/2017.

[4] **Flight Airworthiness Tecnology**. Airbus Technical Magazine: Vol. 48, 2011.

[5] TenCate Advanced Armour will provide ballistic solutions for the Embraer KC-390, Composites World. <http://www.compositesworld.com/news/tencate-advanced-armour-will-provide-ballistic-solutions-for-the-embraer-kc-390>. Accessed: Aug/2017.

[6] <http://www.quattroworld.com/technology/part-2-audi-techday-lightweight-design-milestones-historic-and-current-models> Accessed: Aug/2017.

[7] **BMW i3, the inside story: what it's made of, how it's made**, SAE International. <http://articles.sae.org/12056/>. Accessed: Aug/2017.

[8] MESSLER, Jr.; ROBERT, W. **The challenges for joining to keep pace with advancing materials and designs**. Materials & Design, Vol. 16(5), pp. 261-269, 1996.

[9] ROTHEISER, J. **Joining of Plastics 3E: Handbook for Designers and Engineers**. 3rd ed, Munich; Cincinnati, Ohio: Hanser, 2009.

[10] HABENICHT, G. **Applied Adhesive Bonding: A Practical Guide for Flawless Results**. Vol. 1, Weinheim: Wiley-VCH, 2009.

[11] MESSLER, R. W. **Joining of Materials and Structures: From Pragmatic Process to Enabling Technology**. Vol. 1, Butterworth-Heinemann, 2000.

[12] MARINELLI, J. M.; LAMBING, C. L. T. **Advancement in Welding Technology for Composite-to-Metallic Joints**. Journal of Advanced Materials, Vol. 25, pp. 20-27, 1994.

[13] HOU, M.; Ye, L.; MAY, Y.W. **An Experimental Study of Resistance Welding of Carbon Fiber Fabric Reinforced Polyetherimide (CF Fabric/PEI) Composite Material**. Applied Composite Materials, Vol 6, pp 35-49, 1999.

[14] AGEORGES, C. Ageorges; YE, L. **Resistance Welding of Metal/Thermoplastic Composite Joints**. Journal of Thermoplastic Composite Materials: Vol. 14(6), pp. 449–475, 2001.

[15] HOJJATI, M.; IMMARIGEON, J. P. **Fusion Bonding/Welding of Thermoplastic Composites**. Journal of THERMOPLASTIC COMPOSITE MATERIALS, Vol. 17, pp. 303-341, 2014.

[16] MITSCHANG, P.; VELTHIUS, R.; DIDI, M. **Induction Spot Welding of Metal/CFRPC Hybrid Joints**. Advanced Engineering Materials, Vol. 15, pp. 804-813, 2013.

[17] BALLE, F.; WAGNER, G.; EIFLER, D. **Ultrasonic Metal Welding of Aluminium Sheets to Carbon Fibre Reinforced Thermoplastic Composites**. Adv. Eng. Mater., Vol. 11(1-2), pp. 35-39, 2009.

[18] BECKER, F.; POTENTE, H. **A step Towards Understanding the Heating Phase of Laser Transmission Welding in Polymers**. Polymer Engineering and Science, Vol. 42(2), pp. 365-374, 2002.

[19] KATAYAMA, S.; KAWAHITO, Y. **Laser direct joining of metal and plastic. Scripta Materialia**, Vol. 59(12), pp. 1247-1250, 2008.

[20] AMANCIO-FILHO, S. T.; DOS SANTOS, J. F. **European Patent 2329905B1**, 2012.

[21] AMANCIO-FILHO, S. T.; BEYER, M.; DOS SANTOS, J. F. **European Patent DE102005056606A1**, 2005.

[22] AMANCIO-FILHO, S. T.; FEISTAUER, E. E.; DOS SANTOS, J. F. **European Patent Application EP3078480A**1, 2015.

[23] **Raiser innovation award for friction welding. Category: Auszeichnung**. Friction spot joining of lightweigth metals and fiber-reinforced polymer hybrid structures, award in the Klaus Raiser Gmbh, Munich, Germany, 2011.

[24] AMANCIO-FILHO, S. T.; *et al*. **On the feasibility of friction spot joining in magnesium/fiber-reinforced polymer composite hybrid structures**. Materials Science and Engineering, Vol. 528(10-11), pp. 3841-3848, 2011.

[25] GOUSHEGIR, S. M. **Friction spot joining of metal-composite hybrid structures**. Ph.D. Thesis, Technical Univesity of Hamburg (TUHH), Hamburg, Germany, 2015.

[26] GOUSHEGIR, S. M.; DOS SANTOS, J. F.; AMANCIO-FILHO, S. T. **Friction spot joining of aluminum AA2024/Carbon-fiber reinforced poly(phenylene sulfide) composite single-lap joints: microstructure and mechanical performance**. Materials & Design, Vol. 50, pp. 196-206, 2014.

[27] ESTEVES, J. V.; *et al.* **Friction spot joining of aluminum AA6181-T4 and carbon fiber-reinforced poly(phenylene sulfide): Effects of process parameters on the microstructure and mechanical strength**. Materials & Design, Vol. 66, pp. 437-445, 2015.

[28] ESTEVES, J. V.; *et al.* **Friction Spot Joining of aluminum 6181-T4 and carbon fiber reinforced poly(phenylene sulfide)**. ANTEC, 2012.

[29] ANDRÉ, N. M.; *et. al.* **Friction Spot Joining of Aluminum Alloy 2024-T3 and CarbonFiber-Reinforced Poly(phenylene sulfide) with Additional PPS Film Interlayer: Microstructure, Mechanical Strength and Failure**. Submitted to Composites-Part B Engineering, 2015.

[30] AMANCIO-FILHO, S.T. **Friction riveting: Development and analysis of a new joining technique for polymer-metal multi-materials structures**. Ph.D. Thesis, Technical Univesity of Hamburg (TUHH), Hamburg, Germany, 2007.

[31] AMANCIO-FILHO, S. T.; DOS SANTOS, J. F. **A new joining technique for thermoplastics-lightweight alloy structures**. Pittsburg, USA, 2008.

[32] BORBA, N.Z.; *et al.* **On the Process-Related Rivet Microstructural Evolution, Material Flow and Mechanical Properties of Ti-6Al-4V/GFRP Friction-Riveted Joints**. Journal Materials (Basel), Vol. 10(2), pp. 184, 2017.

[33] PROENÇA, B.; *et al*. **Force controlled Friction Riveting of glass fiber reinforced polyamide 6 and aluminum alloy 6056 hybrid joints**. ANTEC, Orlando, USA, 2015.

[34] AMANCIO-FILHO, S.T. Rebitagem por fricção ('FricRiveting'). **Desenvolvimento de uma nova técnica de união para juntas híbridas do tipo polímero-metal. Parte I: Processo e microestrutura**, Soldag. Insp., Vol. 16, pp. 387-394, 2011.

[35] ALTMEYER, J.; DOS SANTOS, J.F.; AMANCIO-FILHO, S.T. Effect of **Friction Riveting Process Parameters on the Joint Formation and Performance of Ti alloy/ Short-fibre Reinforced Polyether Ether Ketone Joints**. Materials&Design, Vol. 60, pp. 164-176, 2014.

[36] RODRIGUES, C. F.; *et al*. **FricRiveting of aluminum 2024-T351 and polycarbonate: Temperature evolution, microstructure and mechanical performance**. Journal of Materials Processing Technology, Vol. 214, pp. 2029-2039, 2014.

[37] BLAGA, L.; BANCILA, R.; DOS SANTOS, J.F.; AMANCIO-FILHO, S.T. **Friction Riveting of glass-fibre-reinforced polyetherimide composite and titanium grade 2 hybrid joints**. Materials and Design, pp. 825–829, 2013.

[38] BORBA, N.Z.; *et al.* **Friction Riveting of pultruded thermoset glass fiber reinforced polyester composite and Ti6Al4V hybrid joints**. ANTEC, 2014.

[39] EBEL, T.; AMANCIO-FILHO, S.T.; DOS SANTOS, J. F. **Method for manufacturing metal casings with structured surfaces**. European patent nº EP 2 468 436 B1.

[40] FEISTAUER, E.E.; *et al.* **Ultrasonic joining of trough-the-thickness reinforced TI-4AL-6V and polyetherimide hybrid joints**. ANTEC, 2017.

[41] FEISTAUER, E.E.; *et al.* **Ultrasonic joining: A novel direct-assembly technique for metal-composite hybrid structures**. Materiasl letters, Vol. 170, pp 1-4, 2016.

[42] SALVO, L.; *et al.* **X-Ray micro-tomography an attractive characterisation technique in materials science. Nuclear instruments and methods in physics research**. Elsevier Science: B 200, pp. 273-286, 2003.

[43] THORNTON, H.F.K. **Three-dimensional materials science: an intersection of three-dimensional reconstructions and simulations**. MRS Bull, Vol. 33, pp. 629, 2008.

[44] YANG, S.; ZHANG, R.; QU, X. **X-ray tomographic analysis of powder-binder separation in SiC green body**. SciVerse ScienceDirect, Vol. 33, pp. 2935-2941, 2013.

[45] SINKA, I.C.; *et al*. **Measurement of density variations in tablets using X-ray computed tomography.** International Journal of Pharmaceutics, Vol. 271, pp. 215-224, 2004.

[46] LANDIS, E. N.; KEANE. D. T. **X-ray microtomography**. ScienceDirect, Vol. 61, pp. 1305-1316, 2010.

[47] GUDE, M.; *et al*. **Thermoclinching - A novel joining process for lightweight structures in multi-materials design**. Composites Theory and Pratice, Vol. 14(3), pp. 128-133, 2014.

[48] ABIBI. A. B. **Friction-based Injection Clinching Joining (F-ICJ): a new joining method for hybrid lightweight structures**. Ph.D. Thesis, Technical Univesity of Hamburg (TUHH), Hamburg, Germany, 2015.

[49] ABIBI. A. B.; *et al.* **Mechanical and failure behavior of hybrid polymer-metal staked joints**. Material and Design, Vol. 46, pp. 338-347, 2013.

[50] DAVIS, J. R. **Aluminum and Aluminum Alloys**. Materials Park, OH: ASM International, 1993.

[51] CONSTELLIUM, **Technical Datasheet of Alloy 2024**. France, 2009.

[52] ANDRÉ, M. N. **Friction spot joining of aluminum alloy 2024-T3 and carbon-fiber-reinforced polyphenylene sulfide composite laminate with PPS film interlayer**. Master thesis, Federal University of São Carlos, São Carlos, Brazil, 2015.

[53] **Tencate Advanced Composites, Technical Datasheet of CETEX® PPS**. Netherlands, 2009.

[54] **Flight airworthiness technology**. Airbus Technical Magazine, Vol. 48, 2011.

[55] LITE, P. **Technical Datasheet of PPS film**. Austria, 2009.

[56] BOYER, R.; WELSCH, G.; COLLINS, E. **Materials Properties Handbook: Titanium Alloys**. ASM Internacional, 1994.

[57] KITAMURA, K.; FUJII, H.; IWATA, Y.; SUN, Y.S.; MORISADA, Y. **Flexible control of the microstructure and mechanical properties of friction stir welded Ti–6Al–4V joints**. Material and Design, Vol. 46, pp. 348-354, 2013.

[58] BOYER, R.R. **An overview on the use of titanium in the aerospace industry.** Int. Symp. Metall. Technol. Titan. Alloys, Vol. 213, no. 1-2, pp. 103-114, 1996.

[59] WANG, S.; WEI, M.; TSAY, L. **Tensile properties of LBW welds in Ti–6Al–4V alloy at evaluated temperatures below 450 °C**. Materials and Letter, Vol. 57(12), pp. 1815-1823, 2003.

[60] LIMA, M.S.F. **Laser beam welding of titanium nitrid coated titanium using pulse-shaping**. Materials Research, pp. 323-328, 2005.

[61] LEYENS, C.; PETERS, M. **Titanium and Titanium Alloys: Fundamentals and Applications**. Weinheim: Wiley-VCH, 2003.

[62] MATA, F.; *et al.* **Influence of cutting conditions on machinability aspects of PEEK, PEEK CF 30 and PEEK GF 30 composites using PCD tools**. Journal of Materials Processing Technology, Vol. 209, pp. 1980-1987, 2009.

[63] **Handbook of Engineering Plastics**, Vol. 2. ASM International, 1998.

[64] BORMAN, R.; EBEL, T.; FERRY, O. **The influence of a small boron addition the microstructure and mechanical properties of Ti-6Al-4V fabricated by metal injection moulding**. Advanced Materials Engineering, 2011.

[65] BRYDSON, J. A. **Plastics materials**. Vol. 7, Butterworth Heinemann, USA, 1999.

[66] GINGER, G. **Thermoplastic composites gain leading edge on the A380**. High Performance Thermoplastics, Vol.50, pp. 50-55, 2006.

[67] KURODA, S.I.; *et al*. **Degradation or aromatic polymers-I. Rates of crosslinking and chain scission during thermal degradation of several soluble aromatic polymers**, Eur. Polym. J., Vol.25, no. 1, pp. 1-7, 1989.

[68] BUENO, C. **Estudo de viabilidade técnica de novo processo de união pontual por fricção de metais a compósitos termoplásticos**. Dipl. Thesis, Federal University of São Carlos (UFSCar), São Carlos, Brazil, 2010.

[69](https://www.hzg.de/institutes_platforms/materials_research/materials_mechanics/solid_state_joining_processes/techniques/index.php.en). Accessed 07/02/2017.

[70] ALTMEYER, J. **Fundamental characteristics of friction riveted multi-material joints**. Ph.D. Thesis, Technical Univesity of Hamburg (TUHH), Hamburg, Germany, 2015.

[71] A. Neumann. **Reibschweissen von Metallen 1. Auflage. Verlag Technik GmbH**. Berlin, Germany, 1991.

[72] AMANCIO-FILHO, S.T.; DOS SANTOS, J.F **Preliminary analytical modeling of heat input in friction riveting**. ANTEC, 2016.

[73](https://www.hzg.de/imperia/md/content/hzg/institut_fuer_werkstoffforschung/nwg/eduardo_u-joining_protected.pdf). Accessed 06/02/2017.

[74] GARNAIK, S. **Infrared thermography: A versatile technology for condition monitoring and energy conservation**. Kanpur, India.

[75] ZEISS. **XRM Flat Panel User's Guide. Carl Zeiss X-ray Microscopy**. Pleasanton, USA, 2015.

[76] TAN, X.; *et al.* **Characteristics and formation mechanism of porosities in CFRP during laser joining of CFRP and steel**. Composites Part B: Engineering, Vol. 70, pp. 35-43, 2015.

[77] ZHAO, J.W.; *et al.* **Modeling of dynamic recrystallization of Ti6Al4V alloy using a cellular automaton approach**, Acta Metall. Sin. Engl. Lett, Vol. 21(4), pp. 260-268, 2008.

[78] BORBA, Z. N. **Friction riveting of Ti-6Al-4V and pultruded fiber reiforced thermoset polyester hybrid joints**. Master thesis, Federal University of São Carlos, São Carlos, Brazil, 2015.

[79] AMANCIO-FILHO, S.T.; DOS SANTOS, J.F**. Influence of processing parameters on microstructure and properties of a polyetherimide joined by FricRiveting: Investigation of rotational speed**. ANTEC, Chicago, USA, 2009.

[80] REED-HILL, R. E. R**. Abbaschian. Physical Metallurgy Principles.** 4th ed. Cengage Learning India, 2008.

[81] AMANCIO-FILHO, S.T.; *et al.* **Determination of fracture mechanism under tensile loading in commercial available engineering thermoplastic material joined by FricRiveting**. In: 5th International Conferenceon Fracture of Polymer, Composites and Adhesives. LesDiablerets, Switzerland, 2008.

[82] AMANCIO-FILHO, S.T.; et al. **Thermal degradation of plyetherimide joined by friction riveting (FricRiveting)**. Polymer degradation and stability, Vol. 93(8), pp. 1529-3538, 2008.

APPENDIXES

APPENDIX A - The table presented below displays some of main specifications of the Versa 510 equipment.

Zeiss-XRadia Versa 510 technical Specifications

Specifications	
Spatial resolution [μm]	0,7
Tube voltage range [KN]	30 – 160
Maximum Output [W]	10
Sample size limit [mm]	300
Stage travel	360º
Load capacity [kg]	15

APPENDIX B - Monitoring curves of the joining parameters for each joining condition.

- Low Energy Input

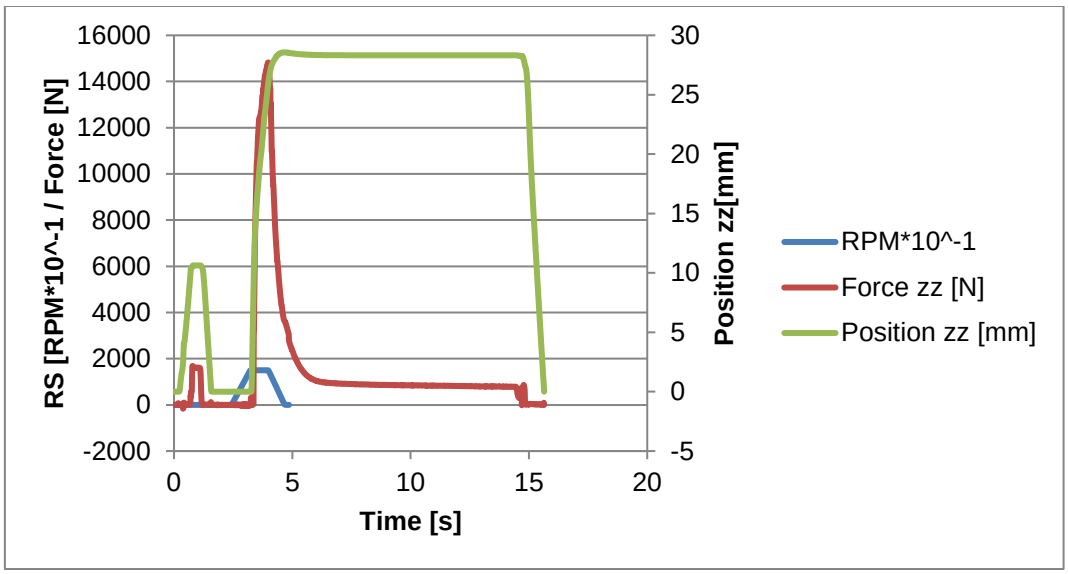

- High Energy Input

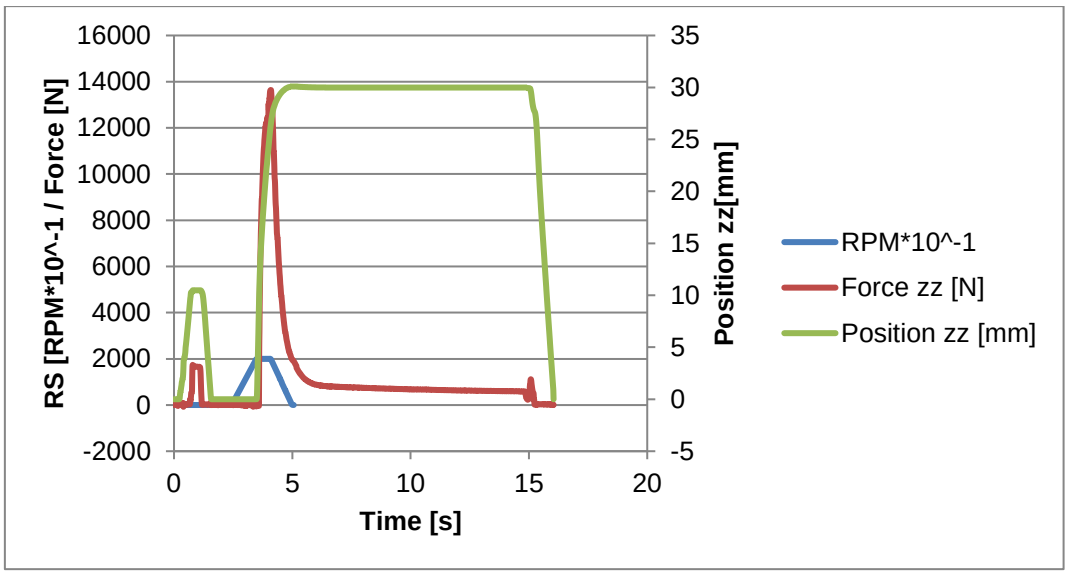

APPENDIX C - Energy dispersive X-Ray spectroscopy evaluation of the composite part in this work (PEEK 30-CF) for each joining condition.

- High Energy Input

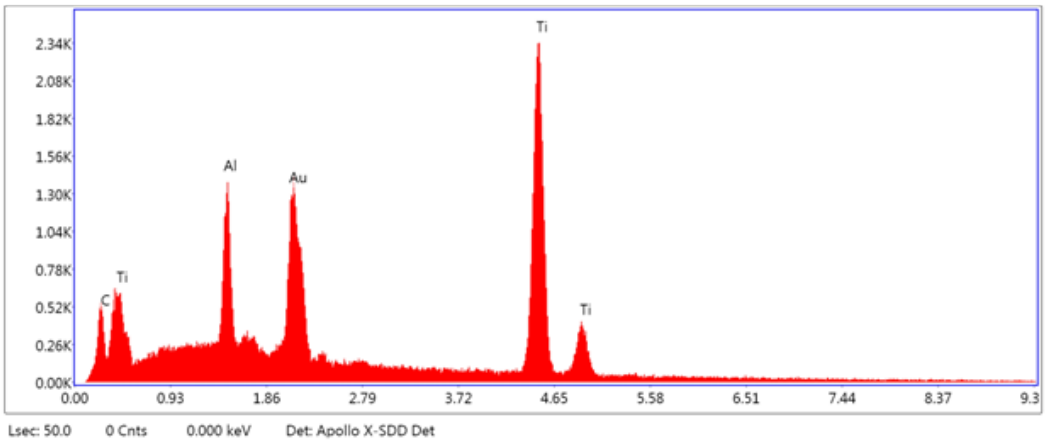

Elements identified through EDS analysis in LEI joints

Element	Weight %	Atomic %	Net Int.	Error %	Kratio
CK	15.03	44.63	86.95	9.72	0.0713
Alk	7.93	10.48	203.55	5.91	0.0637
AuM	22.15	4.01	219.96	6.12	0.2011
TIK	54.90	40.88	538.61	3.09	0.5303

- Low energy Input

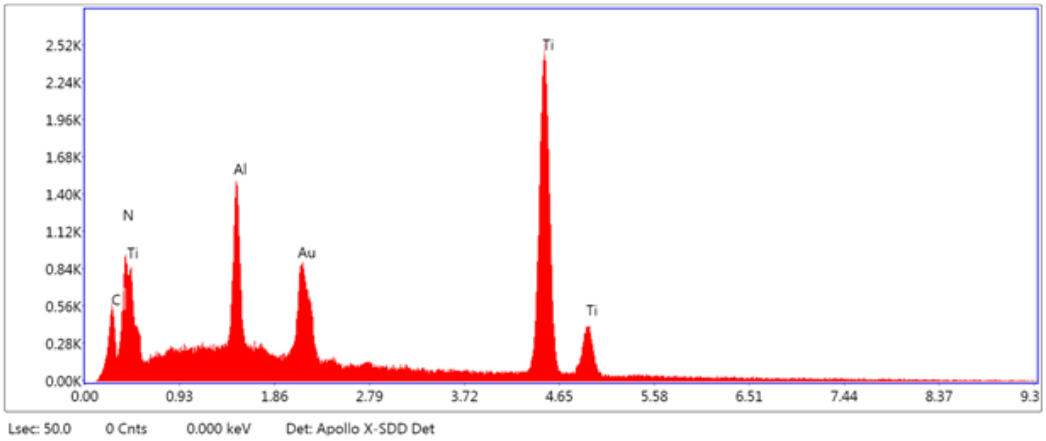

Elements identified by EDS analysis in LEI joints

Element	Weight %	Atomic %	Net Int.	Error %	Kratio
CK	15.22	38.04	94.85	9.42	0.0721
Alk	8.62	9.59	232.86	5.58	0.0671
AuM	13.02	1.98	141.54	7.18	0.1194
TIK	56.01	35.11	577.54	2.90	0.5224